Heat diffusion during thin-film composite membrane formation

Accepted Author Manuscript

A. Deshmukh, J. H. Lienhard and M. Elimelech, "Heat diffusion during thin-film composite membrane formation", *Journal of Membrane Science* (2024), 696, 122493.

https://doi.org/10.1016/j.memsci.2024.122493

Heat Diffusion During Thin-Film Composite Membrane Formation

Akshay Deshmukh,[1,2] John H. Lienhard,[2,*] and Menachem Elimelech[1,*]

[1]Department of Chemical and Environmental Engineering, Yale University, 17 Hillhouse Avenue, New Haven, CT 06511, United States

[2]Department of Mechanical Engineering, Massachusetts Institute of Technology, 77 Massachusetts Avenue, Cambridge, MA 02139, United States

[*]Corresponding Authors: Menachem Elimelech (menachem.elimelech@yale.edu), John H. Lienhard (lienhard@mit.edu)

Thin-film composite (TFC) membranes, the backbone of modern reverse osmosis and nanofiltration, combine the high separation performance of a thin selective layer with the robust mechanical support. Previous studies have shown that heat released during interfacial polymerization (IP) can have a significant impact on the physical and chemical structure of the selective layer. In this study, we develop a multilayer transient heat conduction model to analyze how the thermal properties of the materials used in TFC fabrication impact interfacial temperature, focusing on support-free (SFIP), conventional (CIP), and interlayer-modulated IP (IMIP). Using a combination of analytic solutions and computational models, we demonstrate that the thermal effusivities of fluid and material layers can have a significant effect on the temporal evolution of interfacial temperature during IP. In CIP, we show that the presence of a polymeric support adjacent to the reaction interface yields a 20% to 60% increase in interfacial temperature rise, lasting for ~ 0.1 s. Furthermore, we demonstrate that inorganic or metallic interlayers, which have high thermal effusivities, can lead to short-lived order-of-magnitude reductions in interfacial temperature rise. Finally, we provide analytical approximations for transient heat conduction through multilayered systems, enabling rapid evaluation of the thermal impact of novel membrane support and interlayer materials and structures on interfacial temperature during TFC fabrication. Quantifying how the thermal properties of solvents, support layers, and interlayers affect interfacial temperature during IP is critical for the rational design of new TFC membranes.

Graphical Abstract

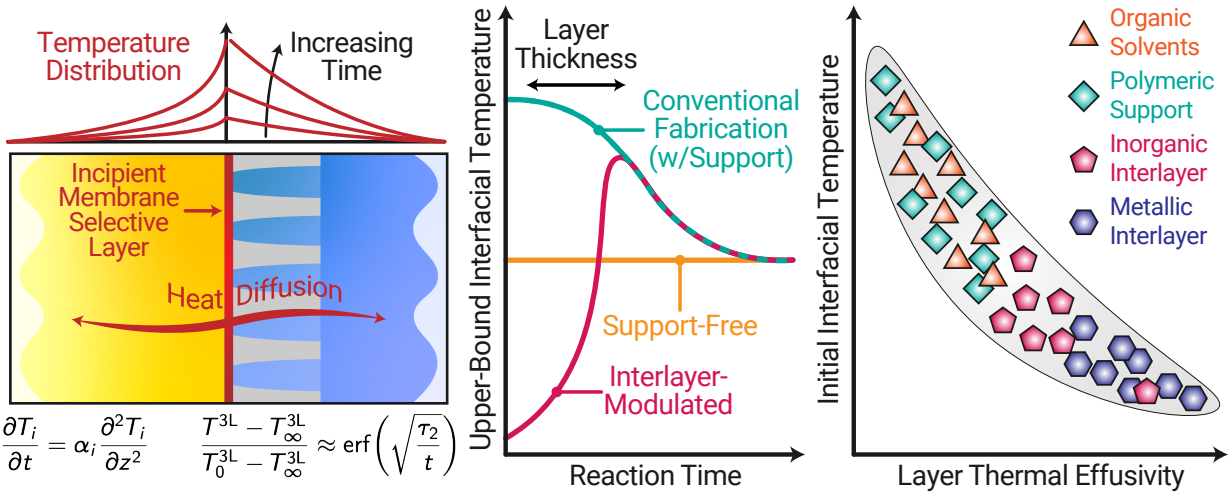

1 Introduction

Thin-film composite (TFC) membranes comprise a thin selective layer ($< 10^{-7}$ m) coupled with a thicker porous layer ($\sim 10^{-4}$ m), which provides mechanical support for pressure-driven separations including reverse osmosis (RO) and nanofiltration (NF). Combining a thin selective layer with a highly porous and mechanically robust support enables membrane permeance and mechanical strength to be optimized simultaneously. Over the last fifty years, the increased permeance and selectivity of polyamide-based TFCs has drastically improved the performance of desalination membranes, driving significant reductions in energy consumption and salt passage [1–3]. New TFC membrane and support layer chemistries and structures are being designed for a wide range of applications, including ion selectivity for resource recovery using NF [4–10], chlorine resistance for biofouling-tolerant RO and NF modules [11–16], and high mechanical strength for efficient brine concentration using high-pressure or low-salt rejection RO [17, 18]. TFC membranes are also being developed for nonaqueous applications requiring angstrom- and nanoscale selectivity, including gas separation [19–21] and organic solvent RO and NF [22–26].

The selective layer in current RO and NF TFC membranes is a polyamide film formed by the exothermic interfacial polymerization (IP) of a bifunctional amine dissolved in water and a trifunctional acid chloride dissolved in an organic solvent. The reaction begins when the aqueous and organic solutions come in contact, allowing the amine to partition into the organic solvent, where it reacts rapidly with the acid chloride [27, 28]. Heat from the polycondensation reaction is then transferred into and through fluid layers, support layers, or interlayers adjacent to the reaction interface. Consequently, the thermal properties of the adjacent fluid layers, support layers, and interlayers have a large impact on interfacial temperature during the IP process.

Recent studies have shown that temperature increase driven by heat released during polymerization can have a significant impact on the structure and morphology of the selective layer, influencing key transport parameters, such as permeability and selectivity, and other membrane performance metrics, such as fouling and scaling resistance [29–35]. Heat released during selective layer formation has been shown to promote interfacial destabilization [31, 33–35] and drive solution degassing and nanobubble formation [36–40], while reducing interfacial tension and fluid viscosity, producing rougher membrane morphologies. Experimental

efforts have also demonstrated that selective layer performance can be tuned using novel membrane fabrication techniques, including support-free [29, 30] and interlayer-modulated IP [41–45]. Both the absence of a polymeric support layer and the presence of an inorganic or metallic interlayer in the vicinity of the reaction interface can affect heat transfer away from the interface, altering the physical and chemical structure of the incipient selective layer.

Understanding how the thermal properties of fluid layers, support layers, and interlayers affect interfacial temperature during IP is essential to guide the development of new high-performance RO and NF membranes for a range of emerging applications. Ascertaining how solvents, support layers, and interlayers might promote or restrict transient heat transfer during membrane fabrication enables the effects of elevated interfacial temperatures to be isolated from the plethora of complex phenomena that affect selective layer formation.

This study builds an analytical framework that explains how the thermal properties of solvent layers, support layers, and interlayers control interfacial temperature during selective layer formation for RO and NF membranes. First, a transient heat conduction model is developed for a time-dependent planar heat release in a multilayered system that comprises a reaction interface sandwiched between two semi-infinite fluid layers, one of which may include either a porous support layer or both an interlayer and a support layer (Figure 1). The thermal properties of typical support layer and interlayer materials (including conductivity, volumetric heat capacity, diffusivity, and effusivity) are then surveyed and bounded as a function of layer porosity and structure. The governing equations are solved in the Laplace domain for an arbitrary planar source intensity across two-, three-, and four-layer systems, representing support-free, conventional, and interlayer-modulated IP, respectively. For a diffusion-limited interfacial model, which gives an upper bound on planar heat release, Laplace-domain solutions are inverted analytically, where possible, and numerically to obtain the interfacial temperature as a function of time and the thermal properties. Finally, we develop a closed-form analytical approximation for interfacial temperature in conventional IP and examine how temperature profiles away from the reaction interface evolve over time. The computational code developed can be used to rapidly analyze heat transfer and temperature rise through multilayered systems with arbitrary, time-dependent, planar heat source intensities.

2 Heat Transfer Model

2.1 Model Assumptions

A one-dimensional planar model is developed to understand how solvent, support layer, and interlayer properties impact interfacial temperature. The model, which assumes a planar heat source at the reaction interface with one-dimensional heat conduction perpendicular to the interface, is based on two approximations. First, the interfacial reaction can be treated as a planar heat source because the thickness of the reaction zone ($l_{\text{rxn}} \sim 10^{-7}$ m) is three orders of magnitude smaller than the characteristic length scale for heat conduction ($l_{\text{cond}} = \sqrt{\alpha_{\text{eff}} \tau_{\text{rxn}}} \sim 10^{-4}$ m) given the effective thermal diffusivity of most solvents and polymers ($\alpha_{\text{eff}} \sim 10^{-7}$ m^2 s^{-1}) and experimentally observed reaction timescales ($\tau_{\text{rxn}} \sim 10^{-1}$ s) [46–49]. Support layers and interlayers are porous structures that typically have three-dimensional heterogeneity with anisotropic thermal properties. The characteristic length scale for variations in thermal properties parallel to the plane of the reaction interface (x-y plane) scales with the size of the largest support layer and interlayer pores ($l_{x\text{-}y} < 10^{-7}$ m). This corresponds to a transient heat transfer timescale of $\tau_{x\text{-}y} = l_{xy}^2/\alpha_{\text{eff}} \sim 10^{-7}$ s, six orders of magnitude smaller than the reaction timescale ($\tau_{\text{rxn}} \sim 10^{-1}$ s). Consequently, temperature gradients par-

allel to the plane of the reaction interface will dissipate rapidly, and heat conduction need only be considered in the direction perpendicular to the reaction interface (z-direction).

Figure 1 is a schematic illustration of heat transfer during thin-film composite (TFC) membrane selective layer fabrication via interfacial polymerization (IP) for three cases: (a) support-free IP (SFIP), (b) conventional IP (CIP), and (c) interlayer-modulated IP (IMIP). In SFIP [29], which can also be achieved by dual-slot coating [30], the selective layer is formed in the absence of a support layer, with heat generated during the reaction being conducted into semi-infinite organic and aqueous solutions (layers 1 and 2, respectively). In CIP [50], heat generated during IP is initially transferred into the semi-infinite organic solution (layer 1) and a finite thickness (d_2) support layer (layer 2), which typically comprises a porous polymer containing the aqueous solution. Over time heat is conducted through the support layer and into the semi-infinite aqueous solution (layer 3). In IMIP [51], heat released at the reaction interface is first transferred into the semi-infinite organic solution (layer 1) and a finite interlayer (layer 2, thickness d_2). Heat is then conducted through the interlayer into a finite support layer (layer 3, thickness d_3), and finally into the semi-infinite aqueous solution (layer 4). SFIP, CIP, and IMIP correspond to two-, three-, and four-layer heat transfer systems, respectively. The location of the planar heat source at the interface between layers 1 and 2 ($z = 0$) in SFIP, CIP, and IMIP, is fixed throughout. Similarly, the interfaces between layers 2 and 3 in CIP and IMIP ($z = d_2$) and layers 3 and 4 in IMIP ($z = d_2 + d_3$) are fixed during the reaction.

2.2 Transient Heat Conduction Equations

In the absence of convection, the transient temperature field (expressed as the deviation from the initial or reference temperature, $u_i = T_i - T_{\text{ref}}$) in each layer i of an n-layer heat transfer system is governed by the heat conduction equations [52]:

$$\frac{\partial u_i}{\partial t} = \alpha_i \frac{\partial^2 u_i}{\partial z^2} \tag{1}$$

where T_i is the temperature, T_{ref} is the reference temperature, and $\alpha_i = k_i/\rho_i c_{\text{P},i}$ is the thermal diffusivity of layer i. Neglecting contact resistances, temperature and heat flux boundary conditions ($t > 0$) are

$$\begin{aligned} u_1(0,t) &= u_2(0,t) \\ -k_1 \frac{\partial u_1}{\partial z}(0,t) + q(t) &= -k_2 \frac{\partial u_2}{\partial z}(0,t) \end{aligned} \tag{2}$$

$$\begin{aligned} u_i(z_i,t) &= u_{i+1}(z_i,t) && \forall\, i \in 2,...,n-1 \\ -k_i \frac{\partial u_i}{\partial z}(z_i,t) &= -k_{i+1} \frac{\partial u_{i+1}}{\partial z}(z_i,t) && \forall\, i \in 2,...,n-1 \end{aligned} \tag{3}$$

$$\begin{aligned} u_1(z \to -\infty, t) &\to 0 \\ u_n(z \to \infty, t) &\to 0 \end{aligned} \tag{4}$$

where q is the transient planar heat flux at $z = 0$ and $z_i = \sum_{j=2}^{j=i} d_j$ is the location of the interface between layers i and $i+1$. Initial conditions are $u_1(z < 0, t) = 0$, $u_n(z_{n-1} < z, t) = 0$, and $u_i(z_{i-1} < z < z_i, t) = 0$ $\forall\, i \in 2,...,n-1$. Defining $U_i(z,s) = \mathscr{L}\{u_i(z,t)\}$ as the Laplace transform of the temperature field in each

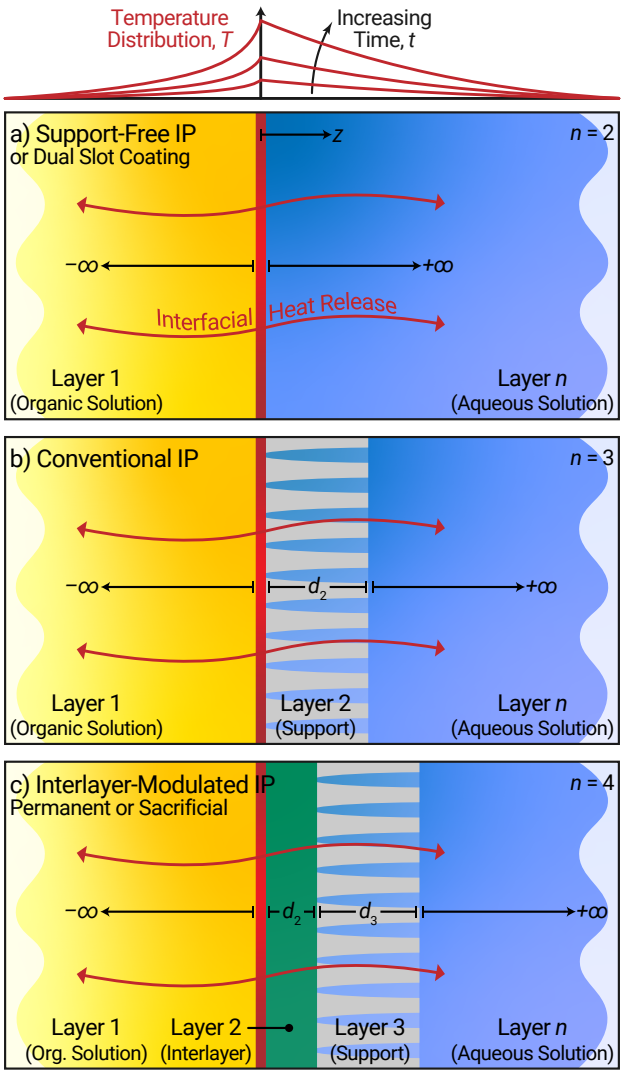

Figure 1: Schematic illustration of heat transfer in an n-layer system during interfacial polymerization (IP) for the fabrication of thin-film composite (TFC) membrane selective layers via (a) support-free or dual slot coating IP (SFIP, $n = 2$), (b) conventional IP (CIP, $n = 3$) with a support layer (gray), and (c) interlayer-modulated IP (IMIP, $n = 4$) with a support layer and an interlayer (green), which can be permanent or sacrificial. Heat released during the exothermic interfacial reaction can be treated as a planar heat source at the interface between layers 1 and 2 ($z = 0$) as the reaction zone is thin ($\sim 10^{-7}$ m) compared to the characteristic length scale for heat transfer ($\sim 10^{-4}$ m at 0.1 s). The heat released is simultaneously transferred into layer 1 ($z < 0$) and (a) layer 2 ($z > 0$); (b) layer 2 (support layer, $0 < z < d_2$) and then layer 3 ($z > d_2$); and (c) layer 2 (interlayer, $0 < z < d_2$), then layer 3 (support layer, $d_2 < z < d_2 + d_3$), and finally layer 4 ($z > d_2 + d_3$). Fluid layers 1 and n represent the organic solution, containing a trifunctional acid chloride, and the aqueous solution, containing a bifunctional amine. Layer 2 in CIP and layer 3 in IMIP is a porous support layer, while layer 2 in IMIP is an interlayer, which can be permanent or removed after fabrication. Both layers 2 and 3 are impregnated with the aqueous diamine solution before the reaction begins.

layer, the governing heat transfer equations can be written as

$$\frac{d^2U_i}{dz^2} - \frac{sU_i}{\alpha_i} = 0 \tag{5}$$

where s is the complex Laplace domain variable. The boundary conditions in the Laplace domain are given by

$$U_1(0,s) = U_2(0,s)$$
$$-k_1\frac{dU_1}{dz}(0,s) + Q(s) = -k_2\frac{dU_2}{dz}(0,s) \tag{6}$$
$$U_i(z_i,t) = U_{i+1}(z_i,t) \qquad \forall\, i \in 2,\ldots,n-1$$
$$-k_i\frac{dU_i}{dz}(z_i,t) = -k_{i+1}\frac{dU_{i+1}}{dz}(z_i,t) \qquad \forall\, i \in 2,\ldots,n-1 \tag{7}$$
$$U_1(z \to -\infty, s) \to 0$$
$$U_n(z \to \infty, s) \to 0 \tag{8}$$

where $Q(s) = \mathscr{L}\{q(t)\}$. Integrating Equation 5, the Laplace-domain temperature increase (U_i) and heat flux ($-k_i(dU_i/dz)$) in layer i can be expressed as

$$U_i = A_i \exp\left(z\sqrt{\frac{s}{\alpha_i}}\right) + B_i \exp\left(-z\sqrt{\frac{s}{\alpha_i}}\right) \tag{9}$$

$$-k_i\frac{dU_i}{dz} = -\kappa_i\sqrt{s}\left[A_i \exp\left(z\sqrt{\frac{s}{\alpha_i}}\right) - B_i \exp\left(-z\sqrt{\frac{s}{\alpha_i}}\right)\right] \tag{10}$$

where A_i and B_i are integration constants for layer i, and $\kappa_i = k_i/\sqrt{\alpha_i} = \sqrt{k_i\rho_i c_{\mathrm{P}i}}$ is the thermal effusivity of layer i (units W $\mathrm{s}^{\frac{1}{2}}$ m^{-2} K^{-1}). Integration constants A_i and B_i are a function of the thermal diffusivity of each layer ($\alpha_1, ..., \alpha_n$), the thermal effusivity of each layer ($\kappa_1, ..., \kappa_n$), the thickness of each finite layer ($d_2, ..., d_{n-1}$), the Laplace transform of the rate of interfacial heat release (Q), and the Laplace-domain variable (s).

2.3 Bounding Interfacial Heat Release

The fabrication of RO and NF membrane selective layers by IP is a rapid multistage process in which half the film is formed in ~ 2 s for most TFC chemistries [46–49]. When the organic-phase reactant (trifunctional acid chloride) is in stoichiometric excess, studies have shown that IP generally proceeds through three stages [46, 48, 49, 53–58]. Initially, rapid incipient film formation is limited by the reaction rate and the diffusion of the aqueous-phase reactant (bifunctional amine) into the thin ($< 10^{-7}$ m) reaction zone on the organic side of the liquid-liquid interface. This is followed by film growth limited by bifunctional amine diffusion through the aqueous phase to the reaction interface. Finally, after a contiguous polymer film forms and precipitates, the reaction is limited by amine diffusion through the dense film.

The rate of planar heat release at the reaction interface during IP is given by the rate of polymerization multiplied by the enthalpy change of reaction. Modeling precise time-dependent polycondensation reaction rates during TFC selective layer fabrication is highly challenging, given the complexity of the IP process and the multitude of phenomena involved from oligomer formation and acid production to reactant hydrolysis and polymer precipitation. Several detailed microkinetic and macrokinetic reaction-diffusion models have been developed that accurately capture the dynamics of multistage IP as a function of monomer chemistry, initial monomer concentrations, and reaction conditions [46, 49, 53–58]. These studies have shown that after the rapid initial reaction stage, selective layer growth is limited by the diffusion of the rate-limiting monomer (aqueous bifunctional amine in RO and NF membrane fabrication) to the reaction interface. In this regime, selective layer growth and IP reaction rate are inversely proportional to the square root of reaction time. In this study, a semi-empirical model based on the diffusion-limited supply of the rate-limiting monomer (r^{dl}) is used as an upper bound for the planar reaction rate as a function of reaction time (t). In the diffusion-limited reaction model, the planar reaction rate is $r^{\mathrm{dl}} = r_0\sqrt{t_0/t}$, where r_0 (units kmol m^{-2} s^{-1}) and t_0 (units s) are reaction-specific constants, with r_0 defined as the diffusion-limited flux of the rate-limiting monomer to the reaction interface at time t_0. The planar heat source intensity resulting from a diffusion-limited interfacial reaction ($q^{\mathrm{dl}} = r^{\mathrm{dl}}\Delta_{\mathrm{r}}\underline{H}$) and its Laplace transform (Q^{dl}) can be expressed as

$$q^{\mathrm{dl}}(t) = q_0\sqrt{\frac{t_0}{t}}$$

$$Q^{\mathrm{dl}}(s) = q_0 \sqrt{\frac{\pi t_0}{s}} \tag{11}$$

where $q_0 = r_0 \Delta_{\mathrm{r}} \underline{H}$ (units W m^{-2}) is a reaction-specific constant, defined as the heat flux at time t_0 and $\Delta_{\mathrm{r}} \underline{H}$ (units J kmol^{-1}) is the enthalpy change of reaction per mole of rate-limiting monomer. Semi-empirical constants r_0 and t_0 can be estimated through the regression of experimental reaction rate data. Both parameters are a function of initial monomer concentrations, monomer transport properties, and reaction conditions. For the IP of benzene-1,3-diamine (*meta*-phenylenediamine) and 1,3,5-benzenetricarbonyl trichloride (trimesoyl chloride), which is used to fabricate high-performance TFCs for RO and tight NF applications, Nowbahar et al. 2018 measure $r_0 \approx 5 \times 10^{-7}$ kmol m^{-2} s^{-1} at $t_0 \approx 5 \times 10^{-1}$ s [47].

The diffusion-limited reaction assumption in Equation 11 neglects the complex polycondensation reaction kinetics that are captured in more advanced models and control the IP rate at small time [46, 49, 53–58]. However, the IP rate cannot exceed the rate of monomer transport to the reaction interface at any time during the reaction. Consequently, the expression for q^{dl} presented in Equation 11 represents a robust upper bound for the release of interfacial heat. Furthermore, while the expression for diffusion-limited interfacial heat release is unbounded as reaction time tends to zero, interfacial temperature is finite in this limit (Section 4). The subsequent analysis focuses on q^{dl} as a rigorous upper bound for interfacial heat release, however, the computational code provided can compute interfacial temperature for any planar heat release time form, provided its Laplace transform exists.

3 Solvent, Support Layer, and Interlayer Thermal Properties

3.1 Thermal Diffusivity and Effusivity of Solvents and Materials

The increase in temperature during membrane fabrication is a function of the thermal properties and thickness of each fluid layer (SFIP, CIP, and IMIP), support layer (CIP and IMIP), and interlayer (IMIP) present. At the reaction interface, where the selective layer is formed, temperature increase is governed by the thermal effusivity of each layer ($\kappa_1, ..., \kappa_n$) and the characteristic timescale for heat transfer through each finite layer ($\tau_2, ..., \tau_{n-1}$ where $\tau_i = d_i^2/\alpha_i$).

Thin-film selective layer fabrication can use a wide range of organic solvents, polymers, metals, and inorganic materials. In SFIP, CIP, and IMIP, layer 1 is a semi-infinite organic solution that is immiscible with water, while layer n is either a semi-infinite aqueous solution or a thick and highly porous woven fabric impregnated with the aqueous solution. Support layers (layer 2 in CIP and layer 3 in IMIP) for membranes used in spiral-wound and flat-sheet membrane modules are often polymeric, although inorganic and metallic materials have also been developed [59, 60]. Interlayers or gutter layers (layer 2 in IMIP), which can be temporary or permanent, can be made of a wide range of polymers, metals, or inorganic materials and their composites [41, 42, 61].

Figure 2 shows the thermal diffusivity ($\alpha = k/\rho c_{\mathrm{P}}$) and thermal effusivity ($\kappa = k/\sqrt{\alpha} = \sqrt{k\rho c_{\mathrm{P}}}$) of water together with selected organic solvents, polymers, metals, and inorganic materials (see Table E1 for data) [52, 62–68]. Organic solvents that are immiscible or only partially miscible with water span a narrow range of thermal effusivities, approximately 0.35 to 0.55 kW s$^{\frac{1}{2}}$ m^{-2} K^{-1}. The thermal effusivities of polymers, in nonporous form, are slightly higher, ranging from 0.30 to 0.80 kW s$^{\frac{1}{2}}$ m^{-2} K^{-1}, although still two- to four-times less than that of water. The thermal effusivities of most inorganic materials are an order of magnitude greater than that of typical organic solvents and polymers, ranging from 1.0 to 10 kW s$^{\frac{1}{2}}$ m^{-2} K^{-1}.

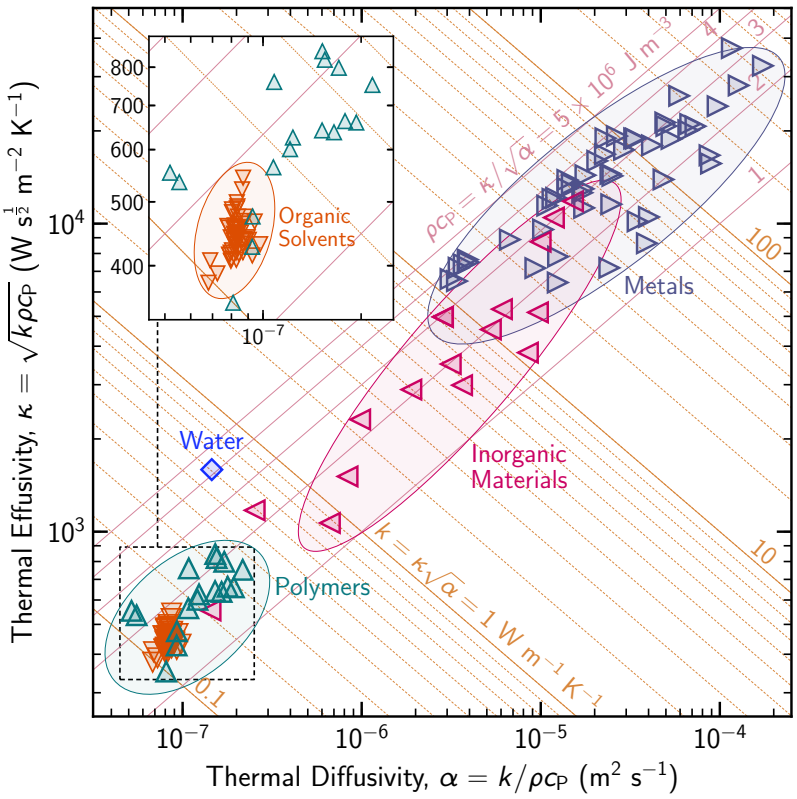

Figure 2: Thermal diffusivity ($\alpha = k/\rho c_P$) and thermal effusivity ($\kappa = k/\sqrt{\alpha} = \sqrt{k\rho c_P}$) of water (blue diamond), organic solvents (orange down triangles), polymers (green up triangles), metals (blue right triangles), and inorganic materials (pink left triangles) at 298 K. Isolines of constant thermal conductivity ($k = \kappa\sqrt{\alpha}$, light orange lines) and constant volumetric heat capacity ($\rho c_P = \kappa/\sqrt{\alpha}$, light pink) at 298 K and 1 bar are shown. Polymers, metals, and inorganic materials data are from references [52, 62–66]. Water and organic solvent data are from open-source software packages [67, 68] (see Table E1 for data).

Nonporous metals have the highest thermal effusivities ranging from below 10.0 kW s$^{\frac{1}{2}}$ m^{-2} K^{-1} for some alloys to above 100 kW s$^{\frac{1}{2}}$ m^{-2} K^{-1} for good conductors, such as aluminum and copper. Although the thermal effusivities of nonporous metals and inorganic materials are significantly higher than those of water and organic solvents, the support layers and interlayers are typically highly porous and impregnated with water prior to initiating the IP process. Consequently, it is essential to quantify the thermal properties of water-filled composites comprising porous polymers, metals, and inorganic materials [69].

3.2 Support Layer and Interlayer Porosity and Structure

Membrane support layers and interlayers are often highly porous, with spatial variations in structure and chemistry designed to minimize transmembrane transport resistance while providing sufficient mechanical support for the active layer during filtration. The composite thermal properties of water-impregnated support layers and interlayers layers, including thermal conductivity (k) and volumetric heat capacity (ρc_P), are porosity and structure specific [70, 71]. In this study, we neglect contact resistances and bound the thermal conductivity of composite layers using porosity-weighted arithmetic (k^{am}) and harmonic (k^{hm}) means of the thermal conductivities of each component material. Porosity-weighted arithmetic and harmonic mean thermal conductivities, which correspond to the combined conductance of conductors in parallel and in series, respectively, represent the widest possible limits on the composite thermal conductivity [70]. Neglecting any excess volume of mixing, the volumetric heat capacity of the composite material is estimated using the arithmetic mean of each constituent material, $(\rho c_P)^{am}$:

$$k^{am} = \varepsilon k_{aq} + (1-\varepsilon)\, k_{mat} \tag{12}$$

$$k^{\mathrm{hm}} = \left(\frac{\varepsilon}{k_{\mathrm{aq}}} + \frac{1-\varepsilon}{k_{\mathrm{mat}}} \right)^{-1} \tag{13}$$

$$(\rho c_{\mathrm{P}})^{\mathrm{am}} = \varepsilon (\rho c_{\mathrm{P}})_{\mathrm{aq}} + (1-\varepsilon)(\rho c_{\mathrm{P}})_{\mathrm{mat}} \tag{14}$$

where the superscripts am and hm denote the arithmetic and harmonic means, respectively, and the subscripts aq and mat denote water and the solid-phase support layer or interlayer material. Combining the porosity-weighted arithmetic and harmonic mean bounds on thermal conductivity with the porosity-weighted arithmetic volumetric heat capacity, the thermal diffusivity and thermal effusivity of a porous support layer or interlayer are bounded by [70]

$$\frac{k^{\mathrm{hm}}}{(\rho c_{\mathrm{P}})^{\mathrm{am}}} \leqslant \alpha \leqslant \frac{k^{\mathrm{am}}}{(\rho c_{\mathrm{P}})^{\mathrm{am}}} \tag{15}$$

$$\sqrt{k^{\mathrm{hm}}(\rho c_{\mathrm{P}})^{\mathrm{am}}} \leqslant \kappa \leqslant \sqrt{k^{\mathrm{am}}(\rho c_{\mathrm{P}})^{\mathrm{am}}} \tag{16}$$

Figure 3 shows the upper and lower bounds of the thermal diffusivity ($\alpha = k/\rho c_{\mathrm{P}}$) and thermal effusivity ($\kappa = k/\sqrt{\alpha} = \sqrt{k\rho c_{\mathrm{P}}}$) of composites comprising selected porous (a) polymers and (b) inorganic materials filled with water as a function of layer porosity calculated using both the arithmetic and harmonic thermal conductivity bounds. Porosity (ε) increases from 0.0 (filled markers, light line segments) through 0.5 (unfilled markers) to 1.0 (filled marker for water, dark line segments). Upper and lower bounds for α and κ are calculated as a function of porosity using Equations 15 and 16, respectively.

Compared to water, the thermal conductivities and volumetric heat capacities of most polymers are between two- to four-times smaller ($k_{\mathrm{mat}} < k_{\mathrm{aq}}$ and $(\rho c_{\mathrm{P}})_{\mathrm{mat}} < (\rho c_{\mathrm{P}})_{\mathrm{aq}}$, respectively). Consequently, increasing porosity leads to a monotonic increase in composite thermal effusivity for both the porosity-weighted arithmetic and harmonic mean thermal conductivity bounds. For a porosity of 0.50, most polymer-water composites have a thermal effusivity of around 1.0 kW $\mathrm{s}^{\frac{1}{2}}$ m^{-2} K^{-1}, approximately double the thermal effusivity of the solid polymer. The lower bound of composite thermal diffusivity, $k^{\mathrm{hm}}/(\rho c_{\mathrm{P}})^{\mathrm{am}}$, which combines the porosity-weighted harmonic mean thermal conductivity with the arithmetic mean volumetric heat capacity, can decrease as porosity increases if $(\rho c_{\mathrm{P}})^{\mathrm{am}}$ increases faster than k^{hm}.

Many inorganic materials; including titanium dioxide, silicon nitride, and aluminum oxide; have thermal conductivities that are significantly higher than that of water, while having volumetric heat capacities that are two- to four-times smaller than water ($k_{\mathrm{mat}} > k_{\mathrm{aq}}$ and $(\rho c_{\mathrm{P}})_{\mathrm{mat}} < (\rho c_{\mathrm{P}})_{\mathrm{aq}}$, respectively). Consequently, for highly conductive inorganic materials, the upper bound of thermal effusivity, $\sqrt{k^{\mathrm{am}}(\rho c_{\mathrm{P}})^{\mathrm{am}}}$, is not a monotonic function of layer porosity. Compared to polymer-water composites, the thermal diffusivity and thermal effusivity of inorganic material-water composites is highly dependent on layer porosity and structure due to the large differences in thermal conductivity. Similarly, the thermal properties of composite layers incorporating metals, which have thermal conductivity values that are orders of magnitude higher than that of water but volumetric heat capacity values that are similar to water ($k_{\mathrm{mat}} \gg k_{\mathrm{aq}}$ and $(\rho c_{\mathrm{P}})_{\mathrm{mat}} \approx (\rho c_{\mathrm{P}})_{\mathrm{aq}}$, respectively), are also highly dependent on both the porosity and structure of the layer.

4 Temperature Increase during Interfacial Heat Release

The transient heat transfer model developed in Section 2 is solved to analyze how the thermal properties of different materials, outlined in Section 3, impact interfacial temperature during TFC membrane fabrica-

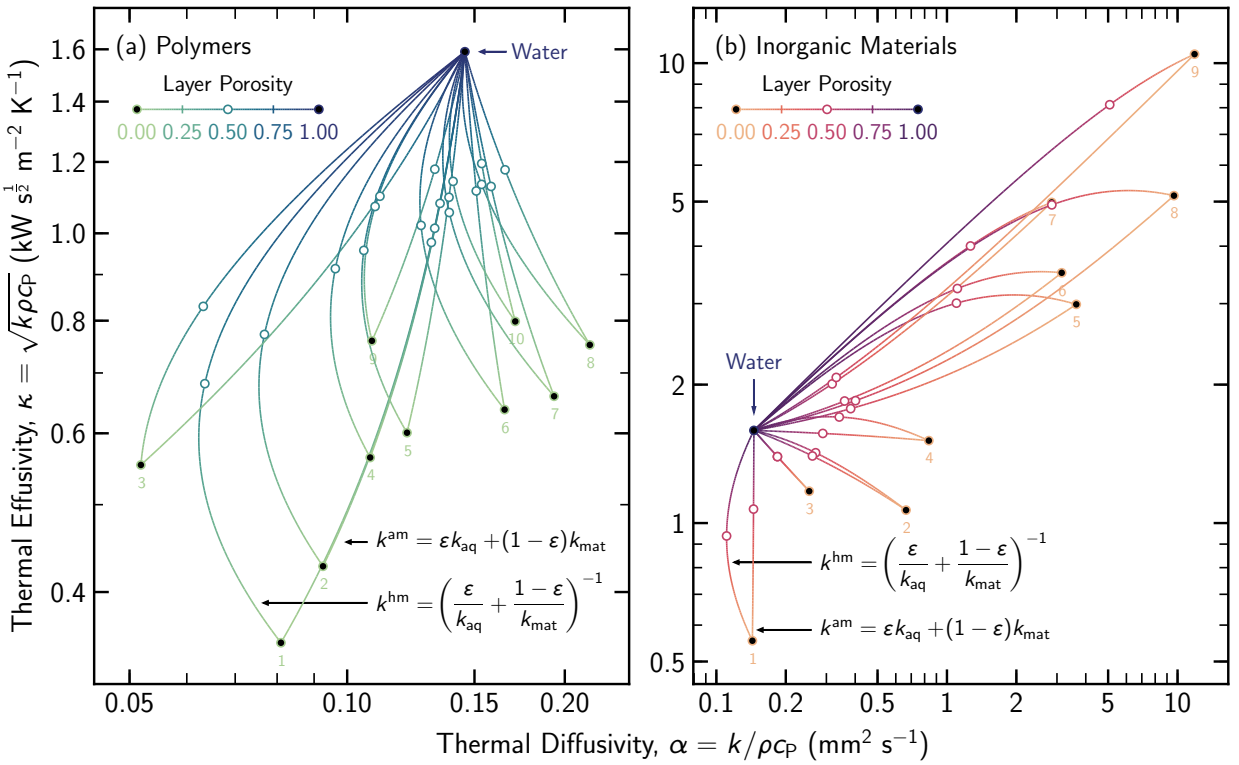

Figure 3: Thermal diffusivity ($\alpha = k/\rho c_P$) and thermal effusivity ($\kappa = k/\sqrt{\alpha} = \sqrt{k\rho c_P}$) bounds for (a) ten polymers and (b) nine inorganic materials impregnated with water as a function of layer porosity. Porosity increases from 0.0 (filled circular marker, light line segments), through 0.5 (unfilled marker), to 1.0 (filled marker, dark segments). The thermal effusivity and diffusivity of the porous matrix is bounded by using the arithmetic and harmonic mean values of the thermal conductivities of the material and water, combined with the arithmetic mean of the volumetric heat capacity. In order of increasing thermal effusivity, the polymers plotted are: (1) polyvinyl chloride, (2) polystyrene, (3) polyvinylidene fluoride, (4) polypropylene, (5) polymethyl methacrylate, (6) polysulfone, (7) polycarbonate, (8) polyimide, (9) polytetrafluoroethylene, and (10) low-density polyethylene; and the inorganic materials plotted are: (1) sulfur, (2) graphite fiber epoxy (perpendicular), (3) boron fiber epoxy (perpendicular), (4) silicon dioxide, (5) pyrolytic graphite (perpendicular), (6) silicon dioxide (perpendicular), (7) titanium dioxide, (8) silicon nitride, and (9) polycrystalline aluminum oxide [62, 66].

tion. Laplace- and, where possible, time-domain solutions for the increase in interfacial temperature are derived for support-free (SFIP), conventional (CIP), and interlayer-modulated (IMIP) interfacial polymerization, which correspond to two-, three-, and four-layer heat transfer systems, respectively. Temperature increase ($u = T - T_{ref}$) is normalized by the reaction-specific diffusion-limited interfacial heat release constant ($q_0\sqrt{t_0}$, units W $s^{\frac{1}{2}}$ m^{-2}), which is described in Section 2.3, giving $\bar{u} = u/(q_0\sqrt{t_0})$. The temperature parameter $\bar{u}$ is a function of reaction time, distance from the reaction interface, and the thermal properties of each layer. Laplace- and time-domain expressions are analyzed to bound the transient behavior of interfacial temperature as a function of fluid and material properties across a range of solvents, support layers, and interlayers for diffusion-limited interfacial heat release (see Appendices A and B for derivations, respectively). Laplace- and time-domain expressions for the transient heat fluxes away from the reaction interface are also determined (Appendix C). Furthermore, the complete Laplace-domain solutions to the transient heat transfer

model developed are numerically inverted to illustrate the temporal evolution of spatial temperature profiles (Section 4.4 and Appendix A).

4.1 Interfacial Temperature during Support-Free Interfacial Polymerization (Two-Layer Heat Transfer)

In SFIP, heat released at the reaction interface is simultaneously transferred into two semi-infinite fluid layers. Layer 1 ($z < 0$) is an organic solution that is immiscible with water, while layer 2 ($z > 0$) is an aqueous solution. The Laplace transform of the temperature increase in layers 1 and 2 for a two-layer heat transfer system ($U_1^{2L}(z,s)$ and $U_2^{2L}(z,s)$, respectively) can be determined by incorporating boundary conditions at $z \to -\infty$, $z = 0$, and $z \to +\infty$ into the general solution for each layer (Equation 9). For a two-layer heat transfer system, the Laplace- and time-domain expressions for interfacial temperature rise during diffusion-limited interfacial heat release ($\bar{U}_{int}^{2L,dl}$ and $\bar{u}_{int}^{2L,dl}$, respectively) are (Appendix A.1)

$$\bar{U}_{int}^{2L,dl}(s) = \frac{\sqrt{\pi}}{s(\kappa_1 + \kappa_2)}$$
$$\bar{u}_{int}^{2L,dl}(t) = \frac{\sqrt{\pi}}{\kappa_1 + \kappa_2} \tag{17}$$

Equation 17 shows that interfacial temperature during diffusion-limited planar interfacial heat release into two semi-infinite fluid layers is constant and inversely proportional to the sum of the thermal effusivities of layers 1 and 2. Figure 4 shows the maximum normalized increase in interfacial temperature ($\bar{u}_{int}^{2L,dl} = u_{int}^{2L,dl}/(q_0\sqrt{t_0})$) as a function of the (a) thermal effusivity ($\kappa_1 = \sqrt{k_1 \rho c_{P,1}}$), (b) thermal conductivity (k_1), and (c) thermal diffusivity ($\alpha_1 = k_1/(\rho_1 c_{P,1})$) of various organic solvents (orange triangles) in a two-layer heat transfer system representing SFIP. Layer 2 is an aqueous solution that is modeled using the thermal properties of water. Increasing the thermal effusivity of the organic solvent used in SFIP increases the rate of heat transfer into the organic solution, driving a reduction in interfacial temperature increase for given interfacial reaction properties.

The thermal effusivities of most organic solvents that are immiscible or only partially miscible with water are relatively similar. Therefore, changing the organic solvent does not have a large impact on the interfacial temperature increase. Increasing κ_1 from 377 to 544 kW $s^{\frac{1}{2}}$ m^{-2} K^{-1} (2,2,4-trimethylpentane and ethyl formate, respectively) leads to a small reduction in $\bar{u}_{int}^{2L,dl}$ from 0.901 to 0.831 K kW^{-1} $s^{-\frac{1}{2}}$ m^2, for a given set of diffusion-limited reaction parameters. Beyond affecting heat transfer outward from the reaction interface, organic solvent choice can impact reaction rate and exothermicity, leading to a change in absolute interfacial temperature. For example, selecting an organic solvent that promotes the partitioning and transport of the aqueous-phase reactant, or increases the exothermicity of the reaction, will lead to an increase in the diffusion-limited interfacial heat release constant ($q_0\sqrt{t_0}$), resulting in a greater absolute increase in interfacial temperature ($u_{int}^{2L,dl}$). Figures 4b and 4c show that interfacial temperature correlates well with the thermal conductivity of the organic solvent (k_1), but correlates quite poorly with its thermal diffusivity (α_1). Note that thermal conductivity, diffusivity, and effusivity are not independent ($\kappa = k/\sqrt{\alpha}$).

4.2 Interfacial Temperature during Conventional Interfacial Polymerization (Three-Layer Heat Transfer)

In CIP, heat released at the reaction interface is initially transferred into layers 1 and 2, and then through layer 2 into layer 3. Layer 1 ($z < 0$) is a semi-infinite organic solution, while finite layer 2 ($0 < z < d_2$) repre-

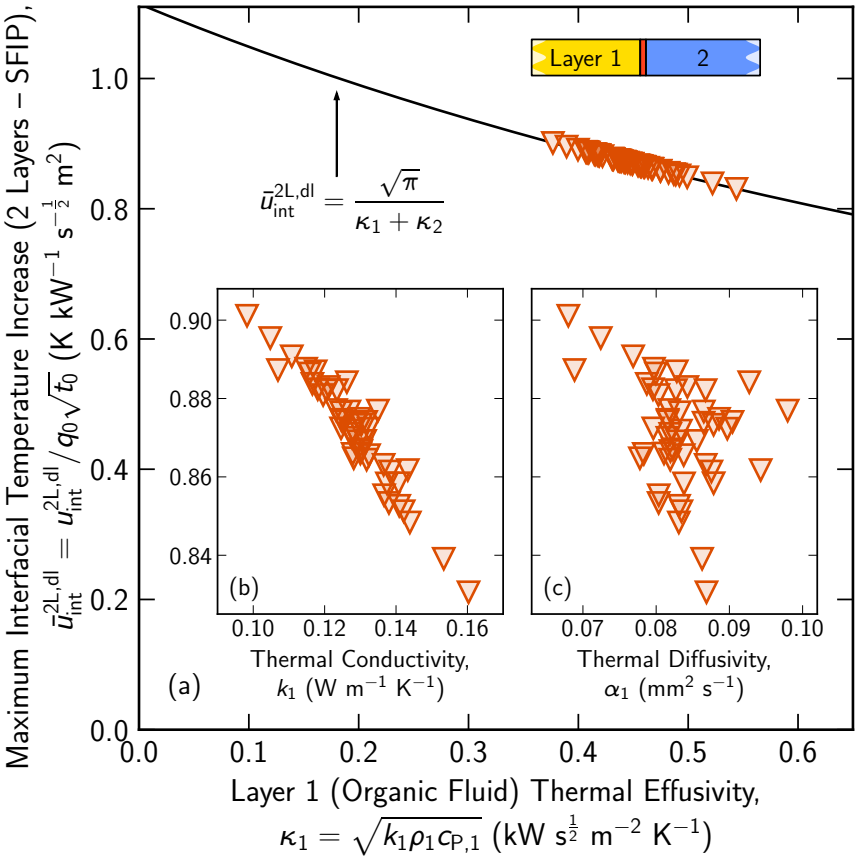

Figure 4: Maximum interfacial temperature increase for diffusion-limited heat release in a two-layer heat transfer system ($\bar{u}_{\text{int}}^{2\text{L,dl}} = u_{\text{int}}^{2\text{L,dl}}/(q_0\sqrt{t_0})$) as a function of layer 1 (a) thermal effusivity ($\kappa_1 = \sqrt{k_1\rho c_{\text{P},1}}$), (b) thermal conductivity (k_1), and (c) thermal diffusivity ($\alpha_1 = k_1/(\rho_1 c_{\text{P},1})$) for 50 organic solvents (orange triangles) that are immiscible or only partially miscible with water (Table E1). Interfacial temperature increase $\bar{u}_{\text{int}}^{2\text{L,dl}}$ as a function of κ_1 (black curve) is calculated assuming that Layer 2 is an aqueous solution with the thermal properties of water ($\kappa_2 = 1.59$ kW s$^{\frac{1}{2}}$ m^{-2} K^{-1}).

sents a porous support layer, comprising a solid support material filled with an aqueous solution, and layer 3 ($z > d_2$) is the semi-infinite bulk aqueous solution. As before, the Laplace transform of the temperature increase in layers 1, 2, and 3 for a three-layer heat transfer system ($U_1^{3\text{L}}(z,s)$, $U_2^{3\text{L}}(z,s)$, and $U_3^{3\text{L}}(z,s)$, respectively) can be determined by incorporating boundary conditions at $z \to -\infty$, $z = 0$, $z = d_2$, and $z \to +\infty$ into the general solution for each layer (Equation 9). For a three-layer heat transfer system, the Laplace transform of interfacial temperature with diffusion-limited interfacial heat release ($\bar{U}_{\text{int}}^{3\text{L,dl}}$) is given by (Appendix A.2)

$$\bar{U}_{\text{int}}^{3\text{L,dl}}(s) = \frac{\sqrt{\pi}}{s(\kappa_1 + \kappa_2)}\left[\frac{1 + \gamma_{2,3}\exp(-2\sqrt{\tau_2 s})}{1 + \gamma_{1,2}\gamma_{2,3}\exp(-2\sqrt{\tau_2 s})}\right] \tag{18}$$

where $\tau_2 = d_2^2/\alpha_2$ is the characteristic timescale for heat conduction through layer 2, which is defined in terms of its thickness (d_2) and thermal diffusivity (α_2), and $\gamma_{i,j} = (\kappa_i - \kappa_j)/(\kappa_i + \kappa_j)$ are thermal effusivity difference-to-sum ratios, noting that $|\gamma_{i,j}| < 1 \; \forall \; i, j \in 1, \ldots, n$ given that $\kappa_i > 0 \; \forall \; i \in 1, \ldots, n$.

Taking the inverse Laplace transform of a series expansion of Equation 18, the time-domain interfacial temperature rise for a three-layer heat transfer system with diffusion-limited interfacial heat release can be expressed as (Appendix B.2)

$$\bar{u}_{\text{int}}^{3\text{L,dl}}(t) = \frac{\sqrt{\pi}}{\kappa_1 + \kappa_2}\left\{1 - \frac{2\kappa_2}{\kappa_1 - \kappa_2}\sum_{j=1}^{\infty}\left[(-\gamma_{1,2}\gamma_{2,3})^j \operatorname{erfc}\left(j\sqrt{\frac{\tau_2}{t}}\right)\right]\right\} \tag{19}$$

The time-domain series solution for $\bar{u}_{\text{int}}^{\text{3L,dl}}$ in Equation 19 converges for any combination of materials and structures given that $|\gamma_{i,j}| < 1 \; \forall \, i, j \in 1, ..., n$. Initial and final interfacial temperatures can be calculated by applying the initial and final value theorems for Laplace transforms to $\bar{U}_{\text{int}}^{\text{3L,dl}}$ giving $\bar{u}_{\text{int},t\to 0^+}^{\text{3L,dl}} = \sqrt{\pi}/(\kappa_1 + \kappa_2)$ and $\bar{u}_{\text{int},t\to\infty}^{\text{3L,dl}} = \sqrt{\pi}/(\kappa_1 + \kappa_3)$, respectively, noting that $\tau_2 > 0$ and that all poles of $s\bar{U}_{\text{int}}^{\text{3L,dl}}$ are in the left complex half-plane.

Figure 5 shows how the maximum normalized interfacial temperature increase in a three-layer heat transfer system ($\bar{u}_{\text{int}}^{\text{3L,dl}} = u_{\text{int}}^{\text{3L,dl}}/(q_0\sqrt{t_0})$) varies as a function of: (a) the thermal effusivity of layer 2 (support layer) in the small time limit ($t \to 0^+$) for ten selected polymers; and (b) the time from the start of the interfacial reaction (t). Layer 1 is the organic solution ($\kappa_1 = \kappa_{\text{org}}$), modeled using the thermal properties of *n*-hexane, throughout. Layer 3 is the aqueous solution (solid curves, $\kappa_3 = \kappa_{\text{aq}}$), modeled as water, and a fabric channel spacer (dashed, $\kappa_3 = \kappa_{\text{fab}}$), modeled as polyethylene terephthalate with a porosity of 0.5 filled with water. The interfacial temperature increase as a function of polymer porosity is calculated assuming volume-averaged arithmetic mean thermal conductivity and volumetric heat capacity values using the thermal properties of the polymer and water. Layer 2 porosity increases from 0.0 (green triangles, green curve segments) through 0.5 (empty circles) to 1.0 (black curve segments). Figure 5c shows the characteristic timescale for heat transfer by conduction $\tau_2 = d_2^2/\alpha_2$ as a function of layer 2 thickness for the ten selected polymers across typical membrane support layer thicknesses of up to 300 μm.

Figure 5 demonstrates that the presence of a polymeric support layer reduces the initial rate of heat conduction away from the reaction interface, leading to a higher interfacial temperature. For a given set of diffusion-limited reaction parameters, the initial increase in interfacial temperature ($\bar{u}_{\text{int},t\to 0}^{\text{3L,dl}} = \sqrt{\pi}/(\kappa_1 + \kappa_2)$) at small times ($t \ll \tau_2$) depends on the thermal effusivity of the organic solvent (layer 1) and the porous polymeric support layer (layer 2). Most materials used in polymeric support layers, and all polymers shown, have a thermal effusivity that is lower than that of water. Consequently, increasing polymer porosity leads to a reduction in the initial temperature rise.

As reaction time increases, relative to the heat conduction timescale for layer 2 (τ_2), interfacial temperature begins to decrease with heat being transferred into layer 3 (aqueous solution or porous fabric channel spacer), which has a higher thermal effusivity than the water-filled polymeric support layer. For diffusion-limited interfacial heat release, at large times ($t \gg \tau_2$), the thermal properties of layer 2 (support layer) cease to impact interfacial temperature ($\bar{u}_{\text{int},t\to\infty}^{\text{3L,dl}} = \sqrt{\pi}/(\kappa_1 + \kappa_3)$) as heat transfer is dominated by conduction away from the reaction interface in layers 1 and 3. Increasing the thickness of the support layer (d_2) leads to a quadratic increase in the characteristic timescale for heat transfer through layer 2 (τ_2), thus extending the duration over which interfacial temperatures remain elevated.

Polymer choice can have a notable impact on both the magnitude of the increase in interfacial temperature and the duration over which it is sustained, particularly if support layer porosity is low. For example, polyvinylidene fluoride (PVDF), which has a thermal effusivity of 0.553 kW $\text{s}^{\frac{1}{2}}$ m^{-2} K^{-1} yields a interfacial temperature increase of 1.82 K kW^{-1} $\text{s}^{-\frac{1}{2}}$ m^2, 21% greater than the corresponding temperature increase for polytetrafluoroethylene (PTFE, $\kappa = 0.760$ kW $\text{s}^{\frac{1}{2}}$ m^{-2} K^{-1}). For highly porous support layers, the thermal effusivity of layer 2 rapidly tends towards that of water (Figure 3a), lowering initial interfacial temperature rise. For a polysulfone (PSF, $\kappa = 0.637$ kW $\text{s}^{\frac{1}{2}}$ m^{-2} K^{-1}) support layer, increasing porosity from 0.25 to 0.75 yields a 27% reduction in the initial interfacial temperature rise from 1.37 kW $\text{s}^{\frac{1}{2}}$ m^{-2} K^{-1} to 0.999 kW $\text{s}^{\frac{1}{2}}$ m^{-2} K^{-1}.

The timescale for heat transfer through typical polymeric support layers, which are approximately 100 μm thick, is similar to the timescale for selective layer formation ($\sim 10^{-1}$ s) in TFC membrane fabri-

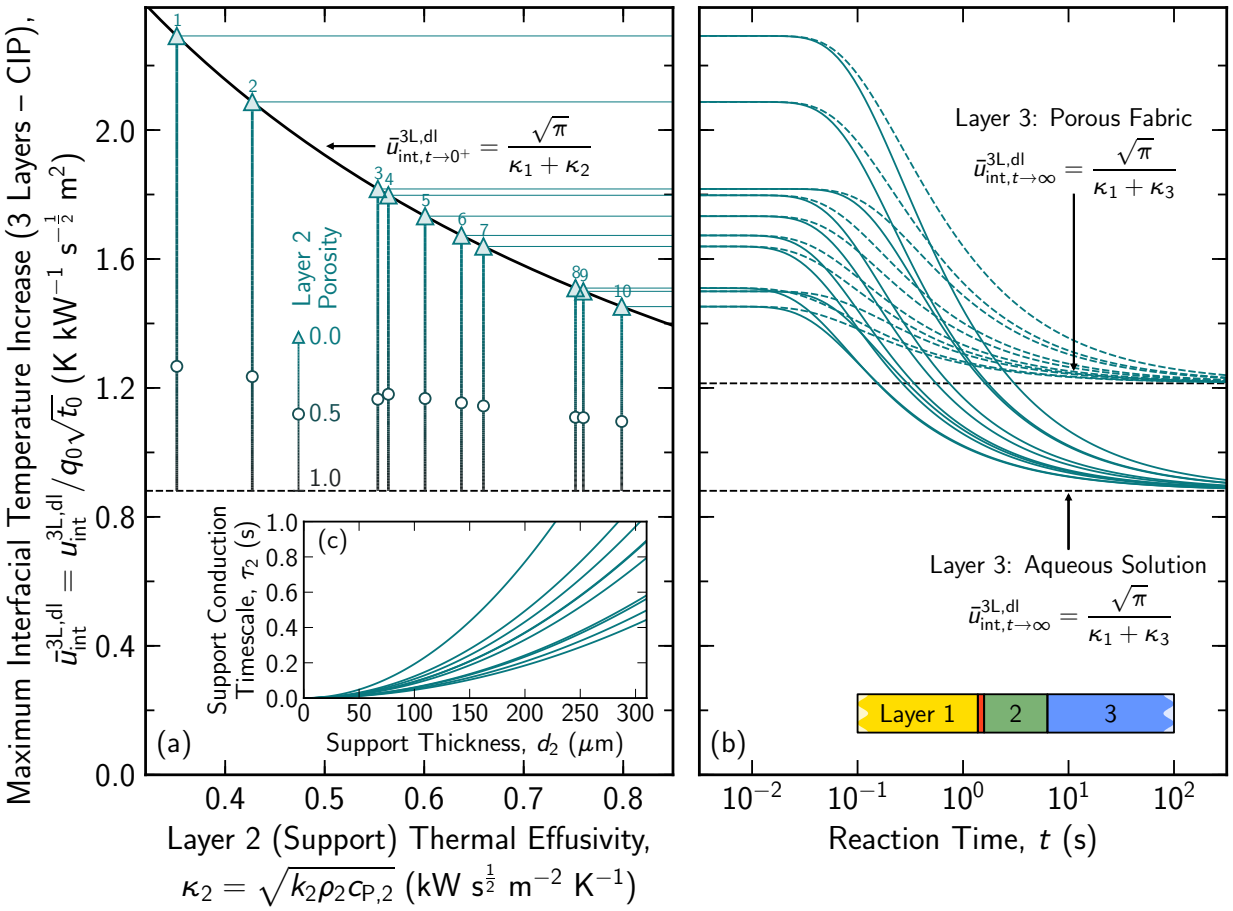

Figure 5: Maximum interfacial temperature increase for diffusion-limited heat release in a three-layer heat transfer system ($\bar{u}^{3L,dl}_{int} = u^{3L,dl}_{int}/(q_0\sqrt{t_0})$) for ten polymers (green triangles) assuming a 100 μm thick support layer as a function of: (a) layer 2 (support) thermal effusivity; and (b) reaction time. (a) Layer 2 porosity increases from 0.0 (triangular markers, green part of vertical lines), through 0.5 (circular markers), to 1.0 (black). The interfacial temperature increase as a function of polymer porosity is calculated assuming volume-averaged arithmetic mean thermal conductivity and volumetric heat capacity values using the thermal properties of the polymer and water. (b) Transient interfacial temperature increase where layer 3 is an aqueous solution (solid curves) or a porous fabric channel spacer fabric comprising polyethylene terephthalate with a porosity of 0.5 filled with water (dashed). (c) Characteristic timescale for heat conduction through layer 2 as a function of layer thickness for ten polymers. Layer 1 is an organic solution, modeled using the thermal properties of *n*-hexane, throughout. In order of increasing thermal effusivity, the polymers plotted are: (1) polyvinyl chloride, (2) polystyrene, (3) polyvinylidene fluoride, (4) polypropylene, (5) polymethyl methacrylate, (6) polysulfone, (7) polycarbonate, (8) polyimide, (9) polytetrafluoroethylene, and (10) low-density polyethylene (Table E1). Interfacial temperature increase $\bar{u}^{3L,dl}_{int}$ as a function of t for each polymer (green curves) is calculated by numerically evaluating the series solution in Equation 19. Black curve indicates the limit for $\bar{u}^{3L,dl}_{int,t\to 0^+}$ as a function of κ_2.

cation [46–49]. Consequently, understanding the temporal dynamics of interfacial temperature in a three-layer heat transfer system is essential to develop a comprehensive understanding of selective layer formation during CIP. Normalizing the change in interfacial temperature for a three-layer heat transfer sys-

tem with diffusion-limited heat release relative to the initial and final limiting temperatures gives $\theta_{\text{int}}^{\text{3L,dl}} = (u_{\text{int}}^{\text{3L,dl}} - u_{\text{int},t\to\infty}^{\text{3L,dl}})/(u_{\text{int},t\to 0^+}^{\text{3L,dl}} - u_{\text{int},t\to\infty}^{\text{3L,dl}})$, where $t \to 0^+ \implies \theta_{\text{int}}^{\text{3L,dl}} \to 1$ and $t \to \infty \implies \theta_{\text{int}}^{\text{3L,dl}} \to 0$. For diffusion-limited interfacial heat release, $u_{\text{int,t}\to 0^+}^{\text{3L,dl}}$ and $u_{\text{int,t}\to\infty}^{\text{3L,dl}}$ are independent of time. Consequently, the Laplace-domain expression for the normalized interfacial temperature change with diffusion-limited interfacial heat release can be written as (Appendix A.3)

$$\Theta_{\text{int}}^{\text{3L,dl}}(s) = \frac{1}{s}\left[\frac{1-\exp(-2\sqrt{\tau_2 s})}{1+\gamma_{1,2}\gamma_{2,3}\exp(-2\sqrt{\tau_2 s})}\right] \tag{20}$$

where $\gamma_{i,j} = (\kappa_i - \kappa_j)/(\kappa_i + \kappa_j)$, noting that $|\gamma_{i,j}| < 1 \;\forall\; i,j \in 1,...,n$ given that $\kappa_i > 0 \;\forall\; i \in 1,...,n$. Using an infinite series expansion for the denominator in Equation 20, a time-domain convergent series expansion for $\theta_{\text{int}}^{\text{3L,dl}}$ can be derived (Appendix B.3):

$$\theta_{\text{int}}^{\text{3L,dl}}(t) = \text{erf}\left(\sqrt{\frac{\tau_2}{t}}\right) + \sum_{j=1}^{\infty}\left[(-\gamma_{1,2}\gamma_{2,3})^j\left\{\text{erf}\left[(j+1)\sqrt{\frac{\tau_2}{t}}\right] - \text{erf}\left(j\sqrt{\frac{\tau_2}{t}}\right)\right\}\right] \tag{21}$$

Figure 6a shows the normalized interfacial temperature change for a three-layer heat transfer system with diffusion-limited interfacial heat release ($\theta_{\text{int}}^{\text{3L,dl}}$) as a function of normalized reaction time (t/τ_2) for 9350 combinations of thermal effusivity spanning 50 organic solvents (layer 1) and 17 water-filled porous polymers (layer 2) with 11 equally spaced porosity values (ε_2) ranging from 0.0 (light green curves) to 1.0 (dark blue). In each case, layer 3 is an aqueous solution modeled using the thermal properties of water. The first term in Equation 21, $\theta_{\text{int},\mathcal{O}(\gamma^0)}^{\text{3L,dl}} = \text{erf}(\sqrt{\tau_2/t})$, which is zeroth order in γ, is shown (solid black curve) along with variations of $\pm 10\%$ in normalized reaction time (dashed). Figure 6b shows the magnitude of the thermal effusivity difference-to-sum ratios $\gamma_{1,2}$ (left triangles) and $\gamma_{2,3}$ (right triangles) as a function of the arithmetic mean thermal effusivity for each combination of adjacent layers relative to the thermal effusivity of water, with ε_2 increasing from 0.0 (light triangles) to 1.0 (dark blue). Figure 6c shows the deviation between the sum of first two terms in the expansion of $\theta_{\text{int}}^{\text{3L,dl}}$ (Equation 21), $\theta_{\text{int},\mathcal{O}(\gamma^2)}^{\text{3L,dl}} = \text{erf}(\sqrt{\tau_2/t}) - \gamma_{1,2}\gamma_{2,3}[\text{erf}(2\sqrt{\tau_2/t}) - \text{erf}(\sqrt{\tau_2/t})]$, which is second order in γ, and the full solution as a function of normalized reaction time.

In typical TFC membrane fabrication using CIP, where layer 2 (support layer) is a porous polymer, the magnitude of the product of the thermal effusivity difference-to-sum ratios ($|\gamma_{1,2}\gamma_{2,3}|$) is small, as the thermal effusivity of layer 2 is similar to that of layer 1 or layer 3 (Figure 6b). For example, in a three-layer heat transfer system comprising a *n*-hexane solution ($\kappa_1 = 0.422$ kW s$^{\frac{1}{2}}$ m^{-2} K^{-1}), a water-filled polysulfone support layer ($\kappa_2 = 1.11$ kW s$^{\frac{1}{2}}$ m^{-2} K^{-1} with $\varepsilon_2 = 0.50$ assuming arithmetic mean thermal properties), and a bulk aqueous solution ($\kappa_3 = 1.59$ kW s$^{\frac{1}{2}}$ m^{-2} K^{-1}), the product of the thermal effusivity difference-to-sum ratios ($\gamma_{1,2}\gamma_{2,3}$) is 0.08. For $|\gamma_{1,2}\gamma_{2,3}| \ll 1$, normalized interfacial temperature change is broadly approximated by the first term in Equation 21, $\theta_{\text{int},\mathcal{O}(\gamma^0)}^{\text{3L,dl}} = \text{erf}(\sqrt{\tau_2/t})$, which is independent of $\gamma_{1,2}$ and $\gamma_{2,3}$ (Figure 6a). Across the 9350 combinations of typical layer 1, 2, and 3 thermal effusivities, 64% are within a normalized reaction time of $\pm 10\%$ of the zeroth-order approximation for $\theta_{\text{int},\mathcal{O}(\gamma^0)}^{\text{3L,dl}}$ for $1 < t/\tau_2 < 10$.

Figure 6c highlights the effectiveness of the second-order expression $\theta_{\text{int},\mathcal{O}(\gamma^2)}^{\text{3L,dl}} = \text{erf}(\sqrt{\tau_2/t}) - \gamma_{1,2}\gamma_{2,3}[\text{erf}(2\sqrt{\tau_2/t}) - \text{erf}(\sqrt{\tau_2/t})]$ in capturing temporal heat transfer dynamics in CIP accurately for a wide range of potential support materials and over several decades in normalized reaction time. The normalized interfacial temperature change for more than 97% of the 9350 layer 1, 2, and 3 material combina-

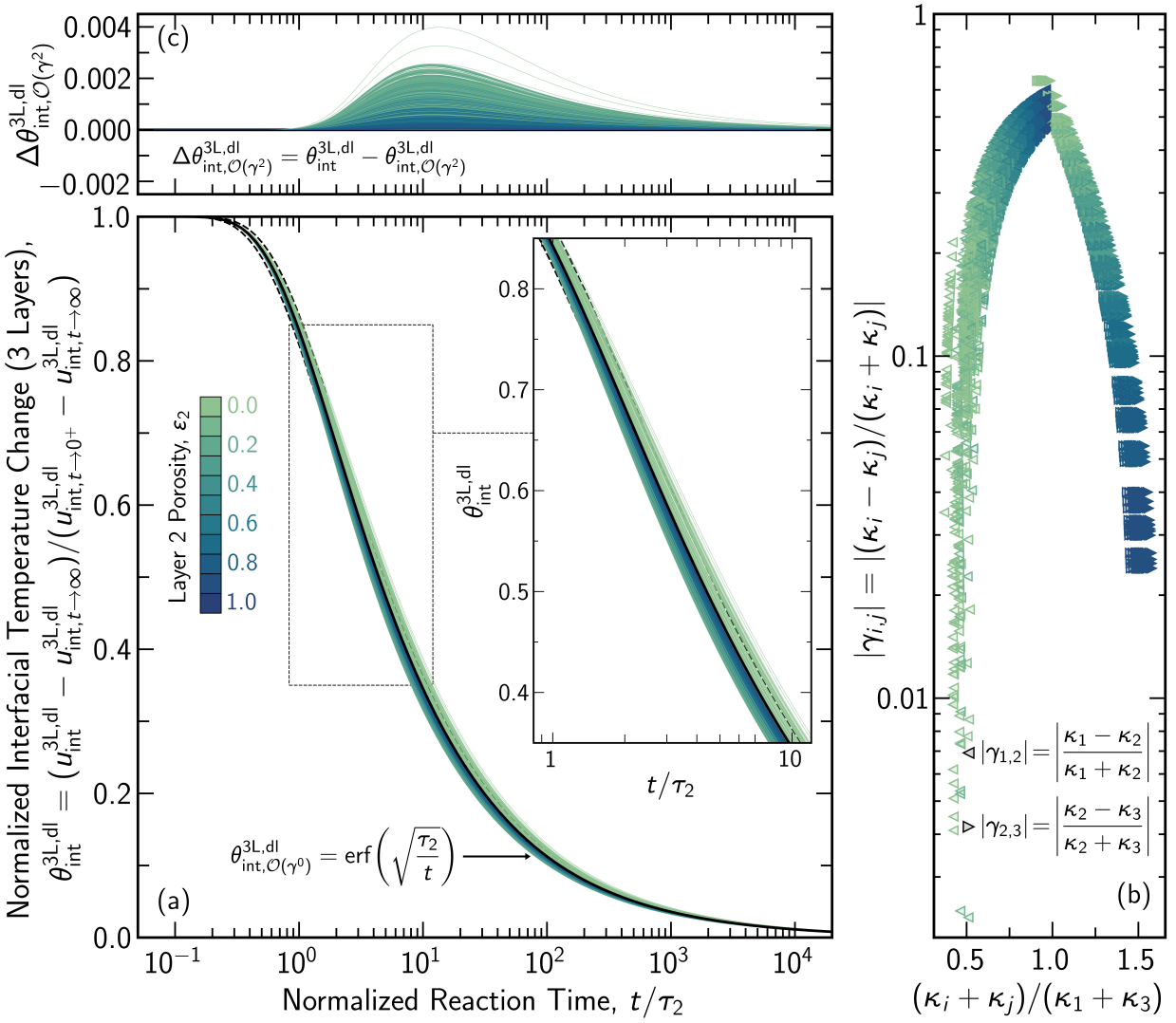

Figure 6: (a) Normalized interfacial temperature change, $\theta^{3L,dl}_{int} = (u^{3L,dl}_{int} - u^{3L,dl}_{int,t\to\infty})/(u^{3L,dl}_{int,t\to 0^+} - u^{3L,dl}_{int,t\to\infty})$, as a function of normalized reaction time (t/τ_2) for a combination of 50 organic solvents (layer 1) and 17 polymers (layer 2), with polymer porosity ranging from 0.0 (light green curves) to 1.0 (dark blue) in increments of 0.1 in each case (Table E1). The first term in the expansion of $\theta^{3L,dl}_{int}$ (Equation 21) in $\gamma_{1,2}\gamma_{2,3}$ is shown (solid black curve) along with variations of $\pm 10\%$ in normalized reaction time (dashed). Normalized interfacial temperature change $\theta^{3L,dl}_{int}$ as a function of t/τ_2 for each organic solvent-polymer-porosity combination (green to blue curves) is calculated by numerically evaluating the time-domain series solution (Equation 21). (b) Magnitude of thermal effusivity difference-to-sum ratios $\gamma_{1,2}$ (left triangles) and $\gamma_{2,3}$ (right triangles) for each organic solvent-polymer-porosity combination. (c) Difference between $\theta^{3L,dl}_{int}$ and the sum of the first two terms in its expansion ($\theta^{3L,dl}_{int,\mathcal{O}(\gamma^2)}$) as a function of normalized reaction time.

tions are within a normalized reaction time of $\pm 1\%$ of $\theta^{3L,dl}_{int,\mathcal{O}(\gamma^2)}$ for $1 < t/\tau_2 < 10$. Figure 6c shows that $\theta^{3L,dl}_{int,\mathcal{O}(\gamma^2)}$ provides a highly accurate, yet relatively simple, approximation of interfacial temperature dynamics, with a maximum deviation ($\Delta\theta^{3L,dl}_{int,\mathcal{O}(\gamma^2)} = \theta^{3L,dl}_{int} - \theta^{3L,dl}_{int,\mathcal{O}(\gamma^2)}$) of 4.0×10^{-3} compared to the full solution.

For all combinations of materials, $\theta^{3L,dl}_{int,\mathcal{O}(\gamma^2)}$ yields an underestimate of $\theta^{3L,dl}_{int}$ as the largest neglected term ($\theta^{3L,dl}_{int,\mathcal{O}(\gamma^4)} - \theta^{3L,dl}_{int,\mathcal{O}(\gamma^2)} = \gamma^2_{1,2}\gamma^2_{2,3}[\text{erf}(3\sqrt{\tau_2/t}) - \text{erf}(2\sqrt{\tau_2/t})]$), the third term in Equation 21, is positive regardless of the thermal effusivities of layers 1, 2, and 3 (Appendix B.3).

4.3 Interfacial Temperature during Interlayer-Modulated Interfacial Polymerization (Four-Layer Heat Transfer)

In IMIP, heat released at the reaction interface is initially transferred into layers 1 and 2, through layer 2 into layer 3, and ultimately through layers 2 and 3 into layer 4. Layer 1 ($z < 0$) is a semi-infinite organic solution; while finite layers 2 ($0 < z < d_2$) and 3 ($d_2 < z < d_2 + d_3$) represent a porous interlayer and a porous support layer, respectively; and layer 4 ($z > d_2 + d_3$) is the semi-infinite bulk aqueous solution. As before, the Laplace transform of the temperature increase in layers 1, 2, 3, and 4 for a four-layer heat transfer system ($U^{4L}_1(z,s)$, $U^{4L}_2(z,s)$, $U^{4L}_3(z,s)$, and $U^{4L}_4(z,s)$, respectively) can be determined by incorporating boundary conditions at $z \to -\infty$, $z = 0$, $z = d_2$, $z = d_2 + d_3$, and $z \to +\infty$ into the general solution for each layer (Equation 9). For a four-layer heat transfer system, the Laplace transform of temperature at the reaction interface with diffusion-limited interfacial heat release ($\bar{U}^{4L,dl}_{int}$) is (Appendix A.4)

$$\bar{U}^{4L,dl}_{int}(s) = \frac{\sqrt{\pi}}{s(\kappa_1+\kappa_2)}\left\{\frac{1+\gamma_{2,3}\exp(-2\sqrt{\tau_2 s})+\gamma_{2,3}\gamma_{3,4}\exp(-2\sqrt{\tau_3 s})+\gamma_{3,4}\exp[-2(\sqrt{\tau_2 s}+\sqrt{\tau_3 s})]}{1+\gamma_{1,2}\gamma_{2,3}\exp(-2\sqrt{\tau_2 s})+\gamma_{2,3}\gamma_{3,4}\exp(-2\sqrt{\tau_3 s})+\gamma_{1,2}\gamma_{3,4}\exp[-2(\sqrt{\tau_2 s}+\sqrt{\tau_3 s})]}\right\} \tag{22}$$

where $\gamma_{i,j} = (\kappa_i - \kappa_j)/(\kappa_i + \kappa_j)$, noting that $|\gamma_{i,j}| < 1 \; \forall \; i, j \in 1, ..., n$ given that $\kappa_i > 0 \; \forall \; i \in 1, ..., n$. Initial and final interfacial temperatures can be calculated by applying the initial and final value theorems for Laplace transforms to $\bar{U}^{4L,dl}_{int}$, giving $\bar{u}^{4L,dl}_{int,t\to 0^+} = \sqrt{\pi}/(\kappa_1+\kappa_2)$ and $\bar{u}^{4L,dl}_{int,t\to\infty} = \sqrt{\pi}/(\kappa_1+\kappa_4)$, respectively, noting that $\tau_2 > 0$, $\tau_3 > 0$, and that all poles of $s\bar{U}^{4L,dl}_{int}$ are in the left complex half-plane. In IMIP, an intermediate time ($\tau_2 \ll t \ll \tau_3$) limit for interfacial temperature increase exists provided that $\tau_2 \ll \tau_3$. Simultaneous applying final ($t/\tau_2 \to \infty$) and initial ($t/\tau_3 \to 0^+$) time limits gives $\bar{u}^{4L,dl}_{int,\tau_3 \ll t \ll \tau_3} = \sqrt{\pi}/(\kappa_1+\kappa_3)$ (Appendix A.4).

Figure 7 shows the maximum normalized interfacial temperature increase for diffusion-limited heat release in a four-layer heat transfer system as a function of (a) layer 2 (interlayer) thermal effusivity for ten inorganic materials (pink left triangles) and ten metals (blue right) and (b) reaction time. In each case, layer 2 is 100 nm thick, layer 1 is an organic solution (*n*-hexane, $\kappa_1 = 0.422$ kW s$^{\frac{1}{2}}$ m^{-2} K^{-1}), layer 3 is a 100 μm thick polymeric support layer (polysulfone, $\kappa_3 = 0.637$ kW s$^{\frac{1}{2}}$ m^{-2} K^{-1}, $\tau_3 = 6.06 \times 10^{-2}$ s), and layer 4 is an aqueous solution (water, $\kappa_3 = 1.59$ kW s$^{\frac{1}{2}}$ m^{-2} K^{-1}). Figure 7c shows the characteristic timescale for heat transfer by conduction $\tau_2 = d_2^2/\alpha_2$ as a function of layer 2 thickness for the ten selected inorganic materials and metals across typical membrane interlayer thicknesses from 1 nm to 1 μm.

Figure 7a demonstrates that many commonly used interlayer materials, particularly metals, can drastically reduce initial interfacial temperatures in IMIP due to their high thermal effusivities. For materials with high κ values, initial temperature is a strong function of interlayer porosity and structure due to the large difference between many commonly used inorganic materials or metals and water (Figure 3b). For example, for an interlayer composed of aligned copper nanostrands with a porosity of 0.75, $\kappa_2^{am} = 20.0$ kW s$^{\frac{1}{2}}$ m^{-2} K^{-1} (conductors-in-parallel approximation for nanomaterials aligned perpendicular to the reaction interface), while $\kappa_2^{hm} = 1.80$ kW s$^{\frac{1}{2}}$ m^{-2} K^{-1} (conductors-in-series approximation for nanomaterials aligned parallel to the interface). This 11-fold reduction in thermal effusivity as the interlayer structure changes from perpendicular- to planar-aligned nanostrands yields a 9-fold increase in initial interfacial temperature increase ($\bar{u}^{4L,dl}_{int,t\to 0^+}$) from 0.0866 to 0.799 K kW^{-1} s$^{-\frac{1}{2}}$ m^2 for a given diffusion-limited interfacial heat release constant. In the case where the conductors-in-parallel approximation applies, incor-

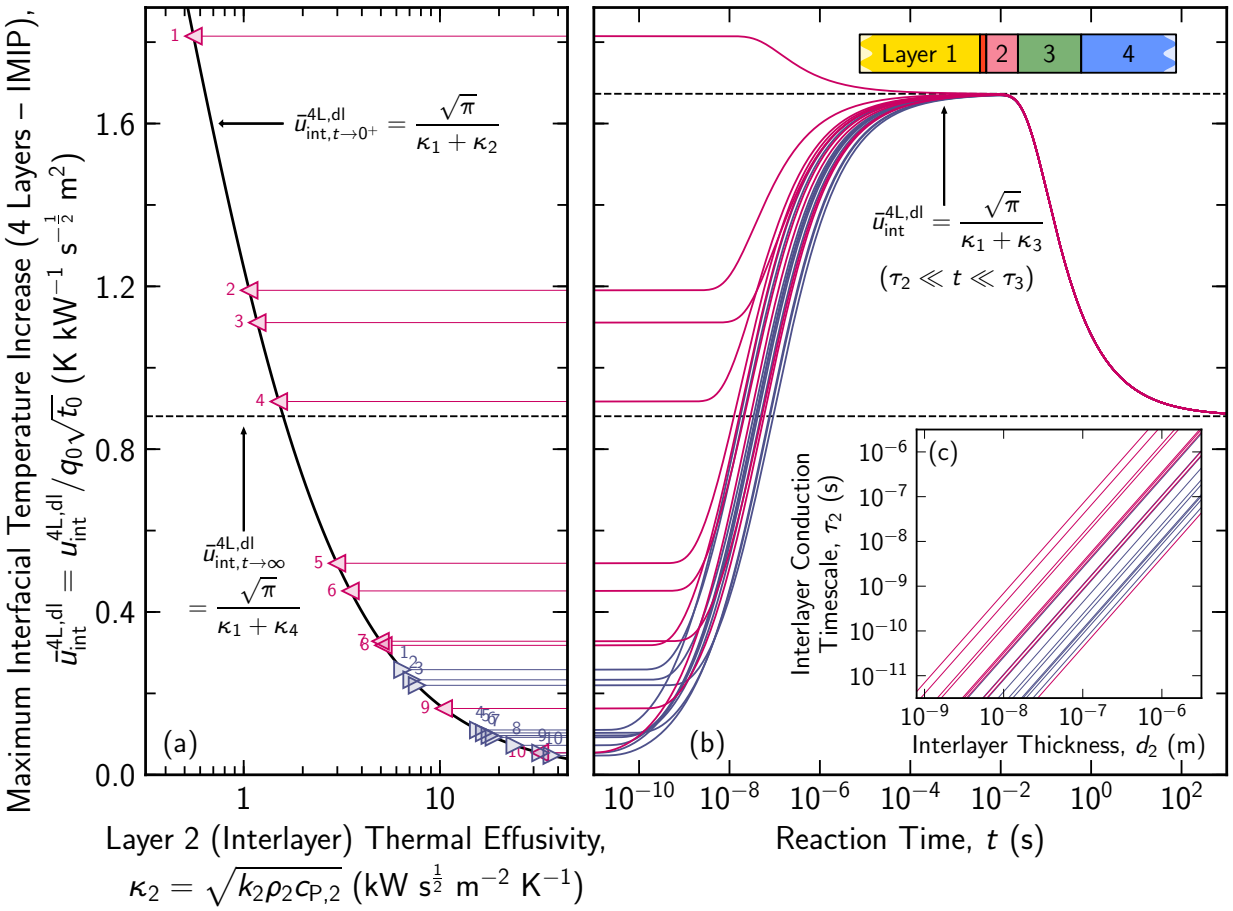

Figure 7: Maximum interfacial temperature increase for diffusion-limited heat release in a four-layer heat transfer system ($\bar{u}^{4L,dl}_{int} = u^{4L,dl}_{int}/(q_0\sqrt{t_0})$) as a function of (a) layer 2 (interlayer) thermal effusivity for ten inorganic materials (pink left triangles) and ten metals (blue right) and (b) reaction time, assuming that interlayer and polysulfone support layer are 100 nm and 100 μm thick, respectively. (c) Characteristic timescale for heat conduction through layer 2 as a function of layer thickness for a range of inorganic materials (pink lines) and metals (blue). In order of increasing thermal effusivity (left to right), the inorganic materials plotted are: (1) sulfur, (2) graphite fiber epoxy (perpendicular), (3) boron fiber epoxy (perpendicular), (4) silicon dioxide, (5) pyrolytic graphite (perpendicular), (6) silicon dioxide (perpendicular), (7) titanium dioxide, (8) silicon nitride, (9) polycrystalline aluminum oxide, and (10) silicon carbide; and the metals plotted are (1) zirconium, (2) titanium, (3) stainless steel, (4) magnesium, (5) iron, (6) zinc, (7) molybedenum, (8) aluminum, (9) silver, and (10) copper (Table E1). Interfacial temperature increase $\bar{u}^{4L,dl}_{int}$ as a function of t for each inorganic material (pink curves) and metal (blue) is calculated by numerically inverting the Laplace-domain solution in Equation 22. Black curve indicates the limit for $\bar{u}^{4L,dl}_{int,t\to 0^+}$ as a function of κ_2.

porating a copper nanostrand interlayer with a porosity of 0.75, results in a 95% reduction in $\bar{u}^{4L,dl}_{int,t\to 0^+}$ from 1.67 to 0.0866 K kW^{-1} s$^{-\frac{1}{2}}$ m^2 during IMIP compared to CIP with a polysulfone support layer.

Figure 7b shows that interfacial temperatures increases rapidly with reaction time as heat is transferred through the interlayer (layer 2) and into the support layer (layer 3), because polymeric support layers have significantly lower thermal effusivities than most inorganic or metallic interlayer materials ($\kappa_2 \gg \kappa_3$ for inorganic materials 5–10 and all metals shown). For intermediate reaction times ($\tau_2 \ll t \ll \tau_3$) between the

characteristic timescale for heat transfer through the interlayer (τ_2) and support layer (τ_3), interfacial temperature is controlled by the thermal properties of the membrane support layer. Ultimately, as time increases beyond τ_3, heat is transferred through both the interlayer and support layer into the semi-infinite aqueous fluid layer, causing the normalized interfacial temperature to approach its large time asymptotic value ($\bar{u}^{\mathrm{4L,dl}}_{\mathrm{int},t\to\infty} = \sqrt{\pi}/(\kappa_1+\kappa_4)$). In IMIP, layer 3 (support layer) typically has a lower thermal effusivity than both layer 2 (interlayer) and layer 4 (aqueous solution) and a significantly higher characteristic heat conduction timescale than layer 2 ($\kappa_3 < \kappa_2$, $\kappa_3 < \kappa_4$, and $\tau_3 \gg \tau_2$). Consequently, the normalized interfacial temperature increase ($\bar{u}^{\mathrm{4L,dl}}_{\mathrm{int}}$) initially rises from $\sqrt{\pi}/(\kappa_1+\kappa_2)$ when $t > \tau_2$, reaching a maximum value of $\sqrt{\pi}/(\kappa_1+\kappa_3)$ before decreasing to $\sqrt{\pi}/(\kappa_1+\kappa_4)$ as reaction time increases beyond τ_3. The porosity and structure of interlayer materials also have a significant impact on the thermal diffusivity and therefore the characteristic heat transfer timescale for conduction through the interlayer (Figure 3b). For example, for aligned copper nanostrands filled with water with a porosity of 0.75, $\alpha_2^{\mathrm{am}} = 25.3$ mm^2 s^{-1}, while $\alpha_2^{\mathrm{hm}} = 0.203$ mm^2 s^{-1}. This yields a 125-fold increase in the characteristic heat transfer timescale when the conductors-in-series approximation applies compared to the conductors-in-parallel structure.

Although inorganic materials and metals can have a large impact on initial temperature, membrane interlayers are typically thin (< 100 nm), which combined with the high thermal diffusivities of these materials (Figure 2) leads to small characteristic heat transfer timescales ($\tau_2 < 10^{-6}$ s). Consequently, the impact of thin membrane interlayers with higher thermal diffusivities on interfacial temperature is confined to the very early stages of the IP reaction. At longer reaction times $t \gg \tau_2$, the rate of conduction through the interlayer is limited by heat transfer in subsequent adjacent layers, including the support layer (layer 3) and, ultimately, the aqueous solution (layer 4). For small times, the rate of interfacial heat release is dominated by reaction kinetics, and monomer diffusion limitations are minimal [47]. However, the diffusion-limited dynamics presented here, which assume instantaneous reaction kinetics, continue to provide a robust upper bound for interfacial temperature at small time.

4.4 Spatial Temperature Increase during Interfacial Heat Release

As heat released during SFIP, CIP, and IMIP is conducted away from the reaction interface, temperatures rise in both fluid layers and any support layers (CIP and IMIP) or interlayers (IMIP) present. Solving the transient heat transfer model developed in Section 2 allows spatial variations in temperature increase to be captured as a function of both position (z, with $z = 0$ at the reaction interface) and time (t).

For diffusion-limited interfacial heat release in a three-layer heat transfer system, the Laplace transform of temperature as a function of distance from the reaction interface in layers 1, 2, and 3 ($\bar{U}_1^{\mathrm{3L,dl}}(z,s)$, $\bar{U}_2^{\mathrm{3L,dl}}(z,s)$, and $\bar{U}_3^{\mathrm{3L,dl}}(z,s)$, respectively) is given by (Appendix A.2)

$$\bar{U}_1^{\mathrm{3L,dl}}(z,s) = \frac{\sqrt{\pi}}{sX^{\mathrm{3L,den}}}\left[\kappa_2+\kappa_3+(\kappa_2-\kappa_3)\exp(-2\sqrt{\tau_2 s})\right]\exp\left(z\sqrt{\frac{s}{\alpha_1}}\right) \tag{23}$$

$$\bar{U}_2^{\mathrm{3L,dl}}(z,s) = \frac{\sqrt{\pi}}{sX^{\mathrm{3L,den}}}\left[(\kappa_2-\kappa_3)\exp\left(-2\sqrt{\tau_2 s}+z\sqrt{\frac{s}{\alpha_2}}\right)+(\kappa_2+\kappa_3)\exp\left(-z\sqrt{\frac{s}{\alpha_2}}\right)\right] \tag{24}$$

$$\bar{U}_3^{\mathrm{3L,dl}}(z,s) = \frac{\sqrt{\pi}}{sX^{\mathrm{3L,den}}}\left\{2\kappa_2\exp\left[-\left(1-\sqrt{\frac{\alpha_2}{\alpha_3}}\right)\sqrt{\tau_2 s}-z\sqrt{\frac{s}{\alpha_3}}\right]\right\} \tag{25}$$

$$X^{\mathrm{3L,den}} = (\kappa_1+\kappa_2)(\kappa_2+\kappa_3)+(\kappa_1-\kappa_2)(\kappa_2-\kappa_3)\exp(-2\sqrt{\tau_2 s}) \tag{26}$$

where $\tau_2 = d_2^2/\alpha_2$ is the characteristic timescale for heat conduction through layer 2 (support layer) and

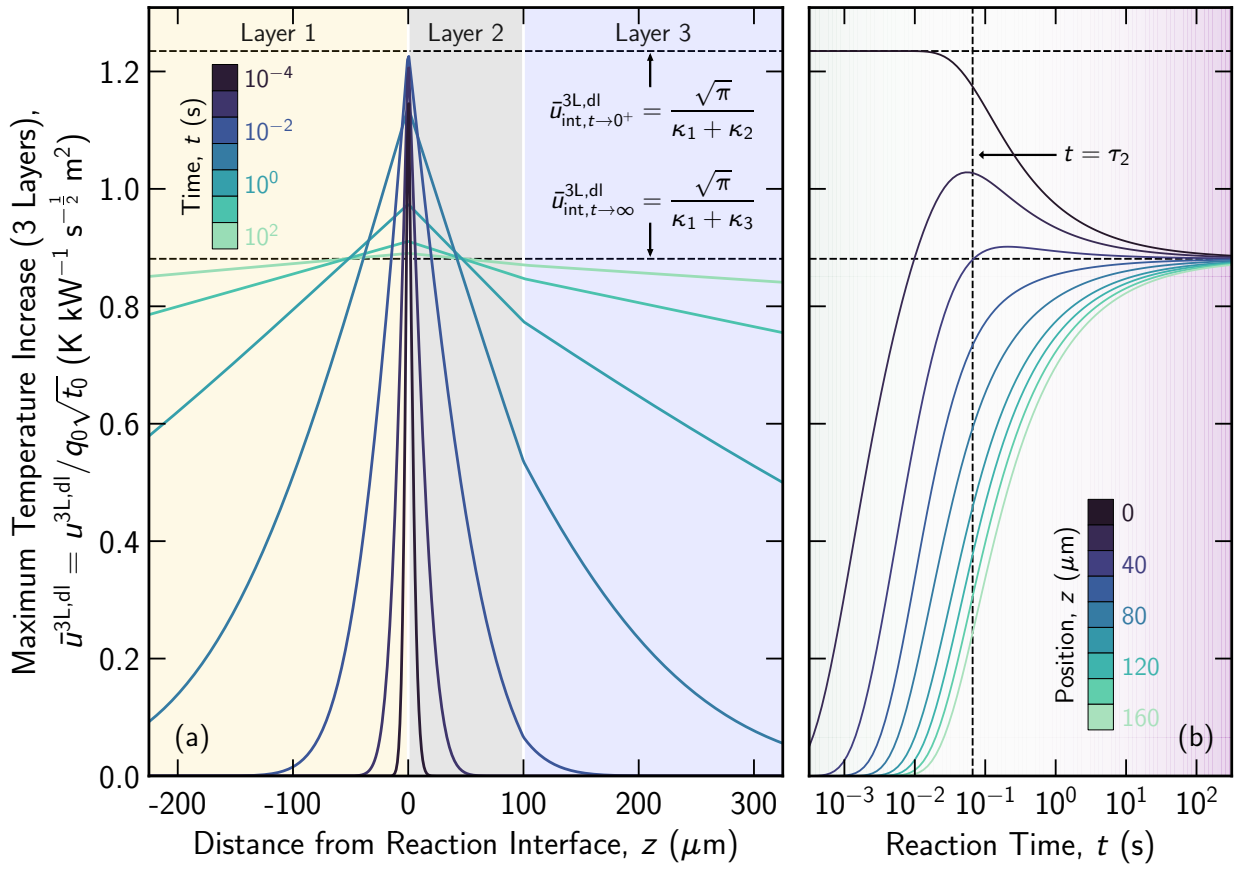

Figure 8: Maximum temperature increase ($\bar{u}^{3L,dl} = u^{3L,dl}/(q_0\sqrt{t_0})$) as a function of (a) distance from the reaction interface and (b) reaction time for diffusion-limited heat release in a three-layer heat transfer system comprising an organic solution (layer 1, *n*-hexane, yellow shading), a 100 μm thick support layer with porosity 0.25 (layer 2, polysulfone, gray), and an aqueous solution (layer 3, water, blue). (a) Heat is conducted into layers 1 and 2 and then through layer 2 into layer 3 as reaction time increases from 10^{-4} s (dark purple lines) to 10^2 s (light green). (b) Maximum temperature increase with increasing distance from the reaction interface from 0 μm (dark purple lines) to 200 μm (light green) towards the aqueous fluid. Temperature increase at the reaction interface ($\bar{u}^{3L,dl}_{int}$) decreases from $\sqrt{\pi}/(\kappa_1+\kappa_2)$ for $t \ll \tau_2$ (upper dashed line) to $\sqrt{\pi}/(\kappa_1+\kappa_3)$ for $t \gg \tau_2$ (lower dashed line). Temperature increase is calculated by numerically inverting the Laplace-domain solutions for $\bar{U}_1^{3L,dl}$, $\bar{U}_2^{3L,dl}$, and $\bar{U}_3^{3L,dl}$ in the regions $z < 0$, $0 < z < d_2$, and $z > d_2$ using Equations 23, 24, and 25, respectively.

$X^{3L,den}$ is a common denominator for a three-layer heat transfer system.

Figure 8 shows the maximum normalized temperature increase ($\bar{u}^{3L,dl} = u^{3L,dl}/(q_0\sqrt{t_0})$) as a function of (a) distance from the reaction interface (z) and (b) reaction time (t) for diffusion-limited heat release in a three-layer heat transfer system comprising a semi-infinite organic layer (layer 1, *n*-hexane, yellow shading), a 100 μm thick support layer with a porosity of 0.25 (layer 2, polysulfone, gray), and a semi-infinite aqueous (layer 3, water, blue). (a) The temporal evolution of spatial temperature profiles is plotted as heat is conducted into layers 1 and 2 and then through layer 2 into layer 3 as reaction time increases from 10^{-4} s (dark purple lines) to 10^2 s (light green). (b) Temperature decreases with increasing distance from the reaction interface from 0 μm (dark purple lines) through 100 μm (blue, edge of the support layer)

to 200 μm (light green) towards the aqueous fluid. Interfacial temperature increase ($\bar{u}^{3L,dl}$) decreases from $\sqrt{\pi}/(\kappa_1+\kappa_2)$ for $t \ll \tau_2$ to $\sqrt{\pi}/(\kappa_1+\kappa_3)$ for $t \gg \tau_2$.

Figure 8a highlights temporal evolution of spatial temperature profile in a three-layer heat transfer system representing CIP. For purely diffusion-limited interfacial heat release, there is an instantaneous increase in interfacial temperature that is inversely proportional to the sum of the thermal effusivities of the organic solution and the polymeric support layer ($\sqrt{\pi}/(\kappa_1+\kappa_2)$) as the reaction begins ($t \to 0^+$). Initially, the temperature increase in the aqueous solution (layer 3, $z > d_2$) is negligible. As time elapses, heat is conducted through the support layer, which has a characteristic heat transfer timescale of 6.6×10^{-2} s, and into the aqueous fluid. The discontinuity of the temperature gradient at the interface between the polymeric support layer and the aqueous solution ($z = d_2$) arises due to the unequal thermal effusivities of layers 2 and 3 (1.01 kW $s^{\frac{1}{2}}$ m^{-2} K^{-1} and 1.59 kW $s^{\frac{1}{2}}$ m^{-2} K^{-1}, respectively) with the reduction in temperature gradient corresponding to an increase in the thermal effusivity of the layer. As reaction time increases ($t \gg \tau_2$) the rate of interfacial heat release continues to decrease and the temperature gradient at the reaction interface dissipates.

Figure 8b shows how temperature decreases monotonically moving away from the reaction interface. The temperature increase is initially zero everywhere except the reaction interface ($\bar{u}^{3L,dl}_{z\neq 0, t\to 0^+} = 0$). As heat is released from the diffusion-limited interfacial reaction, temperature increases rapidly in the immediate vicinity of the reaction interface ($\sqrt{\alpha_1 t} < z < \sqrt{\alpha_2 t}$). As the rate of interfacial heat release decreases and temperature gradients in the support layer dissipate, the temperature increase near the reaction interface approaches its long time limit $\sqrt{\pi}/(\kappa_1+\kappa_3)$. As discussed in Section 4.2, at long times ($t \gg \tau_2$, temperature gradients in the support layer are negligible and the temperature in the vicinity of the reaction interface is governed by conduction in the semi-infinite organic and aqueous solutions (layers 1 and 3, respectively).

4.5 Implications of Elevated Interfacial Temperature during Membrane Fabrication

Elevated interfacial temperatures can alter the chemical structure and physical morphology of the polymeric selective layer central to TFC membranes. In most cases, higher temperatures reduce interfacial stability by lowering fluid viscosity and the interfacial tension between the aqueous and organic phases near the reaction zone [32, 33]. Increased interfacial temperature can also promote the diffusion of monomers to the reaction interface while increasing the diffusion of polymerization byproducts, such as acids, away from the reaction zone. Lower fluid viscosities and interfacial tension coupled with higher temperature or chemical gradients can promote thermocapillary and solutocapillary instabilities. Increased interfacial temperatures can also accelerate the degassing of aqueous and organic solutions near the reaction interface, leading to the formation of nanobubbles [36, 37]. In addtition, elevated temperatures can reduce the flexural modulus of the incipient polymer film, increasing its crumpling propensity.

Experimental studies have shown that higher interfacial temperatures generally lead to rougher and more heterogeneous membrane morphologies [31]. Increasing the roughness of polymeric selective layers can have both positive and negative impacts on TFC membrane performance. For example, rougher membranes may exhibit an increased effective mass transfer area [72] and promote fouling and mineral scaling [73], while the resulting broad pore size distribution and heterogeneous selective layer thickness can impact water permeance [74] and lower water-salt selectivity [75].

The impact of membrane support layer and interlayer materials on interfacial temperature during IP extends beyond their thermal properties analyzed here. Solvent, support layer, and interlayer choice can promote or retard the partitioning and diffusion of monomers to the reaction interface, altering the IP reaction

rate and reaction exothermicity. The hydrophilicity or hydrophobicity of support layers and interlayers can also affect the extent of aqueous solution adsorption, impacting effective monomer concentrations near the reaction zone and effective layer porosity, which affects its thermal effusivity (Section 3.2). In the preceding analysis, higher monomer concentrations, more exothermic IP chemistries, and faster reactant transport or reaction rates would drive an increase in the diffusion-limited interfacial heat release constant ($q_0\sqrt{t_0}$), leading to higher interfacial temperatures.

5 Conclusions

Thin-film composite (TFC) membranes have revolutionized desalination and water treatment, dramatically increasing the energy efficiency and selectivity of reverse osmosis (RO). Currently, extensive research efforts are focused on developing TFCs for a vast array of new applications, from high-pressure RO membranes for brine volume reduction and nanofiltration (NF) membranes for critical metals extraction from brines to gas separation membranes for energy-efficient carbon capture and hydrogen production. TFC membranes comprise a thin selective layer formed by interfacial polymerization (IP) on a porous support layer. Interlayers deposited on the support layer prior to IP are also used to modulate the physical and chemical structure of the selective layer. The preceding analysis develops a transient heat conduction model to understand how the thermal properties of the aqueous and organic solvent layers, polymeric support layers, and inorganic or metallic interlayers impact interfacial temperature during the fabrication of TFC selective layers.

By combining analytical and numerical models, we examine the evolution of temperature over time during interfacial heat release in support-free (SFIP), conventional (CIP), and interlayer-modulated IP (IMIP), which are represented by two-, three-, and four-layer heat transfer systems, respectively. Using diffusion-limited interfacial heat release as an upper bound for planar heat source intensity, we demonstrate that interfacial temperature is a function of the thermal effusivity, rather than thermal conductivity or thermal diffusivity, of each fluid layer and any support layer or interlayer that is present during IP. Initially, interfacial temperature is inversely proportional to the sum of the thermal effusivities of the two materials on either side of the reaction interface—the organic fluid and the aqueous fluid (SFIP), support layer (CIP), or interlayer (IMIP). In SFIP, solvent choice has a relatively minor impact on heat transfer since the thermal effusivities of most organic solvents that are immiscible with water are relatively similar. In CIP, the introduction of a polymeric support layer leads to an increase of 20% to 60% in temperature rise at the reaction interface, compared to SFIP, depending on the polymer and its porosity. As time from the start of the IP reaction increases, heat is conducted through the porous support layer and into the aqueous fluid. This leads to a reduction in interfacial temperature over time in CIP because the thermal effusivity of water is more than double that of most polymeric support layer materials. Furthermore, our analysis demonstrates that incorporating inorganic or metallic interlayer materials with thermal effusivities substantially higher than that of water can lead to a drastic reduction ($> 90\%$) in initial interfacial temperature rise during IMIP. However, interlayer heat conduction timescales are small ($< 10^{-6}$ s), because most membrane interlayers are thin ($< 1\ \mu$m), limiting their thermal impact on the formation of the incipient selective layer.

The analysis presented in this work highlights the thermal impact of solvent and material choice on selective layer formation during TFC membrane fabrication. The upper bounds on temperature increase derived here enable the effects of elevated interfacial temperatures on membrane formation to be delineated and isolated from the myriad of other complex phenomena, from IP reaction kinetics to polymer precipitation. By understanding how support layer or interlayer thickness, porosity, and structure impact the magnitude

and duration of changes in interfacial temperature, the present analysis can inform improved composite membrane design for the vast array of emerging separations challenges. The analytical and computational models developed enable the rapid evaluation of how new membrane support and interlayer materials and structures will influence heat transfer during selective layer formation, accelerating the development of new membrane chemistries and architectures.

Author Contributions

A. Deshmukh developed the analytical model, computational framework, and conducted technical analysis. M. Elimelech and J. H. Lienhard conceived and supervised the project. All authors participated in the discussion and writing of the manuscript.

Competing Interests

The authors declare that they have no competing financial interests.

Acknowledgments

A. Deshmukh gratefully acknowledges financial support from the MIT Energy Initiative Fellowship. Figures 2-8 were created using the `matplotlib` library in Python [76] using colors from the `seaborn` library [77].

Appendix

A Laplace-Domain Temperature Field

The governing equation for heat transfer in layer i in the Laplace domain is

$$\frac{d^2U_i}{dz^2} - \frac{sU_i}{\alpha_i} = 0 \tag{A1}$$

where s is the complex Laplace domain variable and $\alpha_i = k_i/(\rho_i c_{\mathrm{P}i})$ is the thermal diffusivity of layer i. The boundary conditions in the Laplace domain for an n-layer heat transfer system, where layers 1 and n are semi-infinite, are

$$\begin{aligned} U_1(0,s) &= U_2(0,s) \\ -k_1\frac{dU_1}{dz}(0,s) + Q(s) &= -k_2\frac{dU_2}{dz}(0,s) \end{aligned} \tag{A2}$$

$$\begin{aligned} U_i(z_i,t) &= U_{i+1}(z_i,t) && \forall\ i \in 2,...,n-1 \\ -k_i\frac{dU_i}{dz}(z_i,t) &= -k_{i+1}\frac{dU_{i+1}}{dz}(z_i,t) && \forall\ i \in 2,...,n-1 \end{aligned} \tag{A3}$$

$$\begin{aligned} U_1(z\to-\infty,s) &\to 0 \\ U_n(z\to\infty,s) &\to 0 \end{aligned} \tag{A4}$$

where $Q(s) = \mathscr{L}\{q(t)\}$ is the Laplace transform of the rate of interfacial heat release. Integrating Equation A1, the Laplace-domain temperature increase (U_i) and heat flux ($-k_i(dU_i/dz)$) in layer i can be written as

$$U_i = A_i \exp\left(z\sqrt{\frac{s}{\alpha_i}}\right) + B_i \exp\left(-z\sqrt{\frac{s}{\alpha_i}}\right) \tag{A5}$$

$$-k_i\frac{dU_i}{dz} = -\kappa_i\sqrt{s}\left[A_i \exp\left(z\sqrt{\frac{s}{\alpha_i}}\right) - B_i \exp\left(-z\sqrt{\frac{s}{\alpha_i}}\right)\right] \tag{A6}$$

where A_i and B_i are integration constants for layer i, and $\kappa_i = k_i/\sqrt{\alpha_i} = \sqrt{k_i\rho_i c_{\mathrm{P}i}}$ is the thermal effusivity of layer i (units W $\mathrm{s}^{\frac{1}{2}}$ m^{-2} K^{-1}). Integration constants A_i and B_i are a function of the thermal diffusivity of each layer ($\alpha_1,...,\alpha_n$), the thermal effusivity of each layer ($\kappa_1,...,\kappa_n$), the thickness of each finite layer ($d_2,...,d_{n-1}$), the Laplace transform of the rate of interfacial heat release (Q), and the Laplace-domain variable (s). Time- and Laplace-domain solutions were derived both manually and using the `sympy` symbolic mathematics library in Python [78].

A.1 Two-Layer Heat Transfer System

For a two-layer heat transfer system (e.g., support-free interfacial polymerization) the boundary conditions are

$$\begin{aligned} U_1^{2\mathrm{L}}(0,s) &= U_2^{2\mathrm{L}}(0,s) \\ -k_1\frac{dU_1^{2\mathrm{L}}}{dz}(0,s) + Q(s) &= -k_2\frac{dU_2^{2\mathrm{L}}}{dz}(0,s) \end{aligned} \tag{A7}$$

$$U_1^{2L}(z\to-\infty,s)\to 0$$
$$U_2^{2L}(z\to\infty,s)\to 0 \tag{A8}$$

where $Q(s)=\mathscr{L}\{q(t)\}$ is the Laplace transform of the planar heat flux at $z=0$. The boundary conditions at $z=0$, $z\to\infty$, and $z\to-\infty$ give

$$A_1^{2L}+B_1^{2L}=A_2^{2L}+B_2^{2L} \tag{A9}$$
$$\kappa_1\left(A_1^{2L}-B_1^{2L}\right)-\kappa_2\left(A_2^{2L}-B_2^{2L}\right)=\frac{Q}{\sqrt{s}} \tag{A10}$$
$$B_1^{2L}=0 \tag{A11}$$
$$A_2^{2L}=0 \tag{A12}$$

where $\kappa_i=k_i/\sqrt{\alpha_i}=\sqrt{k_i\rho_i c_{Pi}}$ is the thermal effusivity of layer i, which has units W $s^{\frac{1}{2}}$ m^{-2} K^{-1}. Boundary condition equations can be solved for unknown integration constants (A_1^{2L} and B_2^{2L}) giving

$$A_1^{2L}=\frac{Q}{(\kappa_1+\kappa_2)\sqrt{s}} \tag{A13}$$
$$B_2^{2L}=\frac{Q}{(\kappa_1+\kappa_2)\sqrt{s}} \tag{A14}$$

The temperature profiles in layers 1 and 2 as a function of distance from the reaction interface (z), the complex Laplace domain variable (s), and the Laplace transform of the rate of interfacial heat release (Q) are given by

$$U_1^{2L}(z,s)=\frac{Q}{(\kappa_1+\kappa_2)\sqrt{s}}\exp\left(z\sqrt{\frac{s}{\alpha_1}}\right) \tag{A15}$$
$$U_2^{2L}(z,s)=\frac{Q}{(\kappa_1+\kappa_2)\sqrt{s}}\exp\left(-z\sqrt{\frac{s}{\alpha_2}}\right) \tag{A16}$$

The temperature at the reaction interface is given by:

$$U_{\text{int}}^{2L}(s)=\frac{Q}{\sqrt{s}(\kappa_1+\kappa_2)} \tag{A17}$$

For diffusion-limited interfacial heat release ($Q^{\text{dl}}=q_0\sqrt{\pi t_0/s}$) the interfacial temperature rise is

$$\bar{U}_{\text{int}}^{2L,\text{dl}}(s)=\frac{\sqrt{\pi}}{s(\kappa_1+\kappa_2)} \tag{A18}$$

A.2 Three-Layer Heat Transfer System

For a three-layer heat transfer system (e.g., conventional interfacial polymerization) the boundary conditions are

$$U_1^{3L}(0,s)=U_2^{3L}(0,s)$$
$$-k_1\frac{dU_1^{3L}}{dz}(0,s)+Q(s)=-k_2\frac{dU_2^{3L}}{dz}(0,s) \tag{A19}$$

$$U_2^{3L}(d_2,s) = U_3^{3L}(d_2,s)$$
$$-k_2\frac{dU_2^{3L}}{dz}(d_2,s) = -k_3\frac{dU_3^{3L}}{dz}(d_2,s) \tag{A20}$$
$$U_1^{3L}(z\to-\infty,s)\to 0$$
$$U_3^{3L}(z\to\infty,s)\to 0 \tag{A21}$$

where $Q(s)=\mathscr{L}\{q(t)\}$ is the Laplace transform of the planar heat flux at $z=0$. The boundary conditions at $z=0$, $z=d_2$, $z\to\infty$, and $z\to-\infty$ give

$$A_1^{3L}+B_1^{3L} = A_2^{3L}+B_2^{3L} \tag{A22}$$
$$\kappa_1\left(A_1^{3L}-B_1^{3L}\right)-\kappa_2\left(A_2^{3L}-B_2^{3L}\right) = \frac{Q}{\sqrt{s}} \tag{A23}$$
$$A_2^{3L}\exp\left(d_2\sqrt{\frac{s}{\alpha_2}}\right)+B_2^{3L}\exp\left(-d_2\sqrt{\frac{s}{\alpha_2}}\right) = A_3^{3L}\exp\left(d_2\sqrt{\frac{s}{\alpha_3}}\right)+B_3^{3L}\exp\left(-d_2\sqrt{\frac{s}{\alpha_3}}\right) \tag{A24}$$
$$\kappa_2\left[A_2^{3L}\exp\left(d_2\sqrt{\frac{s}{\alpha_2}}\right)-B_2^{3L}\exp\left(-d_2\sqrt{\frac{s}{\alpha_2}}\right)\right] = \kappa_3\left[A_3^{3L}\exp\left(d_2\sqrt{\frac{s}{\alpha_3}}\right)-B_3^{3L}\exp\left(-d_2\sqrt{\frac{s}{\alpha_3}}\right)\right] \tag{A25}$$
$$B_1^{3L} = 0 \tag{A26}$$
$$A_3^{3L} = 0 \tag{A27}$$

Boundary condition equations can be solved for unknown integration constants (A_1^{3L}, A_2^{3L}, B_2^{3L}, and B_3^{3L}) giving

$$A_1^{3L} = \frac{Q}{\sqrt{s}}\left[\frac{\kappa_2+\kappa_3+(\kappa_2-\kappa_3)\exp\left(-2d_2\sqrt{\frac{s}{\alpha_2}}\right)}{(\kappa_1+\kappa_2)(\kappa_2+\kappa_3)+(\kappa_1-\kappa_2)(\kappa_2-\kappa_3)\exp\left(-2d_2\sqrt{\frac{s}{\alpha_2}}\right)}\right] \tag{A28}$$
$$A_2^{3L} = \frac{Q}{\sqrt{s}}\left[\frac{(\kappa_2-\kappa_3)\exp\left(-2d_2\sqrt{\frac{s}{\alpha_2}}\right)}{(\kappa_1+\kappa_2)(\kappa_2+\kappa_3)+(\kappa_1-\kappa_2)(\kappa_2-\kappa_3)\exp\left(-2d_2\sqrt{\frac{s}{\alpha_2}}\right)}\right] \tag{A29}$$
$$B_2^{3L} = \frac{Q}{\sqrt{s}}\left[\frac{\kappa_2+\kappa_3}{(\kappa_1+\kappa_2)(\kappa_2+\kappa_3)+(\kappa_1-\kappa_2)(\kappa_2-\kappa_3)\exp\left(-2d_2\sqrt{\frac{s}{\alpha_2}}\right)}\right] \tag{A30}$$
$$B_3^{3L} = \frac{Q}{\sqrt{s}}\left\{\frac{2\kappa_2\exp\left[-d_2\left(\frac{1}{\sqrt{\alpha_2}}-\frac{1}{\sqrt{\alpha_3}}\right)\sqrt{s}\right]}{(\kappa_1+\kappa_2)(\kappa_2+\kappa_3)+(\kappa_1-\kappa_2)(\kappa_2-\kappa_3)\exp\left(-2d_2\sqrt{\frac{s}{\alpha_2}}\right)}\right\} \tag{A31}$$

Integration constants (A_1^{3L}, A_2^{3L}, B_2^{3L}, and B_3^{3L}) can also be expressed in of the characteristic timescale for heat conduction ($\tau_i = d_i^2/\alpha_i$) though finite layer i, giving

$$A_1^{3L} = \frac{Q}{\sqrt{s}}\left[\frac{\kappa_2+\kappa_3+(\kappa_2-\kappa_3)\exp(-2\sqrt{\tau_2 s})}{(\kappa_1+\kappa_2)(\kappa_2+\kappa_3)+(\kappa_1-\kappa_2)(\kappa_2-\kappa_3)\exp(-2\sqrt{\tau_2 s})}\right] \tag{A32}$$

$$A_2^{3L} = \frac{Q}{\sqrt{s}}\left[\frac{(\kappa_2-\kappa_3)\exp(-2\sqrt{\tau_2 s})}{(\kappa_1+\kappa_2)(\kappa_2+\kappa_3)+(\kappa_1-\kappa_2)(\kappa_2-\kappa_3)\exp(-2\sqrt{\tau_2 s})}\right] \tag{A33}$$

$$B_2^{3L} = \frac{Q}{\sqrt{s}}\left[\frac{\kappa_2+\kappa_3}{(\kappa_1+\kappa_2)(\kappa_2+\kappa_3)+(\kappa_1-\kappa_2)(\kappa_2-\kappa_3)\exp(-2\sqrt{\tau_2 s})}\right] \tag{A34}$$

$$B_3^{3L} = \frac{Q}{\sqrt{s}}\left\{\frac{2\kappa_2\exp\left[-\left(1-\sqrt{\frac{\alpha_2}{\alpha_3}}\right)\sqrt{\tau_2 s}\right]}{(\kappa_1+\kappa_2)(\kappa_2+\kappa_3)+(\kappa_1-\kappa_2)(\kappa_2-\kappa_3)\exp(-2\sqrt{\tau_2 s})}\right\} \tag{A35}$$

Laplace transform of temperature fields in layers 1, 2, and 3 are given by

$$U_1^{3L}(z,s) = \frac{Q}{\sqrt{s}X^{3L,den}}[\kappa_2+\kappa_3+(\kappa_2-\kappa_3)\exp(-2\sqrt{\tau_2 s})]\exp\left(z\sqrt{\frac{s}{\alpha_1}}\right) \tag{A36}$$

$$U_2^{3L}(z,s) = \frac{Q}{\sqrt{s}X^{3L,den}}\left[(\kappa_2-\kappa_3)\exp\left(-2\sqrt{\tau_2 s}+z\sqrt{\frac{s}{\alpha_2}}\right)+(\kappa_2+\kappa_3)\exp\left(-z\sqrt{\frac{s}{\alpha_2}}\right)\right] \tag{A37}$$

$$U_3^{3L}(z,s) = \frac{Q}{\sqrt{s}X^{3L,den}}\left\{2\kappa_2\exp\left[-\left(1-\sqrt{\frac{\alpha_2}{\alpha_3}}\right)\sqrt{\tau_2 s}-z\sqrt{\frac{s}{\alpha_3}}\right]\right\} \tag{A38}$$

$$X^{3L,den} = (\kappa_1+\kappa_2)(\kappa_2+\kappa_3)+(\kappa_1-\kappa_2)(\kappa_2-\kappa_3)\exp(-2\sqrt{\tau_2 s}) \tag{A39}$$

where $X^{3L,den}$ is a common denominator for a three-layer heat transfer system. The temperature at the reaction interface ($z=0$) is given by

$$U_{int}^{3L}(s) = \frac{Q}{\sqrt{s}}\left[\frac{\kappa_2+\kappa_3+(\kappa_2-\kappa_3)\exp\left(-2d_2\sqrt{\frac{s}{\alpha_2}}\right)}{(\kappa_1+\kappa_2)(\kappa_2+\kappa_3)+(\kappa_1-\kappa_2)(\kappa_2-\kappa_3)\exp\left(-2d_2\sqrt{\frac{s}{\alpha_2}}\right)}\right] \tag{A40}$$

$$U_{int}^{3L}(s) = \frac{Q}{\sqrt{s}(\kappa_1+\kappa_2)}\left[\frac{1+\gamma_{2,3}\exp(-2\sqrt{\tau_2 s})}{1+\gamma_{1,2}\gamma_{2,3}\exp(-2\sqrt{\tau_2 s})}\right] \tag{A41}$$

where $\gamma_{i,j} = (\kappa_i-\kappa_j)/(\kappa_i+\kappa_j)$, noting that $|\gamma_{i,j}| < 1 \;\forall\; i,j \in 1,...,n$ given that $\kappa_i > 0 \;\forall\; i \in 1,...,n$. For diffusion-limited interfacial heat release ($Q^{dl} = q_0\sqrt{\pi t_0/s}$) the interfacial temperature rise is

$$\bar{U}_{int}^{3L,dl}(s) = \frac{\sqrt{\pi}}{s(\kappa_1+\kappa_2)}\left[\frac{1+\gamma_{2,3}\exp(-2\sqrt{\tau_2 s})}{1+\gamma_{1,2}\gamma_{2,3}\exp(-2\sqrt{\tau_2 s})}\right] \tag{A42}$$

Initial ($t \to 0^+$) and final ($t \to \infty$) interfacial temperatures can be calculated by applying the initial and final value theorems for Laplace transforms to the expression for $\bar{U}_{int}^{3L,dl}$ (Equation A42) giving

$$\bar{u}_{int,t\to 0^+}^{3L,dl} = \lim_{s\to\infty} s\bar{U}_{int}^{3L,dl}(s) = \frac{\sqrt{\pi}}{\kappa_1+\kappa_2} \tag{A43}$$

$$\bar{u}_{int,t\to\infty}^{3L,dl} = \lim_{s\to 0} s\bar{U}_{int}^{3L,dl}(s) = \frac{\sqrt{\pi}}{\kappa_1+\kappa_2}\left(\frac{1+\gamma_{2,3}}{1+\gamma_{1,2}\gamma_{2,3}}\right) = \frac{\sqrt{\pi}}{\kappa_1+\kappa_3} \tag{A44}$$

noting that $\tau_2 > 0$ and that all poles of $sU_{int}^{3L,dl}$ are in the left complex half-plane.

A.3 Normalized Interfacial Temperature Change in a Three-Layer Heat Transfer System

Normalizing the interfacial temperature for a three-layer heat transfer system with diffusion-limited heat release relative to the initial and final limiting temperatures ($\theta_{\text{int}}^{\text{3L,dl}}$) gives

$$\theta_{\text{int}}^{\text{3L,dl}} = \frac{u_{\text{int}}^{\text{3L,dl}} - u_{\text{int},t\to\infty}^{\text{3L,dl}}}{u_{\text{int},t\to 0^+}^{\text{3L,dl}} - u_{\text{int},t\to\infty}^{\text{3L,dl}}} \tag{A45}$$

$$u_{\text{int},t\to 0^+}^{\text{3L,dl}} - u_{\text{int},t\to\infty}^{\text{3L,dl}} = \frac{1}{\kappa_1+\kappa_2} - \frac{1}{\kappa_1+\kappa_3} \tag{A46}$$

For diffusion-limited interfacial heat release $u_{\text{int,t}\to 0^+}^{\text{3L,dl}}$ and $u_{\text{int,t}\to\infty}^{\text{3L,dl}}$ are constants, independent of time. Consequently, the Laplace transform of the normalized interfacial temperature with diffusion-limited interfacial heat release in a three-layer heat transfer system ($\Theta_{\text{int}}^{\text{3L,dl}}$) can be expressed as

$$\Theta_{\text{int}}^{\text{3L,dl}}(s) = \left[\mathscr{L}\left\{u_{\text{int}}^{\text{3L,dl}}\right\} - \mathscr{L}\left\{u_{\text{int},t\to\infty}^{\text{3L,dl}}\right\}\right]\left(\frac{1}{\kappa_1+\kappa_2} - \frac{1}{\kappa_1+\kappa_3}\right)^{-1} \tag{A47}$$

$$\Theta_{\text{int}}^{\text{3L,dl}}(s) = \left[\mathscr{L}\left\{u_{\text{int}}^{\text{3L,dl}}\right\} - \frac{1}{s(\kappa_1+\kappa_3)}\right]\left(\frac{1}{\kappa_1+\kappa_2} - \frac{1}{\kappa_1+\kappa_3}\right)^{-1} \tag{A48}$$

Substituting the expression for $U_{\text{int}}^{\text{3L,dl}} = \mathscr{L}\{u_{\text{int}}^{\text{3L,dl}}\}$ (Equation 18) gives

$$\Theta_{\text{int}}^{\text{3L,dl}}(s) = \frac{1}{s}\left[\frac{1+\gamma_{2,3}\exp(-2\sqrt{\tau_2 s})}{(\kappa_1+\kappa_2)[1+\gamma_{1,2}\gamma_{2,3}\exp(-2\sqrt{\tau_2 s})]} - \frac{1}{\kappa_1+\kappa_3}\right]\left(\frac{1}{\kappa_1+\kappa_2} - \frac{1}{\kappa_1+\kappa_3}\right)^{-1} \tag{A49}$$

$$\Theta_{\text{int}}^{\text{3L,dl}}(s) = \frac{1}{s}\left\{\frac{1}{\kappa_1+\kappa_3} - \frac{1+\gamma_{2,3}\exp(-2\sqrt{\tau_2 s})}{(\kappa_1+\kappa_2)[1+\gamma_{1,2}\gamma_{2,3}\exp(-2\sqrt{\tau_2 s})]}\right\}\left[\frac{(\kappa_1+\kappa_2)(\kappa_1+\kappa_3)}{\kappa_2-\kappa_3}\right] \tag{A50}$$

$$\Theta_{\text{int}}^{\text{3L,dl}}(s) = \frac{1}{s}\left\{\frac{\kappa_1+\kappa_2}{\kappa_2-\kappa_3} - \frac{\left(\frac{\kappa_1+\kappa_3}{\kappa_2-\kappa_3}\right)[1+\gamma_{2,3}\exp(-2\sqrt{\tau_2 s})]}{1+\gamma_{1,2}\gamma_{2,3}\exp(-2\sqrt{\tau_2 s})}\right\} \tag{A51}$$

$$\Theta_{\text{int}}^{\text{3L,dl}}(s) = \frac{1}{s}\left\{\frac{1+\left[\left(\frac{\kappa_1+\kappa_2}{\kappa_2-\kappa_3}\right)\gamma_{1,2}\gamma_{2,3} - \frac{\kappa_1+\kappa_3}{\kappa_2+\kappa_3}\right]\exp(-2\sqrt{\tau_2 s})}{1+\gamma_{1,2}\gamma_{2,3}\exp(-2\sqrt{\tau_2 s})}\right\} \tag{A52}$$

$$\Theta_{\text{int}}^{\text{3L,dl}}(s) = \frac{1}{s}\left[\frac{1-\exp(-2\sqrt{\tau_2 s})}{1+\gamma_{1,2}\gamma_{2,3}\exp(-2\sqrt{\tau_2 s})}\right] \tag{A53}$$

$$\Theta_{\text{int}}^{\text{3L,dl}}(s) = \frac{1}{\gamma_{1,2}\gamma_{2,3}s}\left[\frac{1+\gamma_{1,2}\gamma_{2,3}}{1+\gamma_{1,2}\gamma_{2,3}\exp(-2\sqrt{\tau_2 s})} - 1\right] \tag{A54}$$

where $\gamma_{i,j} = (\kappa_i - \kappa_j)/(\kappa_i + \kappa_j)$, noting that $|\gamma_{i,j}| < 1 \;\forall\; i, j \in 1, ..., n$ given that $\kappa_i > 0 \;\forall\; i \in 1, ..., n$.

A.4 Four-Layer Heat Transfer System

For a four-layer heat transfer system (e.g., interlayer-modulated interfacial polymerization) the boundary conditions are

$$U_1^{\text{4L}}(0,s) = U_2^{\text{4L}}(0,s)$$

$$-k_1\frac{dU_1^{4L}}{dz}(0,s)+Q(s)=-k_2\frac{dU_2^{4L}}{dz}(0,s) \tag{A55}$$

$$U_2^{4L}(d_2,s)=U_3^{4L}(d_2,s)$$

$$-k_2\frac{dU_2^{4L}}{dz}(d_2,s)=-k_3\frac{dU_3^{4L}}{dz}(d_2,s) \tag{A56}$$

$$U_3^{4L}(d_2+d_3,s)=U_4^{4L}(d_2+d_3,s)$$

$$-k_3\frac{dU_3^{4L}}{dz}(d_2+d_3,s)=-k_4\frac{dU_4^{4L}}{dz}(d_2+d_3,s) \tag{A57}$$

$$U_1^{4L}(z\to-\infty,s)\to 0$$

$$U_4^{4L}(z\to\infty,s)\to 0 \tag{A58}$$

where $Q(s)=\mathscr{L}\{q(t)\}$ is the Laplace transform of the planar heat flux at $z=0$. The boundary conditions at $z=0$, $z=d_2$, $z=d_2+d_3$, $z\to\infty$, and $z\to-\infty$ give

$$A_1^{4L}+B_1^{4L}=A_2^{4L}+B_2^{4L} \tag{A59}$$

$$\kappa_1\left(A_1^{4L}-B_1^{4L}\right)-\kappa_2\left(A_2^{4L}-B_2^{4L}\right)=\frac{Q}{\sqrt{s}} \tag{A60}$$

$$A_2^{4L}\exp\left(d_2\sqrt{\frac{s}{\alpha_2}}\right)+B_2^{4L}\exp\left(-d_2\sqrt{\frac{s}{\alpha_2}}\right)=$$

$$A_3^{4L}\exp\left(d_2\sqrt{\frac{s}{\alpha_3}}\right)+B_3^{4L}\exp\left(-d_2\sqrt{\frac{s}{\alpha_3}}\right) \tag{A61}$$

$$\kappa_2\left[A_2^{4L}\exp\left(d_2\sqrt{\frac{s}{\alpha_2}}\right)-B_2^{4L}\exp\left(-d_2\sqrt{\frac{s}{\alpha_2}}\right)\right]=$$

$$\kappa_3\left[A_3^{4L}\exp\left(d_2\sqrt{\frac{s}{\alpha_3}}\right)-B_3^{4L}\exp\left(-d_2\sqrt{\frac{s}{\alpha_3}}\right)\right] \tag{A62}$$

$$A_3^{4L}\exp\left[(d_2+d_3)\sqrt{\frac{s}{\alpha_3}}\right]+B_3^{4L}\exp\left[-(d_2+d_3)\sqrt{\frac{s}{\alpha_3}}\right]=$$

$$A_4^{4L}\exp\left[(d_2+d_3)\sqrt{\frac{s}{\alpha_4}}\right]+B_4^{4L}\exp\left[-(d_2+d_3)\sqrt{\frac{s}{\alpha_4}}\right] \tag{A63}$$

$$\kappa_3\left\{A_3^{4L}\exp\left[(d_2+d_3)\sqrt{\frac{s}{\alpha_3}}\right]-B_3^{4L}\exp\left[-(d_2+d_3)\sqrt{\frac{s}{\alpha_3}}\right]\right\}=$$

$$\kappa_4\left\{A_4^{4L}\exp\left[(d_2+d_3)\sqrt{\frac{s}{\alpha_4}}\right]-B_4^{4L}\exp\left[-(d_2+d_3)\sqrt{\frac{s}{\alpha_4}}\right]\right\} \tag{A64}$$

$$B_1^{4L}=0 \tag{A65}$$

$$A_4^{4L}=0 \tag{A66}$$

Boundary condition equations can be solved for unknown integration constants (A_1^{4L}, A_2^{4L}, B_2^{4L}, A_3^{4L}, B_3^{4L}, and B_4^{4L}). For convenience, we define $X_i^{4L}=(Q/\sqrt{s})(X_i^{4L,num}/X^{4L,den})$, where $X_i^{4L,num}$ is the numerator for constant X_i^{4L} and $X^{4L,den}$ is a common denominator for all the constants in a four-layer heat transfer system, giving

$$A_1^{4L,num}=(\kappa_2+\kappa_3)(\kappa_3+\kappa_4)+(\kappa_2-\kappa_3)(\kappa_3+\kappa_4)\exp\left(-2d_2\sqrt{\frac{s}{\alpha_2}}\right)$$

$$+(\kappa_2-\kappa_3)(\kappa_3-\kappa_4)\exp\left(-2d_3\sqrt{\frac{s}{\alpha_3}}\right)+(\kappa_2+\kappa_3)(\kappa_3-\kappa_4)\exp\left[-2\left(\frac{d_2}{\sqrt{\alpha_2}}+\frac{d_3}{\sqrt{\alpha_3}}\right)\sqrt{s}\right] \tag{A67}$$

$$A_2^{4L,num}=(\kappa_2-\kappa_3)(\kappa_3+\kappa_4)\exp\left(-2d_2\sqrt{\frac{s}{\alpha_2}}\right)+(\kappa_2+\kappa_3)(\kappa_3-\kappa_4)\exp\left[-2\left(\frac{d_2}{\sqrt{\alpha_2}}+\frac{d_3}{\sqrt{\alpha_3}}\right)\sqrt{s}\right] \tag{A68}$$

$$B_2^{4L,num}=(\kappa_2+\kappa_3)(\kappa_3+\kappa_4)+(\kappa_2-\kappa_3)(\kappa_3-\kappa_4)\exp\left(-2d_3\sqrt{\frac{s}{\alpha_3}}\right) \tag{A69}$$

$$A_3^{4L,num}=2\kappa_2(\kappa_3-\kappa_4)\exp\left[-\left(\frac{d_2}{\sqrt{\alpha_2}}+\frac{d_2+2d_3}{\sqrt{\alpha_3}}\right)\sqrt{s}\right] \tag{A70}$$

$$B_3^{4L,num}=2\kappa_2(\kappa_3-\kappa_4)\exp\left[-\left(\frac{d_2}{\sqrt{\alpha_2}}-\frac{d_2}{\sqrt{\alpha_3}}\right)\sqrt{s}\right] \tag{A71}$$

$$B_4^{4L,num}=4\kappa_2\kappa_3\exp\left[\left(-\frac{d_2}{\sqrt{\alpha_2}}-\frac{d_3}{\sqrt{\alpha_3}}+\frac{d_2+d_3}{\sqrt{\alpha_4}}\right)\sqrt{s}\right] \tag{A72}$$

$$\begin{aligned}X^{4L,den}=&(\kappa_1+\kappa_2)(\kappa_2+\kappa_3)(\kappa_3+\kappa_4)+(\kappa_1-\kappa_2)(\kappa_2-\kappa_3)(\kappa_3+\kappa_4)\exp\left(-2d_2\sqrt{\frac{s}{\alpha_2}}\right)\\&+(\kappa_1+\kappa_2)(\kappa_2-\kappa_3)(\kappa_3-\kappa_4)\exp\left(-2d_3\sqrt{\frac{s}{\alpha_3}}\right)\\&+(\kappa_1-\kappa_2)(\kappa_2+\kappa_3)(\kappa_3-\kappa_4)\exp\left[-2\left(\frac{d_2}{\sqrt{\alpha_2}}+\frac{d_3}{\sqrt{\alpha_3}}\right)\sqrt{s}\right]\end{aligned} \tag{A73}$$

The numerators and denominator of integration constants (A_1^{4L}, A_2^{4L}, B_2^{4L}, A_3^{4L}, B_3^{4L}, and B_4^{4L}) can also be expressed in of the characteristic timescale for heat conduction ($\tau_i=d_i^2/\alpha_i$) though finite layer i, giving

$$\begin{aligned}A_1^{4L,num}=&(\kappa_2+\kappa_3)(\kappa_3+\kappa_4)+(\kappa_2-\kappa_3)(\kappa_3+\kappa_4)\exp(-2\sqrt{\tau_2 s})\\&+(\kappa_2-\kappa_3)(\kappa_3-\kappa_4)\exp(-2\sqrt{\tau_3 s})+(\kappa_2+\kappa_3)(\kappa_3-\kappa_4)\exp[-2(\sqrt{\tau_2 s}+\sqrt{\tau_3 s})]\end{aligned} \tag{A74}$$

$$A_2^{4L,num}=(\kappa_2-\kappa_3)(\kappa_3+\kappa_4)\exp(-2\sqrt{\tau_2 s})+(\kappa_2+\kappa_3)(\kappa_3-\kappa_4)\exp[-2(\sqrt{\tau_2 s}+\sqrt{\tau_3 s})] \tag{A75}$$

$$B_2^{4L,num}=(\kappa_2+\kappa_3)(\kappa_3+\kappa_4)+(\kappa_2-\kappa_3)(\kappa_3-\kappa_4)\exp(-2\sqrt{\tau_3 s}) \tag{A76}$$

$$A_3^{4L,num}=2\kappa_2(\kappa_3-\kappa_4)\exp\left[-\left(1+\sqrt{\frac{\alpha_2}{\alpha_3}}\right)\sqrt{\tau_2 s}-2\sqrt{\tau_3 s}\right] \tag{A77}$$

$$B_3^{4L,num}=2\kappa_2(\kappa_3-\kappa_4)\exp\left[-\left(1-\sqrt{\frac{\alpha_2}{\alpha_3}}\right)\sqrt{\tau_2 s}\right] \tag{A78}$$

$$B_4^{4L,num}=4\kappa_2\kappa_3\exp\left[-\left(1-\sqrt{\frac{\alpha_2}{\alpha_4}}\right)\sqrt{\tau_2 s}-\left(1-\sqrt{\frac{\alpha_3}{\alpha_4}}\right)\sqrt{\tau_3 s}\right] \tag{A79}$$

$$\begin{aligned}X^{4L,den}=&(\kappa_1+\kappa_2)(\kappa_2+\kappa_3)(\kappa_3+\kappa_4)+(\kappa_1-\kappa_2)(\kappa_2-\kappa_3)(\kappa_3+\kappa_4)\exp(-2\sqrt{\tau_2 s})\\&+(\kappa_1+\kappa_2)(\kappa_2-\kappa_3)(\kappa_3-\kappa_4)\exp(-2\sqrt{\tau_3 s})\\&+(\kappa_1-\kappa_2)(\kappa_2+\kappa_3)(\kappa_3-\kappa_4)\exp[-2(\sqrt{\tau_2 s}+\sqrt{\tau_3 s})]\end{aligned} \tag{A80}$$

The temperature at the reaction interface is

$$U_{int}^{4L}(s)=\frac{Q}{\sqrt{s}}\left(\frac{A_1^{4L,num}}{X^{4L,den}}\right) \tag{A81}$$

$$U_{\text{int}}^{\text{4L}}(s) = \frac{Q}{\sqrt{s}(\kappa_1+\kappa_2)}\left\{\frac{1+\gamma_{2,3}\exp(-2\sqrt{\tau_2 s})+\gamma_{2,3}\gamma_{3,4}\exp(-2\sqrt{\tau_3 s})+\gamma_{3,4}\exp[-2(\sqrt{\tau_2 s}+\sqrt{\tau_3 s})]}{1+\gamma_{1,2}\gamma_{2,3}\exp(-2\sqrt{\tau_2 s})+\gamma_{2,3}\gamma_{3,4}\exp(-2\sqrt{\tau_3 s})+\gamma_{1,2}\gamma_{3,4}\exp[-2(\sqrt{\tau_2 s}+\sqrt{\tau_3 s})]}\right\} \tag{A82}$$

where $\gamma_{i,j} = (\kappa_i - \kappa_j)/(\kappa_i + \kappa_j)$, noting that $|\gamma_{i,j}| < 1 \;\forall\; i, j \in 1, ..., n$ given that $\kappa_i > 0 \;\forall\; i \in 1, ..., n$. For diffusion-limited interfacial heat release ($Q^{\text{dl}} = q_0\sqrt{\pi t_0/s}$) the interfacial temperature rise is

$$\bar{U}_{\text{int}}^{\text{4L,dl}}(s) = \frac{\sqrt{\pi}}{s(\kappa_1+\kappa_2)}\left\{\frac{1+\gamma_{2,3}\exp(-2\sqrt{\tau_2 s})+\gamma_{2,3}\gamma_{3,4}\exp(-2\sqrt{\tau_3 s})+\gamma_{3,4}\exp[-2(\sqrt{\tau_2 s}+\sqrt{\tau_3 s})]}{1+\gamma_{1,2}\gamma_{2,3}\exp(-2\sqrt{\tau_2 s})+\gamma_{2,3}\gamma_{3,4}\exp(-2\sqrt{\tau_3 s})+\gamma_{1,2}\gamma_{3,4}\exp[-2(\sqrt{\tau_2 s}+\sqrt{\tau_3 s})]}\right\} \tag{A83}$$

Initial ($t \to 0^+$) and final ($t \to \infty$) interfacial temperatures can be calculated by applying the initial and final value theorems for Laplace transforms to the expression for $\bar{U}_{\text{int}}^{\text{4L,dl}}$ (Equation A83) giving

$$\bar{u}_{\text{int},t\to 0^+}^{\text{4L,dl}} = \lim_{s\to\infty} s\bar{U}_{\text{int}}^{\text{4L,dl}}(s) = \frac{\sqrt{\pi}}{\kappa_1+\kappa_2} \tag{A84}$$

$$\bar{u}_{\text{int},t\to\infty}^{\text{4L,dl}} = \lim_{s\to 0} s\bar{U}_{\text{int}}^{\text{4L,dl}}(s) = \frac{\sqrt{\pi}}{\kappa_1+\kappa_2}\left(\frac{1+\gamma_{2,3}+\gamma_{2,3}\gamma_{3,4}+\gamma_{3,4}}{1+\gamma_{1,2}\gamma_{2,3}+\gamma_{2,3}\gamma_{3,4}+\gamma_{1,2}\gamma_{3,4}}\right) = \frac{\sqrt{\pi}}{\kappa_1+\kappa_4} \tag{A85}$$

noting that $\tau_2 > 0$, $\tau_3 > 0$, and that all poles of $s\bar{U}_{\text{int}}^{\text{4L,dl}}$ are in the left complex half-plane. In a four-layer heat transfer system, an intermediate time ($\tau_2 \ll t \ll \tau_3$) limit for interfacial temperature can be evaluated, provided that the characteristic timescale for heat conduction through finite layer 2 is significantly smaller than that of finite layer 3 ($\tau_2 \ll \tau_3$). Using the time-scaling property of Laplace transforms where $\mathscr{L}\{f(at)\} = (1/a)F(s/a)$ for $\mathscr{L}\{f(t)\} = F(s)$ along with simultaneous final ($t/\tau_2 \to \infty$) and initial ($t/\tau_3 \to 0^+$) time limits gives

$$\bar{u}_{\text{int},\tau_2\ll t\ll\tau_3}^{\text{4L,dl}} = \lim_{\substack{t/\tau_2\to\infty \\ t/\tau_3\to 0^+}} \bar{u}_{\text{int}}^{\text{4L,dl}}(t) = \lim_{\substack{\tau_2 s\to 0 \\ \tau_3 s\to\infty}} s\bar{U}_{\text{int}}^{\text{4L,dl}}(s) = \frac{\sqrt{\pi}}{\kappa_1+\kappa_2}\left(\frac{1+\gamma_{2,3}}{1+\gamma_{1,2}\gamma_{2,3}}\right) = \frac{\sqrt{\pi}}{\kappa_1+\kappa_3} \tag{A86}$$

B Time-Domain Interfacial Temperature

B.1 Two-Layer Heat Transfer System with Diffusion-Limited Interfacial Heat Release

For diffusion-limited interfacial heat release into a two-layer heat transfer system interfacial temperature is constant and given by

$$\bar{U}_{\text{int}}^{\text{2L,dl}}(s) = \frac{\sqrt{\pi}}{s(\kappa_1+\kappa_2)} \tag{B87}$$

$$\bar{u}_{\text{int}}^{\text{2L,dl}}(t) = \frac{\sqrt{\pi}}{\kappa_1+\kappa_2} \tag{B88}$$

B.2 Three-Layer Heat Transfer System with Diffusion-Limited Interfacial Heat Release

The Laplace-domain expression for interfacial temperature with diffusion-limited interfacial heat release in a three-layer heat transfer system ($\bar{U}_{\text{int}}^{\text{3L,dl}}$, Equation 18) can be expanded in series by applying the binomial

theorem to the denominator [79]

$$\bar{U}_{\text{int}}^{\text{3L,dl}}(s) = \frac{\sqrt{\pi}}{s(\kappa_1+\kappa_2)}\left[\frac{1+\gamma_{2,3}\exp(-2\sqrt{\tau_2 s})}{1+\gamma_{1,2}\gamma_{2,3}\exp(-2\sqrt{\tau_2 s})}\right] \tag{B89}$$

$$\bar{U}_{\text{int}}^{\text{3L,dl}}(s) = \frac{\sqrt{\pi}}{s(\kappa_1+\kappa_2)}[1+\gamma_{2,3}\exp(-2\sqrt{\tau_2 s})]\sum_{j=0}^{\infty}\left[(-\gamma_{1,2}\gamma_{2,3})^j\exp(-2j\sqrt{\tau_2 s})\right] \tag{B90}$$

noting that $|\gamma_{1,2}\gamma_{2,3}| < 1$ given that $\kappa_i > 0\ \forall\ i \in 1,...,n$. Rearranging gives

$$\bar{U}_{\text{int}}^{\text{3L,dl}}(s) = \frac{\sqrt{\pi}}{s(\kappa_1+\kappa_2)}\left\{\sum_{j=0}^{\infty}\left[(-\gamma_{1,2}\gamma_{2,3})^j\exp(-2j\sqrt{\tau_2 s})\right] + \gamma_{2,3}\sum_{j=0}^{\infty}\left[(-\gamma_{1,2}\gamma_{2,3})^j\exp(-2(j+1)\sqrt{\tau_2 s})\right]\right\} \tag{B91}$$

$$\bar{U}_{\text{int}}^{\text{3L,dl}}(s) = \frac{\sqrt{\pi}}{s(\kappa_1+\kappa_2)}\left\{\sum_{j=0}^{\infty}\left[(-\gamma_{1,2}\gamma_{2,3})^j\exp(-2j\sqrt{\tau_2 s})\right] - \frac{1}{\gamma_{1,2}}\sum_{j=1}^{\infty}\left[(-\gamma_{1,2}\gamma_{2,3})^j\exp(-2j\sqrt{\tau_2 s})\right]\right\} \tag{B92}$$

$$\bar{U}_{\text{int}}^{\text{3L,dl}}(s) = \frac{\sqrt{\pi}}{s(\kappa_1+\kappa_2)}\left\{1+\left[1-\frac{1}{\gamma_{1,2}}\right]\sum_{j=1}^{\infty}\left[(-\gamma_{1,2}\gamma_{2,3})^j\exp(-2j\sqrt{\tau_2 s})\right]\right\} \tag{B93}$$

$$\bar{U}_{\text{int}}^{\text{3L,dl}}(s) = \frac{\sqrt{\pi}}{\kappa_1+\kappa_2}\left\{\frac{1}{s} - \frac{2\kappa_2}{\kappa_1-\kappa_2}\sum_{j=1}^{\infty}\left[\frac{(-\gamma_{1,2}\gamma_{2,3})^j\exp(-2j\sqrt{\tau_2 s})}{s}\right]\right\} \tag{B94}$$

Using Bateman 1954, Section 5.6, Number 3 [80], the Laplace-domain series expansion for $\bar{U}_{\text{int}}^{\text{3L,dl}}$ can be inverted to give a time-domain series expansion for $\bar{u}_{\text{int}}^{\text{3L,dl}}$

$$\bar{u}_{\text{int}}^{\text{3L,dl}}(t) = \frac{\sqrt{\pi}}{\kappa_1+\kappa_2}\left\{1 - \frac{2\kappa_2}{\kappa_1-\kappa_2}\sum_{j=1}^{\infty}\left[(-\gamma_{1,2}\gamma_{2,3})^j\operatorname{erfc}\left(j\sqrt{\frac{\tau_2}{t}}\right)\right]\right\} \tag{B95}$$

where the infinite series in Equation B95 converges for $|\gamma_{1,2}\gamma_{2,3}| < 1$. The limit of $\bar{u}_{\text{int}}^{\text{3L,dl}}$ as $t \to 0^+$ is given by

$$t \to 0^+ \implies \operatorname{erfc}\left(j\sqrt{\frac{\tau_2}{t}}\right) \to 0 \tag{B96}$$

$$\bar{u}_{\text{int},t\to 0^+}^{\text{3L,dl}} \to \frac{\sqrt{\pi}}{\kappa_1+\kappa_2} \tag{B97}$$

Using the infinite sum $\sum_{j=1}^{\infty}(-\gamma_{1,2}\gamma_{2,3})^j = -\gamma_{1,2}\gamma_{2,3}/(1+\gamma_{1,2}\gamma_{2,3})$ for $|\gamma_{1,2}\gamma_{2,3}| < 1$, the limit of $u_{\text{int}}^{\text{3L,dl}}$ as $t \to \infty$ is given by

$$t \to \infty \implies \operatorname{erfc}\left(j\sqrt{\frac{\tau_2}{t}}\right) \to 1 \tag{B98}$$

$$\bar{u}_{\text{int},t\to\infty}^{\text{3L,dl}}(t) \to \frac{\sqrt{\pi}}{\kappa_1+\kappa_2}\left\{1 - \frac{2\kappa_2}{\kappa_1-\kappa_2}\sum_{j=1}^{\infty}\left[(-\gamma_{1,2}\gamma_{2,3})^j\right]\right\} \tag{B99}$$

$$\bar{u}_{\text{int},t\to\infty}^{\text{3L,dl}}(t) \to \frac{\sqrt{\pi}}{\kappa_1+\kappa_2}\left\{1 + \frac{2\kappa_2}{\kappa_1-\kappa_2}\left(\frac{\gamma_{1,2}\gamma_{2,3}}{1+\gamma_{1,2}\gamma_{2,3}}\right)\right\} \tag{B100}$$

$$\bar{u}^{3L,dl}_{int,t\to\infty}(t) \to \frac{\sqrt{\pi}}{\kappa_1+\kappa_2}\left\{1+\frac{2\kappa_2}{\kappa_1-\kappa_2}\left[\frac{(\kappa_1-\kappa_2)(\kappa_2-\kappa_3)}{2\kappa_2(\kappa_1+\kappa_3)}\right]\right\} \tag{B101}$$

$$\bar{u}^{3L,dl}_{int,t\to\infty}(t) \to \frac{\sqrt{\pi}}{\kappa_1+\kappa_3} \tag{B102}$$

B.3 Normalized Interfacial Temperature Change in a Three-Layer Heat Transfer System

The Laplace-domain expression for normalized interfacial temperature change during diffusion-limited interfacial heat release in a three-layer heat transfer system ($\Theta^{3L,dl}_{int}$, Equation A54) can be expanded in series by applying the binomial theorem to the denominator [79]

$$\Theta^{3L,dl}_{int}(s) = \frac{1}{\gamma_{1,2}\gamma_{2,3}s}\left\{(1+\gamma_{1,2}\gamma_{2,3})\sum_{j=0}^{\infty}\left[(-\gamma_{1,2}\gamma_{2,3})^j \exp(-2j\sqrt{\tau_2 s})\right]-1\right\} \tag{B103}$$

$$\Theta^{3L,dl}_{int}(s) = \frac{1}{s}\left\{1+(1+\gamma_{1,2}\gamma_{2,3})\sum_{j=1}^{\infty}\left[(-1)^j(\gamma_{1,2}\gamma_{2,3})^{j-1} \exp(-2j\sqrt{\tau_2 s})\right]\right\} \tag{B104}$$

Again using Bateman 1954, Section 5.6, Number 3 [80], the Laplace-domain series expansion for $\Theta^{3L,dl}_{int}$ can be inverted to give a time-domain series expansion for $\theta^{3L,dl}_{int}$

$$\theta^{3L,dl}_{int}(t) = 1+(1+\gamma_{1,2}\gamma_{2,3})\sum_{j=1}^{\infty}\left[(-1)^j(\gamma_{1,2}\gamma_{2,3})^{j-1}\,\mathrm{erfc}\left(j\sqrt{\frac{\tau_2}{t}}\right)\right] \tag{B105}$$

$$\theta^{3L,dl}_{int}(t) = 1+(1+\gamma_{1,2}\gamma_{2,3})\sum_{j=1}^{\infty}\left[(-1)^j(\gamma_{1,2}\gamma_{2,3})^{j-1}\right]-(1+\gamma_{1,2}\gamma_{2,3})\sum_{j=1}^{\infty}\left[(-1)^j(\gamma_{1,2}\gamma_{2,3})^{j-1}\,\mathrm{erf}\left(j\sqrt{\frac{\tau_2}{t}}\right)\right] \tag{B106}$$

$$\theta^{3L,dl}_{int}(t) = (1+\gamma_{1,2}\gamma_{2,3})\sum_{j=0}^{\infty}\left\{(-\gamma_{1,2}\gamma_{2,3})^j\,\mathrm{erf}\left[(j+1)\sqrt{\frac{\tau_2}{t}}\right]\right\} \tag{B107}$$

noting that $\sum_{j=0}^{\infty}(-\gamma_{1,2}\gamma_{2,3})^j = 1/(1+\gamma_{1,2}\gamma_{2,3})$ for $|\gamma_{1,2}\gamma_{2,3}|<1$. Equation B107 can be expressed as an expansion in the thermal effusivity difference-to-sum ratios $\gamma_{1,2}$ and $\gamma_{2,3}$ giving

$$\theta^{3L,dl}_{int}(t) = \mathrm{erf}\left(\sqrt{\frac{\tau_2}{t}}\right)+\sum_{j=1}^{\infty}\left[(-\gamma_{1,2}\gamma_{2,3})^j\left\{\mathrm{erf}\left[(j+1)\sqrt{\frac{\tau_2}{t}}\right]-\mathrm{erf}\left(j\sqrt{\frac{\tau_2}{t}}\right)\right\}\right] \tag{B108}$$

For $\gamma_{1,2}\gamma_{2,3} \ll 1$, zeroth- and second-order approximations in γ for normalized interfacial temperature change ($\theta^{3L,dl}_{int,\mathcal{O}(\gamma^0)}$ and $\theta^{3L,dl}_{int,\mathcal{O}(\gamma^2)}$, respectively) are

$$\theta^{3L,dl}_{int,\mathcal{O}(\gamma^0)}(t) = \mathrm{erf}\left(\sqrt{\frac{\tau_2}{t}}\right) \tag{B109}$$

$$\theta^{3L,dl}_{int,\mathcal{O}(\gamma^2)}(t) = \mathrm{erf}\left(\sqrt{\frac{\tau_2}{t}}\right)-\gamma_{1,2}\gamma_{2,3}\left[\mathrm{erf}\left(2\sqrt{\frac{\tau_2}{t}}\right)-\mathrm{erf}\left(\sqrt{\frac{\tau_2}{t}}\right)\right] \tag{B110}$$

C Heat Fluxes at the Reaction Interface

The heat fluxes away from the reaction interface into layer 1 ($q_{1,\text{int}}$ defined as positive in the negative z direction) and layer 2 ($q_{2,\text{int}}$ defined as positive in the positive z direction) for an arbitrary planar source intensity can be defined as

$$q_{1,\text{int}}(0,t) = k_1 \frac{\partial u_1}{\partial z}(0,t) \tag{C111}$$

$$q_{2,\text{int}}(0,t) = -k_2 \frac{\partial u_2}{\partial z}(0,t) \tag{C112}$$

The sum of the heat fluxes into layers 1 and 2 is equal to the total rate of interfacial heat release $q_{1,\text{int}}(t) + q_{2,\text{int}}(t) = q(t)$, in accordance with the heat flux boundary condition at $z = 0$ (Section 2.2).

C.1 Laplace-Domain Heat Flux Expressions

Laplace transforms of the heat fluxes at the reaction interface into layer 1 ($Q_{1,\text{int}}$) and layer 2 ($Q_{2,\text{int}}$) for an arbitrary planar source intensity can be defined as

$$Q_{1,\text{int}}(s) = k_1 \frac{dU_1}{dz}(0,s) \tag{C113}$$

$$Q_{2,\text{int}}(s) = -k_2 \frac{dU_2}{dz}(0,s) \tag{C114}$$

noting that $Q_{1,\text{int}}$ is defined as positive toward $z \to -\infty$ and $Q_{2,\text{int}}$ defined as positive toward $z \to +\infty$. Expressions for $Q_{1,\text{int}}$ and $Q_{2,\text{int}}$ in terms of the thermal properties of each fluid or material layer can be derived by solving the heat transfer model to determine the Laplace transform of the temperature gradient in each layer as a function of position (Equation 10).

For a two-layer heat transfer system (e.g., support-free interfacial polymerization) with diffusion-limited interfacial heat release, the Laplace transforms of the normalized heat fluxes away from the reaction interface into layers 1 and 2 ($\bar{Q}^{\text{2L,dl}}_{1,\text{int}}$ and $\bar{Q}^{\text{2L,dl}}_{2,\text{int}}$, respectively) are

$$\bar{Q}^{\text{2L,dl}}_{1,\text{int}}(s) = \frac{\kappa_1 \sqrt{\pi}}{\sqrt{s}(\kappa_1 + \kappa_2)} \tag{C115}$$

$$\bar{Q}^{\text{2L,dl}}_{2,\text{int}}(s) = \frac{\kappa_2 \sqrt{\pi}}{\sqrt{s}(\kappa_1 + \kappa_2)} \tag{C116}$$

where heat fluxes have been normalized by the reaction-specific diffusion-limited interfacial heat release constant ($q_0\sqrt{t_0}$, units W s$^{\frac{1}{2}}$ m^{-2}) where $\bar{Q}^{n\text{L,dl}}_{i,\text{int}} = Q^{n\text{L,dl}}_{i,\text{int}}/(q_0\sqrt{t_0})$ and $\bar{Q}^{\text{dl}} = Q^{\text{dl}}/(q_0\sqrt{t_0}) = \sqrt{\pi/s}$.

Similarly, for a three-layer heat transfer system (e.g., conventional interfacial polymerization) with diffusion-limited interfacial heat release, the Laplace transforms of the normalized heat fluxes away from the reaction interface into layers 1 and 2 ($\bar{Q}^{\text{3L,dl}}_{1,\text{int}}$ and $\bar{Q}^{\text{3L,dl}}_{2,\text{int}}$, respectively) are

$$\bar{Q}^{\text{3L,dl}}_{1,\text{int}}(s) = \frac{\kappa_1 \sqrt{\pi}}{\sqrt{s}(\kappa_1 + \kappa_2)} \left[\frac{1 + \gamma_{2,3} \exp(-2\sqrt{\tau_2 s})}{1 + \gamma_{1,2}\gamma_{2,3} \exp(-2\sqrt{\tau_2 s})} \right] \tag{C117}$$

$$\bar{Q}^{\text{3L,dl}}_{2,\text{int}}(s) = \frac{\kappa_2 \sqrt{\pi}}{\sqrt{s}(\kappa_1 + \kappa_2)} \left[\frac{1 - \gamma_{2,3} \exp(-2\sqrt{\tau_2 s})}{1 + \gamma_{1,2}\gamma_{2,3} \exp(-2\sqrt{\tau_2 s})} \right] \tag{C118}$$

where $\gamma_{i,j} = (\kappa_i - \kappa_j)/(\kappa_i + \kappa_j)$, noting that $|\gamma_{i,j}| < 1 \ \forall \ i, j \in 1, ..., n$ given that $\kappa_i > 0 \ \forall \ i \in 1, ..., n$, and $\tau_i = d_i^2/\alpha_i$ is characteristic timescale for heat conduction though finite layer i.

Similarly, for a four-layer heat transfer system (e.g., interlayer-modulated interfacial polymerization) with diffusion-limited interfacial heat release, the Laplace transforms of the normalized heat fluxes away from the reaction interface into layers 1 and 2 ($\bar{Q}_{1,\text{int}}^{\text{4L,dl}}$ and $\bar{Q}_{2,\text{int}}^{\text{4L,dl}}$, respectively) are

$$\bar{Q}_{1,\text{int}}^{\text{4L,dl}}(s) = \frac{\kappa_1\sqrt{\pi}}{\sqrt{s}(\kappa_1+\kappa_2)}\left\{\frac{1+\gamma_{2,3}\exp(-2\sqrt{\tau_2 s})+\gamma_{2,3}\gamma_{3,4}\exp(-2\sqrt{\tau_3 s})+\gamma_{3,4}\exp[-2(\sqrt{\tau_2 s}+\sqrt{\tau_3 s})]}{1+\gamma_{1,2}\gamma_{2,3}\exp(-2\sqrt{\tau_2 s})+\gamma_{2,3}\gamma_{3,4}\exp(-2\sqrt{\tau_3 s})+\gamma_{1,2}\gamma_{3,4}\exp[-2(\sqrt{\tau_2 s}+\sqrt{\tau_3 s})]}\right\} \tag{C119}$$

$$\bar{Q}_{2,\text{int}}^{\text{4L,dl}}(s) = \frac{\kappa_2\sqrt{\pi}}{\sqrt{s}(\kappa_1+\kappa_2)}\left\{\frac{1-\gamma_{2,3}\exp(-2\sqrt{\tau_2 s})+\gamma_{2,3}\gamma_{3,4}\exp(-2\sqrt{\tau_3 s})-\gamma_{3,4}\exp[-2(\sqrt{\tau_2 s}+\sqrt{\tau_3 s})]}{1+\gamma_{1,2}\gamma_{2,3}\exp(-2\sqrt{\tau_2 s})+\gamma_{2,3}\gamma_{3,4}\exp(-2\sqrt{\tau_3 s})+\gamma_{1,2}\gamma_{3,4}\exp[-2(\sqrt{\tau_2 s}+\sqrt{\tau_3 s})]}\right\} \tag{C120}$$

Figure C1 shows the normalized heat flux into layers 1 ($\bar{q}_{1,\text{int}}^{n\text{L,dl}} = q_{1,\text{int}}^{n\text{L,dl}}/(q_0\sqrt{t_0})$, orange curves) and 2 ($\bar{q}_{2,\text{int}}^{n\text{L,dl}} = q_{2,\text{int}}^{n\text{L,dl}}/(q_0\sqrt{t_0})$, blue curves) at the reaction interface as a function of reaction time for (a) two-, (b) three-, and (c) four-layer heat transfer systems with diffusion-limited interfacial heat release. The fraction of heat conducted into layer 1 ($\bar{q}_{1,\text{int}}^{n\text{L,dl}}/\bar{q}^{\text{dl}}$, yellow shading) from the planar heat source at the reaction interface ($z = 0$) is also shown for (d) two-, (e) three-, and (f) four-layer heat transfer systems. The remainder of the heat is conducted into layer 2 ($\bar{q}_{2,\text{int}}^{n\text{L,dl}}/\bar{q}^{\text{dl}}$) comprising the infinite aqueous fluid (two-layer system, blue shading), finite support layer (three-layer system, green shading), or the finite interlayer (four-layer system, pink shading). In each case, the support layer and the interlayer are 100 μm thick polysulfone (layer 2 in b and e, layer 3 in c and f) and 100 nm thick pyrolytic graphite in a perpendicular orientation (layer 2 in c and f), respectively (Table E1). Characteristic timescales for heat conduction through finite (τ_2 in b and e) layer 2 and (τ_2 and τ_3 in c and f) layers 2 and 3 are indicated (vertical dashed lines).

In a two-layer heat transfer system (Figure C1d) with diffusion-limited interfacial heat release, the fraction of heat conducted into layer 2 ($\bar{q}_{2\text{int}}^{\text{2L,dl}}/\bar{q}^{\text{dl}} = 1 - (\bar{q}_{1,\text{int}}^{\text{2L,dl}}/\bar{q}^{\text{dl}})$) is constant with respect to reaction time, having a value of (i) $\kappa_2/(\kappa_1+\kappa_2)$. In a three-layer system (Figure C1e), $\bar{q}_{2\text{int}}^{\text{3L,dl}}/\bar{q}^{\text{dl}}$ decreases from (ii) $\kappa_2/(\kappa_1+\kappa_2)$ for $t \ll \tau_2$ to (iii) $\kappa_3/(\kappa_1+\kappa_3)$ when $t \gg \tau_2$ as heat transfer in the positive z direction is initially governed by heat conduction through finite layer 2 before conduction through infinite layer 3 dominates. Similarly, in a four-layer system (Figure C1f), $\bar{q}_{2\text{int}}^{\text{4L,dl}}/\bar{q}^{\text{dl}}$ changes from (iv) $\kappa_2/(\kappa_1+\kappa_2)$ for $t \ll \tau_2$ to (v) $\kappa_3/(\kappa_1+\kappa_3)$ for $\tau_2 \ll t \ll \tau_3$ and finally (vi) $\kappa_4/(\kappa_1+\kappa_4)$ for $t \gg \tau_3$, provided that $\tau_2 \ll \tau_3$.

C.2 Time-Domain Heat Flux Expressions

The Laplace-domain expressions for interfacial heat flux into layers 1 ($\bar{Q}_{1,\text{int}}^{\text{2L,dl}}$) and 2 ($\bar{Q}_{2,\text{int}}^{\text{2L,dl}}$) in a two-layer heat transfer system with diffusion-limited interfacial heat release can be inverted using Bateman 1954, Section 5.3, Number 21 [80] to give time-domain expressions:

$$\bar{q}_{1,\text{int}}^{\text{2L,dl}}(s) = \frac{\kappa_1}{\sqrt{t}(\kappa_1+\kappa_2)} \tag{C121}$$

$$\bar{q}_{2,\text{int}}^{\text{2L,dl}}(s) = \frac{\kappa_2}{\sqrt{t}(\kappa_1+\kappa_2)} \tag{C122}$$

The Laplace-domain expression for interfacial heat flux into layer 1 ($\bar{Q}_{1,\text{int}}^{\text{3L,dl}}$) in a three-layer heat transfer system with diffusion-limited interfacial heat release can be expanded in series by applying the

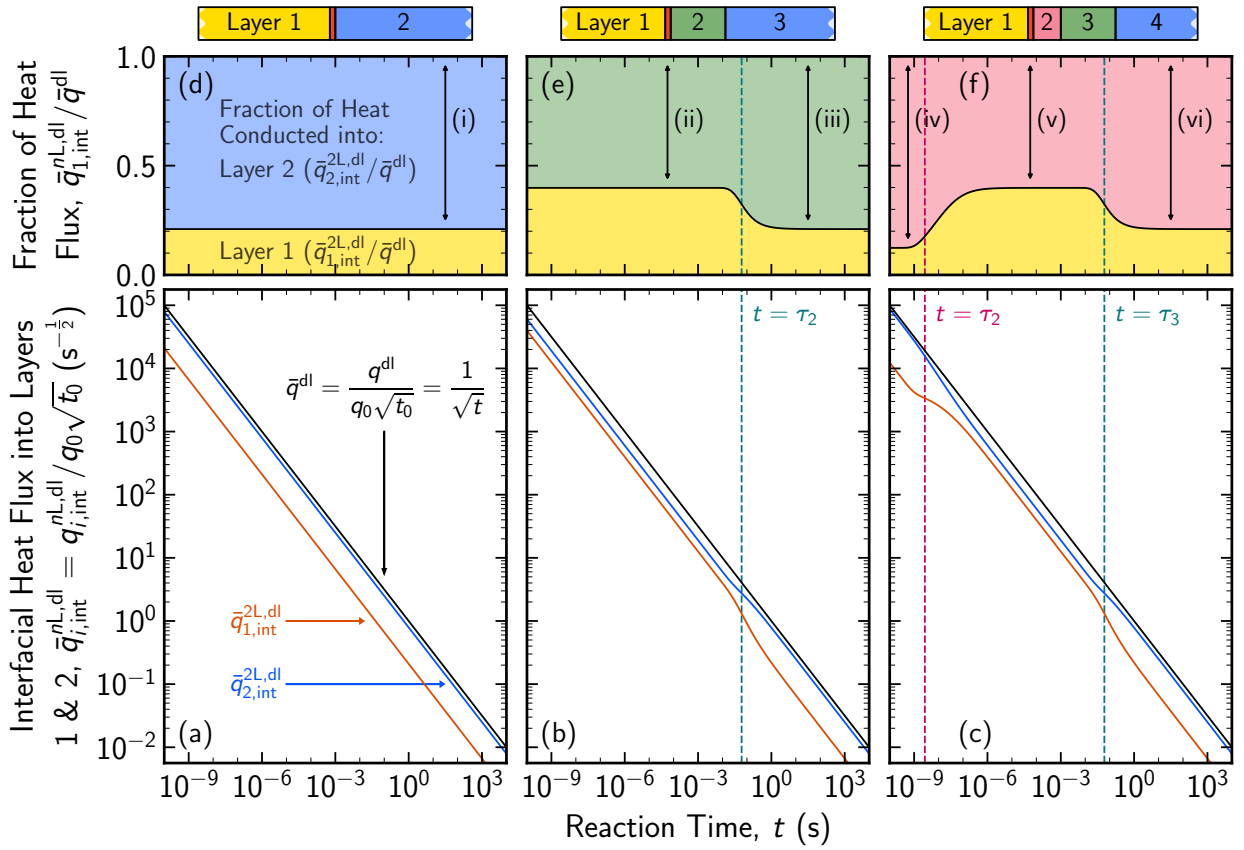

Figure C1: (a–c) Interfacial heat fluxes into layers 1 ($\bar{q}^{nL,dl}_{1,int} = q^{nL,dl}_{1,int}/(q_0\sqrt{t_0})$, orange curves) and 2 ($\bar{q}^{nL,dl}_{2,int}$, blue) at the reaction interface ($z = 0$) during diffusion-limited heat release ($\bar{q}^{dl} = q^{dl}/(q_0\sqrt{t_0}) = 1/\sqrt{t}$, black) in (a) two-, (b) three-, and (c) four-layer heat transfer systems as a function of reaction time (t). (d–f) Fraction of interfacial heat flux conducted into layer 1 ($\bar{q}^{nL,dl}_{1,int}/\bar{q}^{dl}$, yellow shading) during diffusion-limited heat release ($\bar{q}^{dl} = 1/\sqrt{t}$) in (d) two-, (e) three-, and (f) four-layer heat transfer systems. Interfacial heat fluxes into layers 1 and 2 are calculated using time-domain solutions (a) Equations C121 and C122 and (b) Equations C129 and C131 or by numerically inverting Laplace-domain expressions (c) Equations C119 and C120. The support layer and the interlayer are 100 μm thick polysulfone (layer 2 in b and e, layer 3 in c and f) and 100 nm thick pyrolytic graphite in a perpendicular orientation (layer 2 in e and f), respectively (Table E1).

binomial theorem to the denominator:

$$\bar{Q}^{3L,dl}_{1,int}(s) = \frac{\kappa_1\sqrt{\pi}}{\sqrt{s}(\kappa_1+\kappa_2)}\left[\frac{1+\gamma_{2,3}\exp(-2\sqrt{\tau_2 s})}{1+\gamma_{1,2}\gamma_{2,3}\exp(-2\sqrt{\tau_2 s})}\right] \tag{C123}$$

$$\bar{Q}^{3L,dl}_{1,int}(s) = \frac{\kappa_1\sqrt{\pi}}{\sqrt{s}(\kappa_1+\kappa_2)}[1+\gamma_{2,3}\exp(-2\sqrt{\tau_2 s})]\sum_{j=0}^{\infty}\left[(-\gamma_{1,2}\gamma_{2,3})^j\exp(-2j\sqrt{\tau_2 s})\right] \tag{C124}$$

noting that $|\gamma_{1,2}\gamma_{2,3}| < 1$ given that $\kappa_i > 0 \; \forall \; i \in 1,...,n$. Rearranging gives

$$\bar{Q}^{3L,dl}_{1,int}(s) = \frac{\kappa_1\sqrt{\pi}}{\sqrt{s}(\kappa_1+\kappa_2)}\left\{\sum_{j=0}^{\infty}\left[(-\gamma_{2,3})^j \exp(-2j\sqrt{\tau_2 s})\right] + \gamma_{2,3}\sum_{j=0}^{\infty}\left[(-\gamma_{1,2}\gamma_{2,3})^j \exp(-2(j+1)\sqrt{\tau_2 s})\right]\right\} \tag{C125}$$

$$\bar{Q}^{3L,dl}_{1,int}(s) = \frac{\kappa_1\sqrt{\pi}}{\sqrt{s}(\kappa_1+\kappa_2)}\left\{\sum_{j=0}^{\infty}\left[(-\gamma_{2,3})^j \exp(-2j\sqrt{\tau_2 s})\right] - \frac{1}{\gamma_{1,2}}\sum_{j=1}^{\infty}\left[(-\gamma_{1,2}\gamma_{2,3})^j \exp(-2j\sqrt{\tau_2 s})\right]\right\} \tag{C126}$$

$$\bar{Q}^{3L,dl}_{1,int}(s) = \frac{\kappa_1\sqrt{\pi}}{\sqrt{s}(\kappa_1+\kappa_2)}\left\{1 + \left[1-\frac{1}{\gamma_{1,2}}\right]\sum_{j=1}^{\infty}\left[(-\gamma_{1,2}\gamma_{2,3})^j \exp(-2j\sqrt{\tau_2 s})\right]\right\} \tag{C127}$$

$$\bar{Q}^{3L,dl}_{1,int}(s) = \frac{\kappa_1\sqrt{\pi}}{\kappa_1+\kappa_2}\left\{\frac{1}{\sqrt{s}} - \frac{2\kappa_2}{\kappa_1-\kappa_2}\sum_{j=1}^{\infty}\left[\frac{(-\gamma_{1,2}\gamma_{2,3})^j \exp(-2j\sqrt{\tau_2 s})}{\sqrt{s}}\right]\right\} \tag{C128}$$

The Laplace-domain series expansion for $\bar{Q}^{3L,dl}_{1,int}$ can be inverted using Bateman 1954, Section 5.3, Number 21 and Section 5.6, Number 6 [80] to give a time-domain series expansion:

$$\bar{q}^{3L,dl}_{1,int}(s) = \frac{\kappa_1}{\sqrt{t}(\kappa_1+\kappa_2)}\left\{1 - \frac{2\kappa_2}{\kappa_1-\kappa_2}\sum_{j=1}^{\infty}\left[(-\gamma_{1,2}\gamma_{2,3})^j \exp\left(-\frac{j^2\tau_2}{t}\right)\right]\right\} \tag{C129}$$

Similarly, the Laplace-domain expression for interfacial heat flux into layer 2 ($\bar{Q}^{3L,dl}_{2,int}$) in a three-layer heat transfer system with diffusion-limited interfacial heat release can be inverted to give a time-domain series expansion:

$$\bar{Q}^{3L,dl}_{2,int}(s) = \frac{\kappa_2\sqrt{\pi}}{\sqrt{s}(\kappa_1+\kappa_2)}\left[\frac{1-\gamma_{2,3}\exp(-2\sqrt{\tau_2 s})}{1+\gamma_{1,2}\gamma_{2,3}\exp(-2\sqrt{\tau_2 s})}\right] \tag{C130}$$

$$\bar{q}^{3L,dl}_{2,int}(s) = \frac{\kappa_2}{\sqrt{t}(\kappa_1+\kappa_2)}\left\{1 + \frac{2\kappa_1}{\kappa_1-\kappa_2}\sum_{j=1}^{\infty}\left[(-\gamma_{1,2}\gamma_{2,3})^j \exp\left(-\frac{j^2\tau_2}{t}\right)\right]\right\} \tag{C131}$$

noting that the sum of the heat fluxes into layer 1 and 2 is equal to the total rate of diffusion-limited heat release in the time- and Laplace-domains where $\bar{q}^{3L,dl}_{1,int}(t) + \bar{q}^{3L,dl}_{2,int}(t) = 1/\sqrt{t}$ and $\bar{Q}^{3L,dl}_{1,int}(s) + \bar{Q}^{3L,dl}_{2,int}(s) = \sqrt{\pi/s}$, respectively.

D Numerical Function and Inverse Laplace Transform Evaluation

Infinite series summations, which appear in expressions for $\bar{u}^{3L,dl}_{int}(t)$, $\theta^{3L,dl}_{int}(t)$, $\bar{q}^{3L,dl}_{1,int}(t)$, and $\bar{q}^{3L,dl}_{2,int}(t)$, were evaluated using Richardson extrapolation through the `nsum` function implemented in the `mpmath` library in Python with 25-digit precision [81–83]. The Laplace-domain expressions for $\bar{U}^{4L,dl}_{int}(s)$, $\bar{U}^{3L,dl}_{1}(z,s)$, $\bar{U}^{3L,dl}_{2}(z,s)$, $\bar{U}^{3L,dl}_{3}(z,s)$, $\bar{U}^{4L,dl}_{1}(z,s)$, $\bar{U}^{4L,dl}_{2}(z,s)$, $\bar{U}^{4L,dl}_{3}(z,s)$, and $\bar{U}^{4L,dl}_{4}(z,s)$ derived in Appendix A and $\bar{Q}^{4L,dl}_{1,int}(s)$ and $\bar{Q}^{4L,dl}_{2,int}(s)$ derived in Appendix C.2 were inverted numerically using Talbot's method to integrate the Bromwich contour through the `invertlaplace` function implemented in the `mpmath` library in Python with 25-digit precision [81, 84].

E Thermal Diffusivity and Thermal Effusivity Data

Table E1: Thermal diffusivity and thermal effusivity of solvents, polymers, metals, and inorganic materials. Data is from Suryanarayana 1995 [62], Lienhard and Lienhard 2019 [52], Wu 2018 [65], the Thermtest Materials Thermal Properties Database [66], the Chemicals library [67], and the CoolProp library [68].

Material	Thermal Diffusivity ($m^2\ s^{-1}$)	Thermal Effusivity ($W\ s^{\frac{1}{2}}\ m^{-2}\ K^{-1}$)	Data Source
Solvents			
Water	1.45×10^{-7}	1.59×10^{3}	[68]
n-Hexane	8.03×10^{-8}	4.22×10^{2}	[67]
n-Heptane	8.16×10^{-8}	4.36×10^{2}	[67]
n-Octane	8.15×10^{-8}	4.47×10^{2}	[67]
n-Nonane	8.20×10^{-8}	4.55×10^{2}	[67]
n-Decane	8.19×10^{-8}	4.60×10^{2}	[67]
n-Hexadecane	8.35×10^{-8}	4.92×10^{2}	[67]
2,3-Dimethylbutane	7.24×10^{-8}	3.89×10^{2}	[67]
1,2,3-Trimethylbenzene	8.11×10^{-8}	4.57×10^{2}	[67]
1,2,4-Trimethylbenzene	8.29×10^{-8}	4.49×10^{2}	[67]
2,3,3-Trimethylpentane	6.89×10^{-8}	4.07×10^{2}	[67]
2,2,4-Trimethylpentane	6.80×10^{-8}	3.77×10^{2}	[67]
Cyclopentane	9.27×10^{-8}	4.15×10^{2}	[67]
Cyclopentene	9.80×10^{-8}	4.31×10^{2}	[67]
Cyclohexane	8.68×10^{-8}	4.19×10^{2}	[67]
Cyclohexene	9.04×10^{-8}	4.38×10^{2}	[67]
Methylcyclohexane	7.69×10^{-8}	4.00×10^{2}	[67]
Ethylcyclohexane	7.87×10^{-8}	4.15×10^{2}	[67]
1,1-Dimethylcyclohexane	8.00×10^{-8}	4.09×10^{2}	[67]
cis-1,2-Dimethylcyclohexane	7.96×10^{-8}	4.19×10^{2}	[67]
trans-1,2-Dimethylcyclohexane	7.97×10^{-8}	4.07×10^{2}	[67]
Benzene	9.43×10^{-8}	4.67×10^{2}	[67]
Toluene	8.97×10^{-8}	4.42×10^{2}	[67]
o-Xylene	8.55×10^{-8}	4.49×10^{2}	[67]
m-Xylene	8.78×10^{-8}	4.39×10^{2}	[67]
p-Xylene	8.86×10^{-8}	4.36×10^{2}	[67]
Ethylbenzene	8.65×10^{-8}	4.38×10^{2}	[67]
Propylbenzene	8.34×10^{-8}	4.43×10^{2}	[67]
Butylbenzene	8.19×10^{-8}	4.45×10^{2}	[67]
Cumene	8.18×10^{-8}	4.31×10^{2}	[67]
1-Hexene	8.27×10^{-8}	4.19×10^{2}	[67]
1-Heptene	8.32×10^{-8}	4.32×10^{2}	[67]

1-Octene	8.16×10^{-8}	4.37×10^{2}	[67]
1-Decene	8.23×10^{-8}	4.54×10^{2}	[67]
Styrene	8.68×10^{-8}	4.63×10^{2}	[67]
Methyl acetate	8.63×10^{-8}	5.22×10^{2}	[67]
Ethyl acetate	8.31×10^{-8}	4.99×10^{2}	[67]
Propyl acetate	8.31×10^{-8}	4.89×10^{2}	[67]
Butyl acetate	8.03×10^{-8}	4.87×10^{2}	[67]
Ethyl formate	8.69×10^{-8}	5.44×10^{2}	[67]
Ethyl mercaptan	8.75×10^{-8}	4.68×10^{2}	[67]
Diethyl ether	7.78×10^{-8}	4.60×10^{2}	[67]
Dibutyl ether	7.83×10^{-8}	4.57×10^{2}	[67]
Methyl *tert*-butyl ether	7.96×10^{-8}	4.42×10^{2}	[67]
Dimethyl sulfide	8.78×10^{-8}	4.75×10^{2}	[67]
Diethyl sulfide	8.38×10^{-8}	4.58×10^{2}	[67]
Hexanal	8.04×10^{-8}	4.82×10^{2}	[67]
Heptanal	8.38×10^{-8}	4.75×10^{2}	[67]
o-Dichlorobenzene	8.43×10^{-8}	4.17×10^{2}	[67]
Chloroform	8.28×10^{-8}	4.08×10^{2}	[67]
Chlorobenzene	8.65×10^{-8}	4.32×10^{2}	[67]
Polymers			
Polysulfone	1.651×10^{-7}	6.374×10^{2}	[66]
Polyoxymethylene	1.547×10^{-7}	8.211×10^{2}	[66]
Polyamide (nylon 6-6)	1.518×10^{-7}	6.416×10^{2}	[66]
Polyamide (nylon 6-12)	1.235×10^{-7}	6.259×10^{2}	[66]
Polycarbonate	1.933×10^{-7}	6.595×10^{2}	[62]
Polyethylene (high-density)	1.521×10^{-7}	8.461×10^{2}	[66]
Polyethylene (low-density)	1.708×10^{-7}	7.985×10^{2}	[66]
Polyimide	2.166×10^{-7}	7.520×10^{2}	[66]
Polypropylene	1.076×10^{-7}	5.640×10^{2}	[62]
Polystyrene	9.259×10^{-8}	4.272×10^{2}	[66]
Polytetrafluoroethylene	1.082×10^{-7}	7.599×10^{2}	[62]
Polyvinyl chloride	8.098×10^{-8}	3.514×10^{2}	[62]
Polymethyl methacrylate	1.210×10^{-7}	6.009×10^{2}	[66]
Polyvinyl alcohol	1.785×10^{-7}	6.628×10^{2}	[65]
Polyvinylidene fluoride	5.184×10^{-8}	5.534×10^{2}	[66]
Polyvinylidene chloride	5.535×10^{-8}	5.355×10^{2}	[66]
Polyethylene terephthalate	9.290×10^{-8}	4.750×10^{2}	[63, 64]
Metals			
Aluminium	9.713×10^{-5}	2.405×10^{4}	[62]
Aluminium alloy (2024-T6)	7.303×10^{-5}	2.071×10^{4}	[62]
Brass	3.322×10^{-5}	1.891×10^{4}	[52]
Beryllium	5.924×10^{-5}	2.599×10^{4}	[62]

Bronze (90% Cu, 10% Al)	1.407×10^{-5}	1.386×10^{4}	[62]
Bronze (89% Cu, 11% Sn)	1.732×10^{-5}	1.297×10^{4}	[62]
Bronze (70% Cu, 30% Zn)	3.394×10^{-5}	1.888×10^{4}	[62]
Cadmium	4.844×10^{-5}	1.391×10^{4}	[62]
Chromium	2.915×10^{-5}	1.736×10^{4}	[62]
Cobalt	2.659×10^{-5}	1.924×10^{4}	[62]
Copper	1.166×10^{-4}	3.714×10^{4}	[62]
Constantan (55% Cu, 45% Ni)	6.715×10^{-6}	8.876×10^{3}	[62]
Duralumin (95.5% Cu, 4.0% Cu, 0.5% Ni)	2.009×10^{4}	2.461×10^{6}	[52]
Germanium	3.471×10^{-5}	1.017×10^{4}	[62]
Gold	1.273×10^{-4}	2.809×10^{4}	[62]
Iridium	5.026×10^{-5}	2.074×10^{4}	[62]
Iron	2.280×10^{-5}	1.680×10^{4}	[62]
Iron (99.75% pure)	2.067×10^{-5}	1.599×10^{4}	[62]
Iron (cast, 4% C)	1.703×10^{-5}	1.260×10^{4}	[62]
Carbon Steel (AISI 1010)	1.775×10^{-5}	1.436×10^{4}	[62]
Carbon Steel (Carbon-Silicon)	1.489×10^{-5}	1.345×10^{4}	[62]
Carbon Steel (Carbon-Manganese-Silicon)	1.162×10^{-5}	1.203×10^{4}	[62]
Chromium Steel (0.18% C, 0.65% Cr, 0.23% Mo, 0.60% Si)	1.086×10^{-5}	1.144×10^{4}	[62]
Chromium Steel (0.16% C, 1.00% Cr, 0.54% Mo)	1.218×10^{-5}	1.212×10^{4}	[62]
Chromium Steel (0.20% C, 1.02% Cr, 0.15% V)	1.409×10^{-5}	1.303×10^{4}	[62]
Silver	1.719×10^{-4}	3.257×10^{4}	[52]
Stainless Steel (AISI 302)	3.905×10^{-6}	7.641×10^{3}	[62]
Stainless Steel (AISI 304)	3.954×10^{-6}	7.493×10^{3}	[62]
Stainless Steel (AISI 316)	3.476×10^{-6}	7.188×10^{3}	[62]
Stainless Steel (AISI 347)	3.708×10^{-6}	7.374×10^{3}	[62]
Lead	2.413×10^{-5}	7.186×10^{3}	[62]
Magnesium	8.755×10^{-5}	1.667×10^{4}	[62]
Molybdenum	5.369×10^{-5}	1.883×10^{4}	[62]
Nickel	2.295×10^{-5}	1.893×10^{4}	[62]
Nichrome (80% Ni, 20% Cr)	3.401×10^{-6}	6.507×10^{3}	[62]
Palladium	2.448×10^{-5}	1.451×10^{4}	[62]
Platinum	2.510×10^{-5}	1.429×10^{4}	[62]
Platinum alloy (60% Pt, 40% Rh)	1.745×10^{-5}	1.125×10^{4}	[62]
Rhodium	4.958×10^{-5}	2.130×10^{4}	[62]
Silicon	8.921×10^{-5}	1.567×10^{4}	[62]
Silver	1.739×10^{-4}	3.254×10^{4}	[62]
Tantalum	2.474×10^{-5}	1.156×10^{4}	[62]
Thorium	3.911×10^{-5}	8.634×10^{3}	[62]
Tin	4.014×10^{-5}	1.051×10^{4}	[62]
Titanium	9.323×10^{-6}	7.172×10^{3}	[62]
Tungsten	6.830×10^{-5}	2.105×10^{4}	[62]

Uranium	1.248×10^{-5}	7.814×10^{3}	[62]
Vanadium	1.029×10^{-5}	9.569×10^{3}	[62]
Zinc	4.176×10^{-5}	1.795×10^{4}	[62]
Zirconium	1.243×10^{-5}	6.439×10^{3}	[62]
Inorganic Materials			
Aluminum oxide (sapphire)	1.515×10^{-5}	1.182×10^{4}	[62]
Aluminum oxide (polycrystalline)	1.185×10^{-5}	1.046×10^{4}	[62]
Boron	9.991×10^{-6}	8.732×10^{3}	[62]
Boron fiber epoxy (parallel)	9.812×10^{-7}	2.312×10^{3}	[62]
Boron fiber epoxy (perpendicular)	2.528×10^{-7}	1.173×10^{3}	[62]
Graphite pyrolytic (perpendicular)	3.638×10^{-6}	2.989×10^{3}	[62]
Graphite fiber epoxy (parallel)	8.480×10^{-6}	3.812×10^{3}	[62]
Graphite fiber epoxy (perpendicular)	6.646×10^{-7}	1.067×10^{3}	[62]
Pyroceram	1.895×10^{-6}	2.892×10^{3}	[62]
Silicon carbide	2.846×10^{-6}	4.979×10^{3}	[62]
Silicon dioxide (parallel)	5.268×10^{-6}	4.531×10^{3}	[62]
Silicon dioxide (perpendicular)	3.145×10^{-6}	3.501×10^{3}	[62]
Silicon dioxide (fused silica)	8.344×10^{-7}	1.511×10^{3}	[62]
Silicon nitride	9.648×10^{-6}	5.151×10^{3}	[62]
Sulfur	1.433×10^{-7}	5.548×10^{2}	[62]
Thorium dioxide	6.072×10^{-6}	5.276×10^{3}	[62]
Titanium dioxide	2.846×10^{-6}	4.979×10^{3}	[62]

Nomenclature

A_i	K	Temperature field integration constant for layer i
B_i	K	Temperature field integration constant for layer i
$c_{\mathrm{P},i}$	J kg^{-1} K^{-1}	Isobaric specific heat capacity of layer i
d_i	m	Thickness of finite layer i (support layer or interlayer)
$\Delta_\mathrm{r}\underline{H}$	J kmol^{-1}	Enthalpy change of reaction per mole of rate-limiting monomer
i		Layer index
j		Summation index
k_i	W m^{-1} K^{-1}	Thermal conductivity of layer i
l	m	Length scale for heat transfer
n		Number of layers
q	W m^{-2}	Heat flux
q_0	W m^{-2}	Semi-empirical reaction-specific constant representing the planar heat source intensity at time t_0, defined as $q_0 = r_0\Delta_\mathrm{r}\underline{H}$
$q_0\sqrt{t_0}$	W s$^{\frac{1}{2}}$ m^{-2}	Reaction-specific diffusion-limited interfacial heat release constant
r	kmol m^{-2} s^{-1}	Molar flux of rate-limiting monomer
r_0	kmol m^{-2} s^{-1}	Semi-empirical reaction-specific constant representing the molar flux of rate-limiting monomer at time t_0
s	s^{-1}	Complex Laplace domain variable
t	s	Time elapsed since initiation of membrane formation
t_0	s	Semi-empirical reaction-specific constant
T	K	Temperature
u	K	Temperature deviation from environmental temperature reference state
$\bar{u}$	K W^{-1} s$^{-\frac{1}{2}}$ m^2	Temperature deviation from environmental temperature reference state divided by diffusion-limited interfacial heat release constant: $\bar{u} = u/q_0\sqrt{t_0}$
U	K	Laplace transform of temperature deviation from environmental temperature reference state
$\bar{U}$	K W^{-1} s$^{-\frac{1}{2}}$ m^2	Laplace transform of temperature deviation from environmental temperature reference state divided by diffusion-limited interfacial heat release constant: $\bar{U} = U/q_0\sqrt{t_0}$
z	m	Distance coordinate perpendicular to the reaction interface (positive towards layer n)

Greek Letters:

α_i	m^2 s^{-1}	Thermal diffusivity of layer i
$\gamma_{i,j}$		Thermal effusivity difference-to-sum ratio for layers i and j: $\gamma_{i,j} = (\kappa_i - \kappa_j)/(\kappa_i + \kappa_j)$
ε_i		Porosity of finite layer i
θ		Transient temperature normalized by initial ($t \to 0^+$) and final ($t \to \infty$) temperature values: $\theta = (u - u_{t\to\infty})/(u_{t\to 0^+} - u_{t\to\infty})$

Θ		Laplace transform of the transient temperature normalized by initial ($t \to 0^+$) and final ($t \to \infty$) temperature values: $\Theta = (U - U_{t\to\infty})/(u_{t\to 0^+} - u_{t\to\infty})$
κ_i	W $s^{\frac{1}{2}}$ m^{-2} K^{-1}	Thermal effusivity of layer i
ρ_i	kg m^{-3}	Mass density of layer i
τ_i	s	Timescale for heat conduction through finite layer i

Superscripts and Subscripts:

0	Constant in the diffusion-limited interfacial heat release model
am	Arithmetic mean
aq	Aqueous solution
den	Denominator for integration constant expressions
dl	Diffusion-limited interfacial heat release model
hm	Harmonic mean
int	Reaction interface ($z = 0$)
num	Numerator for integration constant expressions
org	Organic solution
nL	Temperature or constant in an n-layer system
ref	Reference state

Abbreviations:

CIP	Conventional interfacial polymerization
IMIP	Interlayer-modulated interfacial polymerization
IP	Interfacial polymerization
SFIP	Support-free interfacial polymerization

References

(1) M. Elimelech and W. A. Phillip, "The future of seawater desalination: Energy, technology, and the environment", *Science*, 2011, **333**, 712–717.

(2) J. E. Cadotte, R. J. Petersen, R. E. Larson and E. E. Erickson, "A new thin-film composite seawater reverse osmosis membrane", *Desalination*, 1980, **32**, 25–31.

(3) J. E. Cadotte, R. S. King, R. J. Majerle and R. J. Petersen, "Interfacial Synthesis in the Preparation of Reverse Osmosis Membranes", *Journal of Macromolecular Science: Part A - Chemistry*, 1981, **15**, 727–755.

(4) M. Paul and S. D. Jons, "Chemistry and fabrication of polymeric nanofiltration membranes: A review", *Polymer*, 2016, **103**, 417–456.

(5) M. F. Jimenez-Solomon, Q. Song, K. E. Jelfs, M. Munoz-Ibanez and A. G. Livingston, "Polymer nanofilms with enhanced microporosity by interfacial polymerization", *Nature Materials*, 2016, **15**, 760–767.

(6) R. M. DuChanois, M. Heiranian, J. Yang, C. J. Porter, Q. Li, X. Zhang, R. Verduzco and M. Elimelech, "Designing polymeric membranes with coordination chemistry for high-precision ion separations", *Science Advances*, 2022, **8**, eabm9436.

(7) O. Labban, C. Liu, T. H. Chong and J. H. Lienhard, "Relating transport modeling to nanofiltration membrane fabrication: Navigating the permeability-selectivity trade-off in desalination pretreatment", *Journal of Membrane Science*, 2018, **554**, 26–38.

(8) Z. Ali, B. S. Ghanem, Y. Wang, F. Pacheco, W. Ogieglo, H. Vovusha, G. Genduso, U. Schwingenschlögl, Y. Han and I. Pinnau, "Finely Tuned Submicroporous Thin-Film Molecular Sieve Membranes for Highly Efficient Fluid Separations", *Advanced Materials*, 2020, **32**, 2001132.

(9) J. Liu, G. Han, D. Zhao, K. Lu, J. Gao and T.-S. Chung, "Self-standing and flexible covalent organic framework (COF) membranes for molecular separation", *Science Advances*, 2020, **6**, eabb1110.

(10) L. Wang et al., "Novel Positively Charged Metal-Coordinated Nanofiltration Membrane for Lithium Recovery", *ACS Applied Materials and Interfaces*, 2021, **13**, 16906–16915.

(11) P. R. Buch, D. Jagan Mohan and A. V. R. Reddy, "Preparation, characterization and chlorine stability of aromatic–cycloaliphatic polyamide thin film composite membranes", *Journal of Membrane Science*, 2008, **309**, 36–44.

(12) R. Han, "Formation and characterization of (melamine–TMC) based thin film composite NF membranes for improved thermal and chlorine resistances", *Journal of Membrane Science*, 2013, **425–426**, 176–181.

(13) Y. He, Y. Zhang, F. Liang, Y. Zhu and J. Jin, "Chlorine resistant polyamide desalination membrane prepared via organic-organic interfacial polymerization", *Journal of Membrane Science*, 2023, 121444.

(14) R. Verbeke, V. Gómez and I. F. Vankelecom, "Chlorine-resistance of reverse osmosis (RO) polyamide membranes", *Progress in Polymer Science*, 2017, **72**, 1–15.

(15) Y. Yao, P. Zhang, C. Jiang, R. M. DuChanois, X. Zhang and M. Elimelech, "High performance polyester reverse osmosis desalination membrane with chlorine resistance", *Nature Sustainability*, 2020, 1–9.

(16) R. Verbeke et al., "Chlorine-resistant epoxide-based membranes for sustainable water desalination", *Environmental Science & Technology*, 2021, **8**, 818–824.

(17) D. Davenport, A. Deshmukh, J. Werber and M. Elimelech, "High Pressure Reverse Osmosis for Energy-Efficient Hypersaline Brine Desalination: Current Status, Design Considerations, and Research Needs", *Environmental Science and Technology Letters*, 2018, **5**, 467–475.

(18) W. Yan, M. Shi, Z. Wang, S. Zhao and J. Wang, "Confined growth of skin layer for high performance reverse osmosis membrane", *Journal of Membrane Science*, 2019, **585**, 208–217.

(19) M. Liu, M. D. Nothling, P. A. Webley, Q. Fu and G. G. Qiao, "Postcombustion Carbon Capture Using Thin-Film Composite Membranes", *Accounts of Chemical Research*, 2019, **52**, 1905–1914.

(20) K. Xie, Q. Fu, G. G. Qiao and P. A. Webley, "Recent progress on fabrication methods of polymeric thin film gas separation membranes for CO2 capture", *Journal of Membrane Science*, 2019, **572**, 38–60.

(21) C. Ge, M. Sheng, Y. Yuan, F. Shi, Y. Yang, S. Zhao, J. Wang and Z. Wang, "Recent advances of the interfacial polymerization process in gas separation membranes fabrication", *Journal of Membrane Science*, 2023, **683**, 121854.

(22) M. F. Jimenez Solomon, Y. Bhole and A. G. Livingston, "High flux membranes for organic solvent nanofiltration (OSN)—Interfacial polymerization with solvent activation", *Journal of Membrane Science*, 2012, **423–424**, 371–382.

(23) M. F. Jimenez Solomon, Y. Bhole and A. G. Livingston, "High flux hydrophobic membranes for organic solvent nanofiltration (OSN)-Interfacial polymerization, surface modification and solvent activation", *Journal of Membrane Science*, 2013, **434**, 193–203.

(24) P. Marchetti, M. F. Jimenez Solomon, G. Szekely and A. G. Livingston, "Molecular separation with organic solvent nanofiltration: A critical review", *Chemical Reviews*, 2014, **114**, 10735–10806.

(25) S. Hermans, E. Dom, H. Mariën, G. Koeckelberghs and I. F. J. Vankelecom, "Efficient synthesis of interfacially polymerized membranes for solvent resistant nanofiltration", *Journal of Membrane Science*, 2015, **476**, 356–363.

(26) K. Guan et al., "Thin film composite membrane with improved permeance for reverse osmosis and organic solvent reverse osmosis", *Journal of Membrane Science*, 2023, 122104.

(27) M. J. Raaijmakers and N. E. Benes, "Current trends in interfacial polymerization chemistry", *Progress in Polymer Science*, 2016, **63**, 86–142.

(28) F. Zhang, J. bing Fan and S. Wang, "Interfacial Polymerization: From Chemistry to Functional Materials", *Angewandte Chemie - International Edition*, 2020, **59**, 21840–21856.

(29) S.-J. Park, W. Choi, S.-E. Nam, S. Hong, J. S. Suk and J.-H. Lee, "Fabrication of polyamide thin film composite reverse osmosis membranes via support-free interfacial polymerization", *Journal of Membrane Science*, 2017, **526**, 52–59.

(30) S.-J. Park, W.-G. Ahn, W. Choi, S.-H. Park, J. S. Lee, H. W. Jung and J.-H. Lee, "A facile and scalable fabrication method for thin film composite reverse osmosis membranes: dual-layer slot coating", *Journal of Materials Chemistry A*, 2017, **5**, 6648–6655.

(31) B. Ukrainsky and G. Z. Ramon, "Temperature measurement of the reaction zone during polyamide film formation by interfacial polymerization", *Journal of Membrane Science*, 2018, **566**, 329–335.

(32) V. Freger and G. Z. Ramon, "Polyamide Desalination Membranes: Formation, Structure, and Properties", *Progress in Polymer Science*, 2021, **122**, 101451.

(33) I. Nulens, A. Ben Zvi, I. F. Vankelecom and G. Ramon, "Re-Thinking Polyamide Thin Film Formation: How Does Interfacial Destabilization Dictate Film Morphology?", *Journal of Membrane Science*, 2022, **656**, 120593.

(34) I. Nulens, R. Peters, R. Verbeke, D. M. Davenport, C. Van Goethem, B. De Ketelaere, P. Goos, K. V. Agrawal and I. F. Vankelecom, "MPD and TMC supply as parameters to describe synthesis-morphology-performance relationships of polyamide thin film composite membranes", *Journal of Membrane Science*, 2023, **667**, 121155.

(35) S.-J. Park, M.-S. Lee, M. E. Kilic, J. Ryu, H. Park, Y. I. Park, H. Kim, K.-R. Lee and J.-H. Lee, "Autonomous Interfacial Assembly of Polymer Nanofilms via Surfactant-Regulated Marangoni Instability", *Nano Letters*, 2023, **23**, 4822–4829.

(36) X. H. Ma, Z. K. Yao, Z. Yang, H. Guo, Z. L. Xu, C. Y. Tang and M. Elimelech, "Nanofoaming of Polyamide Desalination Membranes to Tune Permeability and Selectivity", *Environmental Science and Technology Letters*, 2018, **5**, 123–130.

(37) X. Song, B. Gan, Z. Yang, C. Y. Tang and C. Gao, "Confined nanobubbles shape the surface roughness structures of thin film composite polyamide desalination membranes", *Journal of Membrane Science*, 2019, **582**, 342–349.

(38) L. E. Peng, Z. Yao, Z. Yang, H. Guo and C. Y. Tang, "Dissecting the Role of Substrate on the Morphology and Separation Properties of Thin Film Composite Polyamide Membranes: Seeing Is Believing", *Environmental Science and Technology*, 2020, **54**, 6978–6986.

(39) L. E. Peng, Y. Jiang, L. Wen, H. Guo, Z. Yang and C. Y. Tang, "Does interfacial vaporization of organic solvent affect the structure and separation properties of polyamide RO membranes ?", *Journal of Membrane Science*, 2021, **625**, 119173.

(40) L. E. Peng, Z. Yang, L. Long, S. Zhou, H. Guo and C. Y. Tang, "A critical review on porous substrates of TFC polyamide membranes: Mechanisms, membrane performances, and future perspectives", *Journal of Membrane Science*, 2021, **641**, 119871.

(41) S. Karan, Q. Wang, S. Samitsu, Y. Fujii and I. Ichinose, "Ultrathin free-standing membranes from metal hydroxide nanostrands", *Journal of Membrane Science*, 2013, **448**, 270–291.

(42) S. Karan, Z. Jiang and A. G. Livingston, "Sub-10 nm polyamide nanofilms with ultrafast solvent transport for molecular separation", *Science*, 2015, **348**, 1347–1351.

(43) Z. Yang, P. F. Sun, X. Li, B. Gan, L. Wang, X. Song, H. D. Park and C. Y. Tang, "A Critical Review on Thin-Film Nanocomposite Membranes with Interlayered Structure: Mechanisms, Recent Developments, and Environmental Applications", *Environmental Science and Technology*, 2020, **54**, 15563–15583.

(44) C. Yang, S. Li, X. Lv, H. Li, L. Han and B. Su, "Effectively regulating interfacial polymerization process via in-situ constructed 2D COFs interlayer for fabricating organic solvent nanofiltration membranes", *Journal of Membrane Science*, 2021, **637**, 104743.

(45) S. Cao, A. Deshmukh, L. Wang, Q. Han, Y. Shu, H. Y. Ng, Z. Wang and J. H. Lienhard, "Enhancing the Permselectivity of Thin-Film Composite Membranes Interlayered with MoS_2 Nanosheets via Precise Thickness Control", *Environmental Science & Technology*, 2022, **56**, 8807–8818.

(46) T. D. Matthews, H. Yan, D. G. Cahill, O. Coronell and B. J. Marinas, "Growth dynamics of interfacially polymerized polyamide layers by diffuse reflectance spectroscopy and Rutherford backscattering spectrometry", *Journal of Membrane Science*, 2013, **429**, 71–80.

(47) A. Nowbahar, V. Mansard, J. M. Mecca, M. Paul, T. Arrowood and T. M. Squires, "Measuring Interfacial Polymerization Kinetics Using Microfluidic Interferometry", *Journal of the American Chemical Society*, 2018, **140**, 3173–3176.

(48) J. Mansouri, S. Huang, A. Agostino, R. P. Kuchel, G. Leslie, C. Y. Tang and A. G. Fane, "Kinetics of support-free interfacial polymerization polyamide films by in-situ absorbance spectroscopy", *Desalination*, 2023, **549**, 116349.

(49) I. Nulens, R. Verbeke, T. Opsomer, J. Huang, Y. Wang, S. Caspers, A. Kubarev, A. H. McMillan, W. Dehaen and I. F. J. Vankelecom, "Real-time monitoring of interfacial polymerization using fluorescent dyes", *Journal of Membrane Science*, 2023, **686**, 121998.

(50) X. Lu and M. Elimelech, "Fabrication of desalination membranes by interfacial polymerization: history, current efforts, and future directions", *Chemical Society Reviews*, 2021, **50**, 6290–6307.

(51) X. Li, Z. Wang, X. Han, Y. Liu, C. Wang, F. Yan and J. Wang, "Regulating the interfacial polymerization process toward high-performance polyamide thin-film composite reverse osmosis and nanofiltration membranes: A review", *Journal of Membrane Science*, 2021, **640**, 119765.

(52) J. H. Lienhard, IV and J. H. Lienhard, *A Heat Transfer Textbook*, Dover Publications, Mineola, NY, 5th ed, 2019.

(53) P. W. Morgan and S. L. Kwolek, "Interfacial polycondensation. II. Fundamentals of polymer formation at liquid interfaces", *Journal of Polymer Science*, 1959, **40**, 299–327.

(54) S. K. Karode, S. S. Kulkarni, A. K. Suresh and R. A. Mashelkar, "New insights into kinetics and thermodynamics of interfacial polymerization", *Chemical Engineering Science*, 1998, **53**, 2649–2663.

(55) V. Freger, "Kinetics of film formation by interfacial polycondensation", *Langmuir*, 2005, **21**, 1884–1894.

(56) A. V. Berezkin and A. R. Khokhlov, "Mathematical modeling of interfacial polycondensation", *Journal of Polymer Science, Part B: Polymer Physics*, 2006, **44**, 2698–2724.

(57) R. Nadler and S. Srebnik, "Molecular simulation of polyamide synthesis by interfacial polymerization", *Journal of Membrane Science*, 2008, **315**, 100–105.

(58) P. Jha and A. K. Suresh, "A modelling study of interfacial polyamidation", *Applied Surface Science*, 2023, **613**, 155889.

(59) Y. Zhang, P. Xu, X. Chen, M. Qiu and Y. Fan, "Preparation of high permeance thin-film composite nanofiltration membrane on macroporous ceramic support", *Journal of Membrane Science*, 2022, **663**, 121076.

(60) E. Maaskant, P. de Wit and N. E. Benes, "Direct interfacial polymerization onto thin ceramic hollow fibers", *Journal of Membrane Science*, 2018, **550**, 296–301.

(61) R. Dai, J. Li and Z. Wang, "Constructing interlayer to tailor structure and performance of thin-film composite polyamide membranes: A review", *Advances in Colloid and Interface Science*, 2020, **282**, 102204.

(62) N. V. Suryanarayana, *Engineering Heat Transfer*, West Publishing Company, New York, 1995.

(63) R. C. Steere, "Thermal Properties of Thin-Film Polymers by Transient Heating", *Journal of Applied Physics*, 1966, **37**, 3338–3344.

(64) C. W. Smith and M. Dole, "Specific heat of synthetic high polymers. VII. Polyethylene terephthalate", *Journal of Polymer Science*, 1956, **20**, 37–56.

(65) Y. Wu, K. Ye, Z. Liu, M. Wang, K. W. A. Chee, C.-T. Lin, N. Jiang and J. Yu, "Effective thermal transport highway construction within dielectric polymer composites via a vacuum-assisted infiltration method", *Journal of Materials Chemistry C*, 2018, **6**, 6494–6501.

(66) Thermtest, *Materials Database - Thermal Properties - Thermtest Inc.* https://thermtest.com/thermal-resources/materials-database.

(67) C. Bell, Y. R. Cortes-Pena and Contributors, *Chemicals: Chemical Properties Component of Chemical Engineering Design Library (ChEDL)*, https://github.com/CalebBell/chemicals.

(68) I. H. Bell, J. Wronski, S. Quoilin and V. Lemort, "Pure and Pseudo-pure Fluid Thermophysical Property Evaluation and the Open-Source Thermophysical Property Library CoolProp", *Industrial and Engineering Chemistry Research*, 2014, **53**, 2498–2508.

(69) L. R. Glicksman and J. H. Lienhard, *Modeling and Approximation in Heat Transfer*, Cambridge University Press, 1st edn., 2016.

(70) J. K. Carson, S. J. Lovatt, D. J. Tanner and A. C. Cleland, "Thermal conductivity bounds for isotropic, porous materials", *International Journal of Heat and Mass Transfer*, 2005, **48**, 2150–2158.

(71) R. C. Progelhof, J. L. Throne and R. R. Ruetsch, "Methods for predicting the thermal conductivity of composite systems: A review", *Polymer Engineering & Science*, 1976, **16**, 615–625.

(72) C. E. Goodyer and A. L. Bunge, "Mass transfer through membranes with surface roughness", *Journal of Membrane Science*, 2012, **409–410**, 127–136.

(73) J. Rolf, T. Cao, X. Huang, C. Boo, Q. Li and M. Elimelech, "Inorganic Scaling in Membrane Desalination: Models, Mechanisms, and Characterization Methods", *Environmental Science & Technology*, 2022, **56**, 7484–7511.

(74) L. Wang, J. He, M. Heiranian, H. Fan, L. Song, Y. Li and M. Elimelech, "Water transport in reverse osmosis membranes is governed by pore flow, not a solution-diffusion mechanism", *Science Advances*, 2023, **9**, eadf8488.

(75) R. Z. Waldman, F. Gao, W. A. Phillip and S. B. Darling, "Maximizing selectivity : An analysis of isoporous membranes", *Journal of Membrane Science*, 2021, **633**, 119389.

(76) J. D. Hunter, "Matplotlib: A 2D Graphics Environment", *Computing in Science & Engineering*, 2007, **9**, 90–95.

(77) M. L. Waskom, "seaborn: statistical data visualization", *Journal of Open Source Software*, 2021, **6**, 3021.

(78) A. Meurer et al., "SymPy: symbolic computing in Python", *PeerJ Computer Science*, 2017, **3**, e103.

(79) H. S. Carslaw and J. C. Jaeger, *Conduction of Heat in Solids*, Oxford University Press, 1959.

(80) H. Bateman, *Tables of Integral Transforms*, ed. A. Erdélyi, McGraw-Hill Book Company, New York, 1954, vol. 1–2.

(81) F. Johansson and Contributors, *mpmath: a Python library for arbitrary-precision floating-point arithmetic (version 1.3.0)*, http://mpmath.org/, 2023.

(82) L. F. Richardson and R. T. Glazebrook, "IX. The approximate arithmetical solution by finite differences of physical problems involving differential equations, with an application to the stresses in a masonry dam", *Philosophical Transactions of the Royal Society of London A*, 1910, **210**, 307–357.

(83) L. F. Richardson and J. A. Gaunt, "VIII. The deferred approach to the limit", *Philosophical Transactions of the Royal Society of London A*, 1927, **226**, 299–361.

(84) A. Talbot, "The Accurate Numerical Inversion of Laplace Transforms", *IMA Journal of Applied Mathematics*, 1979, **23**, 97–120.